ANL-ART-290
ANL-METL-53

Report on Initial Sodium Testing on the Thermal Hydraulic Experimental Test Article (THETA)–Fiscal Year 2024 Final Report

---

Nuclear Science & Engineering

About Argonne National Laboratory
Argonne is a U.S. Department of Energy laboratory managed by UChicago Argonne, LLC under contract DE-AC02-06CH11357. The Laboratory's main facility is outside Chicago, at 9700 South Cass Avenue, Argonne, Illinois 60439. For information about Argonne and its pioneering science and technology programs, see www.anl.gov.

DOCUMENT AVAILABILITY

Online Access: U.S. Department of Energy (DOE) reports produced after 1991 and a growing number of pre-1991 documents are available free at OSTI.GOV (http://www.osti.gov/), a service of the US Dept. of Energy's Office of Scientific and Technical Information.

Reports not in digital format may be purchased by the public from the National Technical Information Service (NTIS):

U.S. Department of Commerce National
Technical Information Service 5301
Shawnee Rd
Alexandria, VA 22312
www.ntis.gov
Phone: (800) 553-NTIS (6847) or (703) 605-6000
Fax: (703) 605-6900
Email: **orders@ntis.gov**

Reports not in digital format are available to DOE and DOE contractors from the Office of Scientific and Technical Information (OSTI):

U.S. Department of Energy
Office of Scientific and Technical Information
P.O. Box 62
Oak Ridge, TN 37831-0062
www.osti.gov
Phone: (865) 576-8401
Fax: (865) 576-5728
Email: **reports@osti.gov**

Disclaimer
This report was prepared as an account of work sponsored by an agency of the United States Government. Neither the United States Government nor any agency thereof, nor UChicago Argonne, LLC, nor any of their employees or officers, makes any warranty, express or implied, or assumes any legal liability or responsibility for the accuracy, completeness, or usefulness of any information, apparatus, product, or process disclosed, or represents that its use would not infringe privately owned rights. Reference herein to any specific commercial product, process, or service by trade name, trademark, manufacturer, or otherwise, does not necessarily constitute or imply its endorsement, recommendation, or favoring by the United States Government or any agency thereof. The views and opinions of document authors expressed herein do not necessarily state or reflect those of the United States Government or any agency thereof, Argonne National Laboratory, or UChicago Argonne, LLC.

ANL-ART-290
ANL-METL-53

Report on Initial Sodium Testing on the Thermal Hydraulic Experimental Test Article (THETA)– Fiscal Year 2024 Final Report

---

prepared by:
Matthew Weathered, Christopher Grandy, Derek Kultgen, Edward Kent, Jordan Rein, Alex Grannan, Evan Ogren, Yeongshin Jeong, Lander Ibarra

Nuclear Science & Engineering, Argonne National Laboratory

August 2024

Executive Summary

The Thermal Hydraulic Experimental Test Article (THETA) is a facility that is used to develop sodium components and instrumentation as well as to acquire experimental data for validation of reactor thermal hydraulic and safety analysis codes. The facility simulates nominal thermal hydraulic conditions as well as protected/unprotected loss of flow accidents in a sodium-cooled fast reactor (SFR). High fidelity distributed temperature profiles of the developed flow field may be acquired with Rayleigh backscatter based optical fiber temperature sensors. The facility was designed in partnership with systems code experts to tailor the experiment to ensure the most relevant and highest quality data for code validation.

THETA is comprised of a traditional primary coolant and secondary coolant system. The primary system is submerged in the pool of sodium and consists of a pump, electrically heated core, intermediate heat exchanger, and connected piping and thermal barriers (redan). The secondary system, located outside of the sodium pool, consists of a pump, sodium to air heat exchanger, and connected piping and valves.

In fiscal year 2023, thermal stratification tests were completed with the primary system online, while the secondary system was being constructed [1]. These tests had shown that the core barrel and intermediate heat exchanger (IHX) outlet required increased thermal insulation. The THETA primary system was removed from METL, cleaned, thermal insulators installed, and then inserted into METL Test Vessel 4.

At the time of this writing the THETA primary and secondary system are operational. During this fiscal year 100+ hours of testing was completed to characterize thermal hydraulic phenomena associated with steady state and transient conditions in a pool type liquid metal cooled reactor. A majority of the testing campaign was completed to satisfy the experimental data acquisition requirements for the GAIN Voucher with Oklo, CRADA 2021-21121.

THETA is still operational at the time of this publication and future testing is planned for fiscal year 2025. Work is underway to publish existing and future data to an online database to facilitate collaboration with SFR engineers looking to validate their systems code or computational fluid dynamics models.

This page was intentionally left blank.

Table of Contents

List of Figures

List of Tables

1. Introduction

The Thermal Hydraulic Experimental Test Article (THETA) is a Mechanisms Engineering Test Loop (METL) vessel experiment designed for testing and validating sodium fast reactor components and phenomena. Figure 1 to Figure 5 provide drawings and photographs of the THETA primary and secondary system. THETA possesses all the major thermal hydraulic components of a pool type sodium cooled reactor. Figure 6 provides a P&ID of the THETA primary and secondary system. THETA has been scaled using a non-dimensional Richardson number approach to represent temperature distributions during nominal and loss of flow conditions in a sodium fast reactor (SFR) [2]. THETA was designed in collaboration with systems code experts to inform the geometry and sensor placement to acquire the highest value code validation data.

This report will begin by providing an overview of component analyses/updates that were performed during fiscal year 2024. This includes a modeling effort to characterize secondary flowmeter generated voltage as a function of sodium flow.

A select test will then be analyzed to demonstrate the capabilities and performance of the THETA primary and secondary system components and sensors. This test, ID # 2024-05-23-01, was 150 minutes long and brought the primary and secondary system to steady state at a low, medium and high core power level. A method of in-situ calibration of the optical fibers with co-located thermocouples will be provided. The fibers will then be used to characterize thermal hydraulic phenomena such as stratification and striping both spatially and temporally.

Finally, the ~100 hours of THETA testing that was completed to satisfy a GAIN Voucher with Oklo, CRADA 2021-21121 will be discussed and select data will be presented to give a broad overview of the work. This testing in partnership with Oklo is also discussed in [3]. The data from this testing will be available at a future date to be downloaded in an online database.

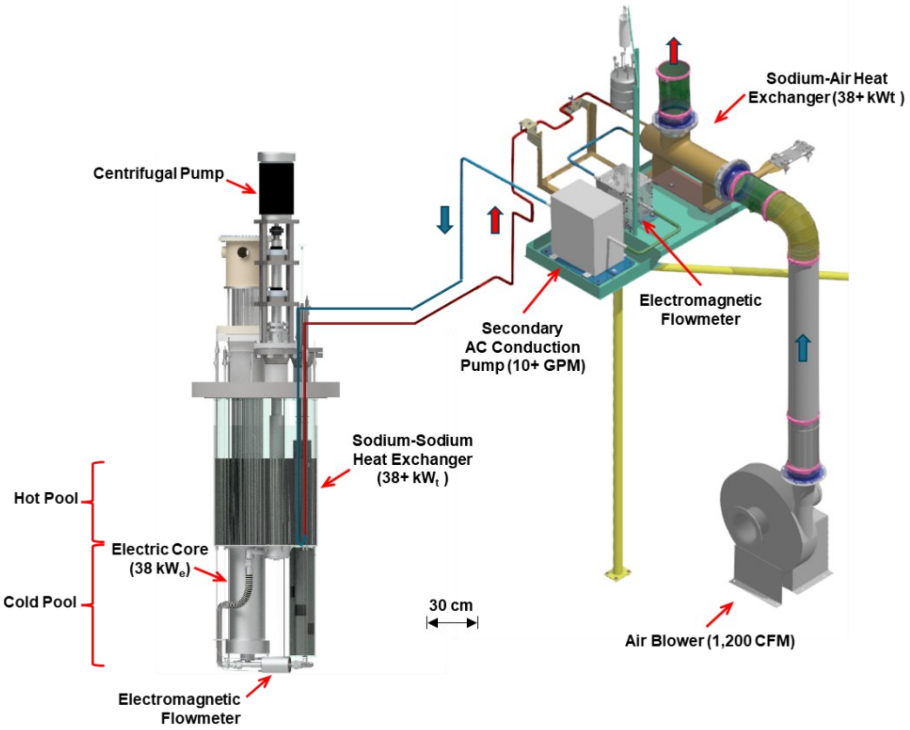

Figure 1: THETA primary and secondary system. Secondary piping and primary system orientation modified for visual clarity and are not to scale.

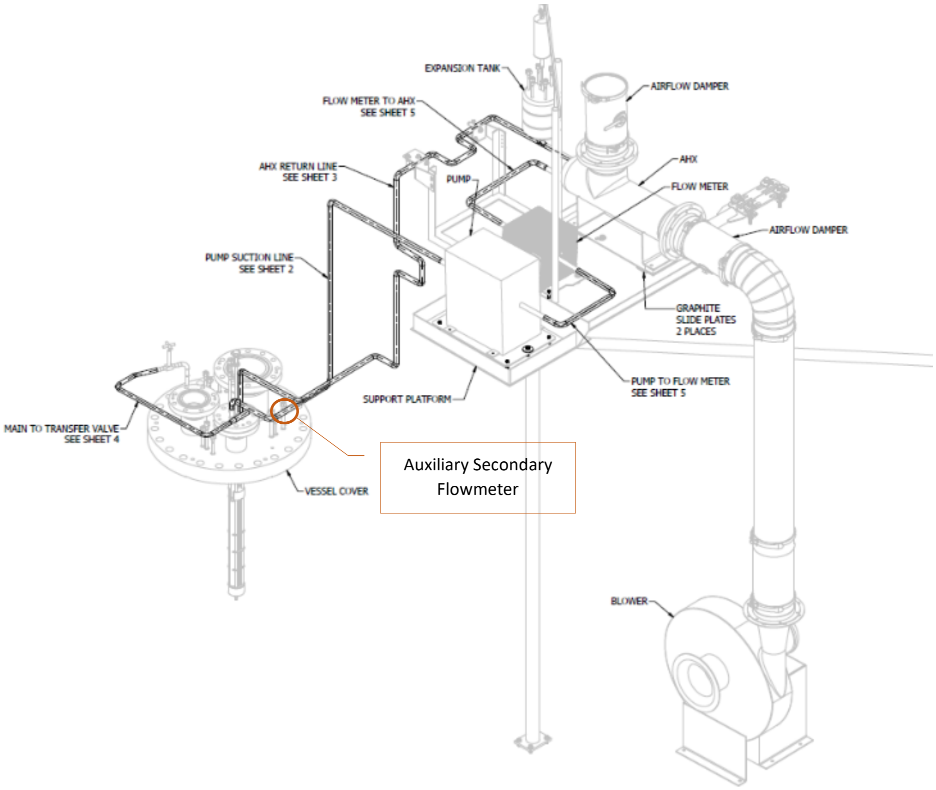

Figure 2: Isometric drawing of THETA secondary system with piping to scale. For reference the primary THETA flange is 36” in diameter

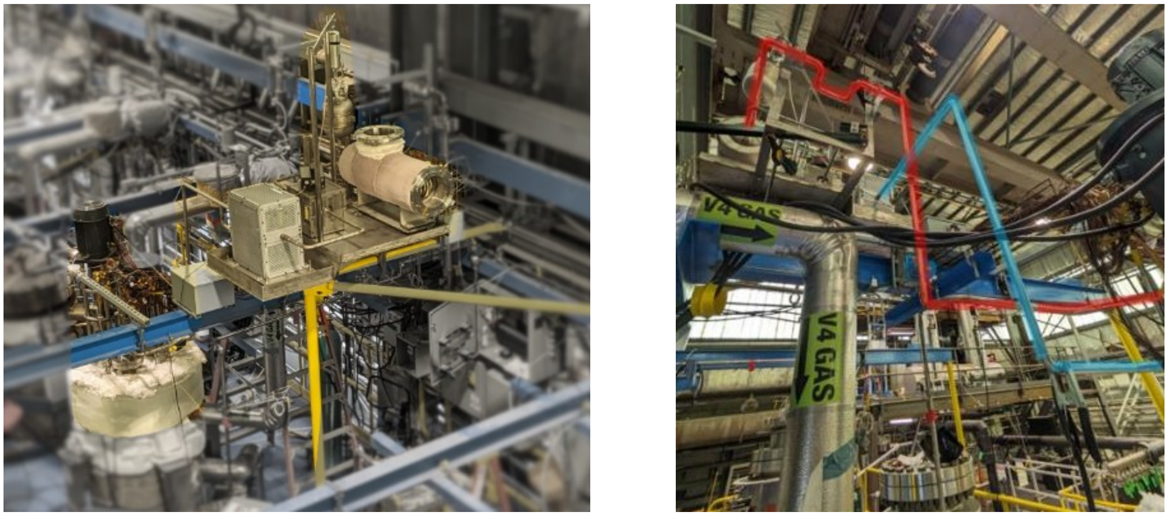

Figure 3: Photographs showing the THETA secondary system components installed on the platform structure (left) and the hot return and cold supply secondary sodium piping (right). Note the hot return and cold supply sodium pipes have been highlighted with red and blue, respectively.

Figure 4: AHX blower installed on mezzanine. 9” stainless steel ducting being installed.

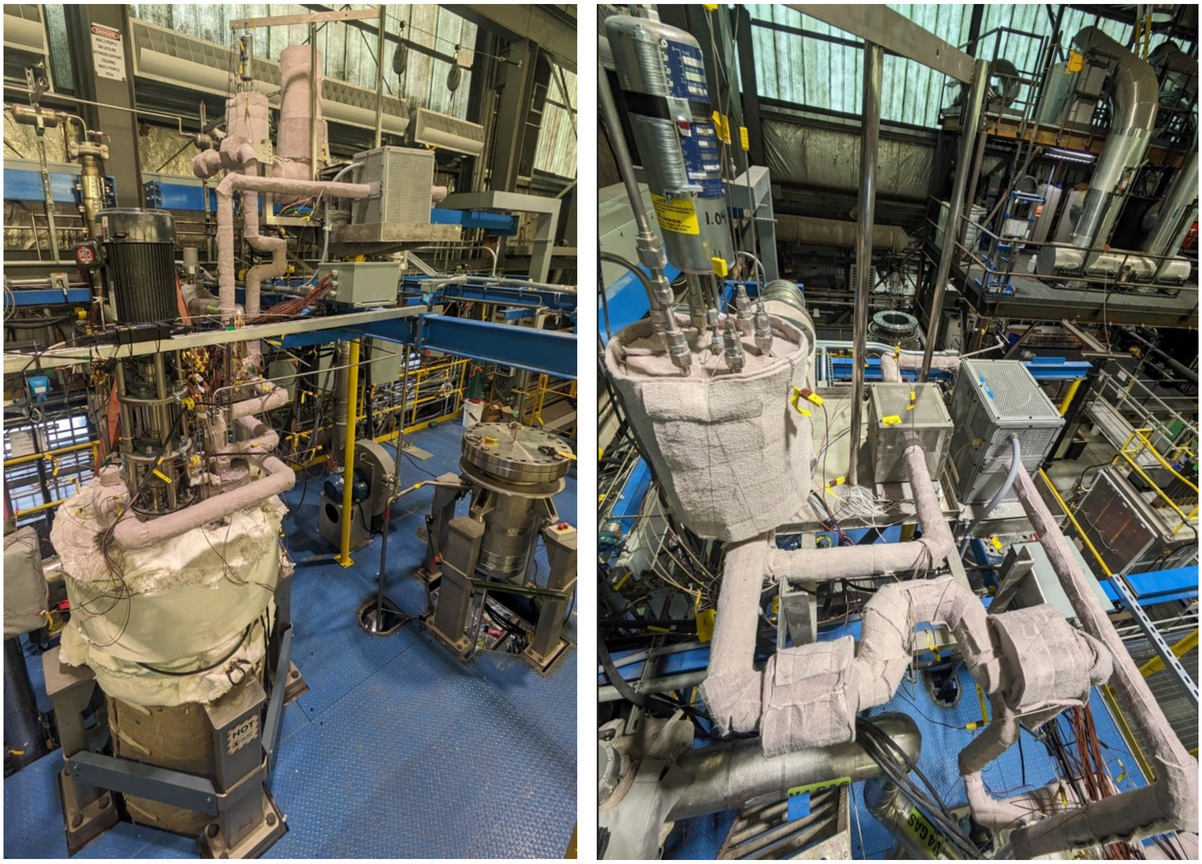

Figure 5: Photos of the THETA primary and secondary system

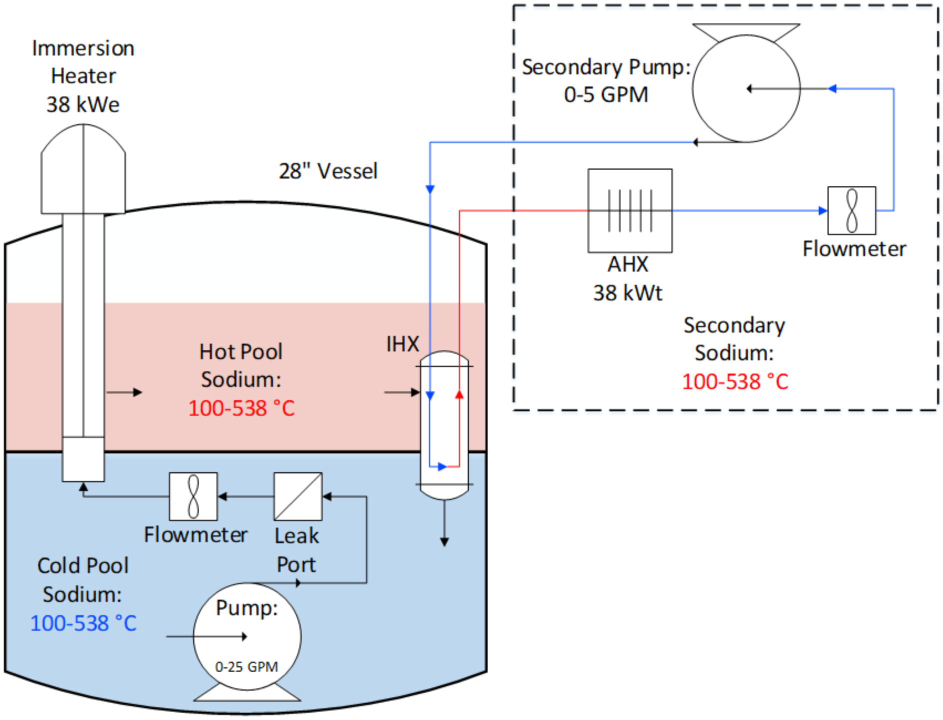

Figure 6: P&ID schematic of THETA primary and secondary system. Secondary system highlighted with dashed box

2. Facility Updates

2.1. Secondary Flowmeter

2.1.1. Noise in Flowmeter Voltage

A considerable amount of noise was observed during testing in the THETA secondary flowmeter. The flowmeter is near the AC conduction pump, Figure 2, which was suspected to be contributing to the noise in the flowmeter data. A sample of secondary flowmeter data can be found in Figure 7 where data from two different tests with the same secondary pump setpoint (55% duty cycle) and similar sodium temperature are compared. As can be seen during the *2023_11_14_02* test (data set 1 in plot) there was a significant amount of noise in the induced flowmeter voltage, fluctuating around 6.2 mV ± 1.1 mV. The flowmeter voltage was being read by a National Instruments 9219 analog voltage input module. The 9219 supports four different timing options that are optimized for various types of applications by using different analog-to-digital conversion methods. During set 1 in Figure 7 the *High Speed* conversion time option (20 ms acquisition time for all channels) was used for data acquisition as a 100 ms acquisition rate was desired. Another of the 4 timing options for the 9219 is *Best 60 Hz Rejection* conversion time method. This noise rejection analog-to-digital conversion method was utilized for data set 2 (test *2024_05_23_01*) in Figure 7 and eliminated the large sinusoidal fluctuation that was apparent in set

1. The acquisition time for the *Best 60 Hz Rejection* conversion method was 120 ms, so if a 100 ms acquisition rate is desired for the overall data acquisition system then every ~5th flowmeter voltage reading will be repeated in the data. Visually, over long time periods of 5+ minutes, data set 1 oscillates about a mean voltage that resembles the set 2 data (that had 60 Hz noise filter)- thus it is possible to smooth the non-noise rejected data with a large 5+ minute window, however small perturbations or quickly changing flowrates will not be apparent. As of test *2024_05_23_01* all flowmeter data is 60 Hz noise rejected, though the primary submerged flowmeter seems to be unaffected by the same 60 Hz noise as the secondary flowmeter. Going forward with experiments it seems the Labview software based 60 Hz noise rejection will be sufficient to yield a satisfactory signal to noise ratio.

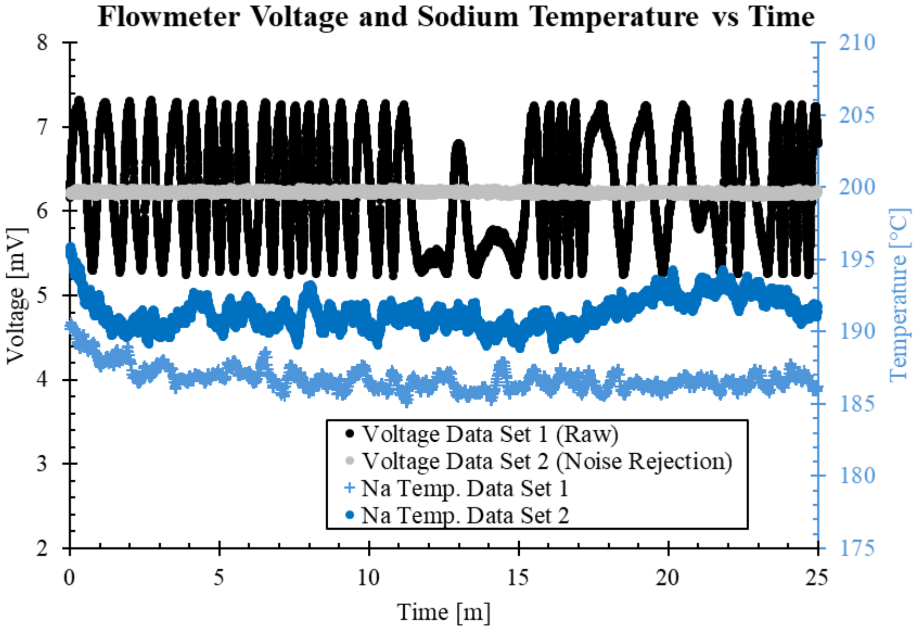

Figure 7: Flowmeter voltage and sodium temperature vs time for two data sets. Both data sets possessed simliar sodium temperature, as shown, and a continuous secondary AC conduction pump duty cycle set point of 55%. Data set 1 before noise rejection from test 2023_11_14_02 and data set 2 after 60 Hz noise rejection implemented from test 2024_05_23_01

2.1.2. Development of Auxiliary Secondary Flowmeter

Prior to determining that the source of the noise in the main secondary flowmeter could be resolved with 60 Hz noise rejection, an auxiliary permanent magnet flowmeter was designed that could be attached to the existing secondary piping to facilitate ease of installation at various locations in the secondary system. This would allow for placement of the flowmeter at a location further away from the AC conduction pump without extensive modification to the existing loop.

Figure 8 provides a photo of the auxiliary secondary flowmeter installed on a temporary piece of pipe where the ¾” SCH 40 316SS pipe, pipe mount, magnet mount and magnets are highlighted. The pipe mount is 316L and was manufactured using metal binder jet 3D printing with a zirconium silicate bead sandblast finish. The 316L was chosen for the pipe mount to match the thermal expansion rate of the existing THETA secondary piping. The magnet mount was made with X1 Metal 316i™, a 316 stainless steel (60%) infiltrated with bronze (40%). This material was chosen to reduce cost in the overall assembly. Ceramic thermal brake washers were employed in the assembly to minimize heat transfer between the pipe and magnet mounts. The magnets used were grade 26 samarium cobalt disk magnets (maximum operating temperature ~350 °C [4]) with a diameter of 2” and a thickness of 0.5”. Note that four magnets were used in the assembly with two magnets stacked on each side of the pipe.

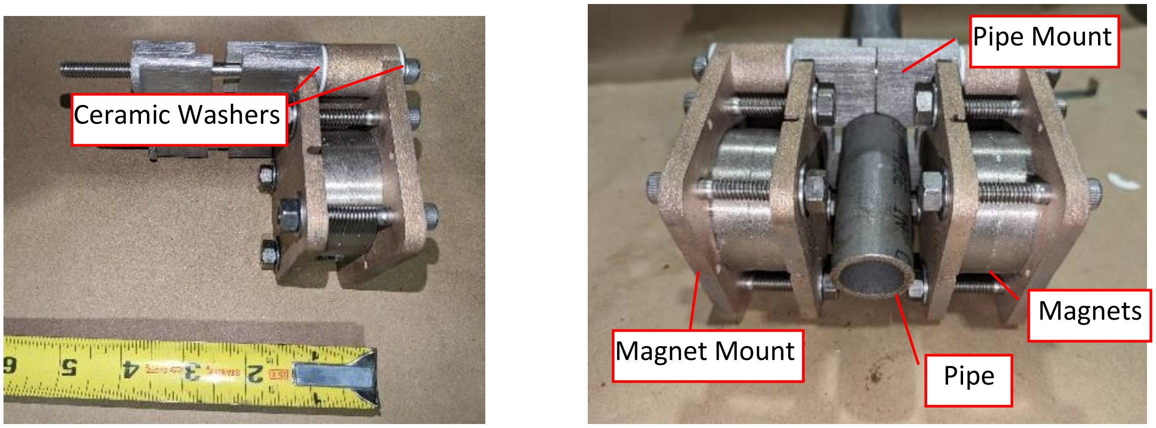

Figure 8: Auxiliary secondary flowmeter. Left photo shows flowmeter partially assembled with ceramic thermal brake washers highlighted for reference. Right photo shows the complete assembly installed on a piece of blank pipe (without any leads welded on).

The magnetic field was measured with an F.W. Bell 5180 gaussmeter (±1% rated accuracy) to be 19.5 mT, Figure 9. A location was selected in the secondary piping on the cold leg far downstream from the AC conduction pump, the location is highlighted in Figure 2. A photo showing the 0.010” thick 316 stainless steel leads that were spot welded onto THETA secondary piping is provided in Figure 10. A photo of the as installed auxiliary secondary flowmeter has been provided in Figure 11.

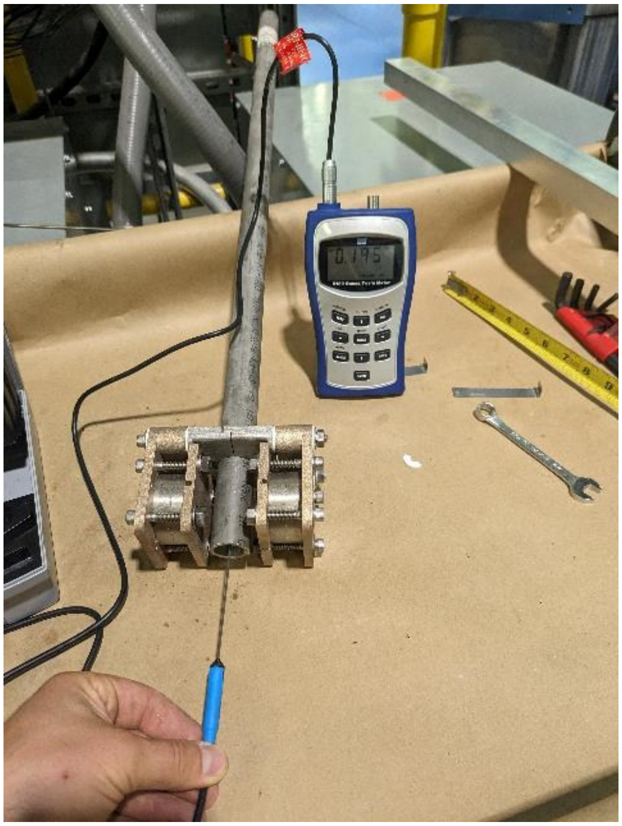

Figure 9: Photo showing the magnetic field measurement at the center of a 316 stainless steel pipe at room temperature

Figure 10: Photo showing voltage measurement leads made with 316ss sheet metal, left. The leads as installed on THETA secondary system are shown in the right photo.

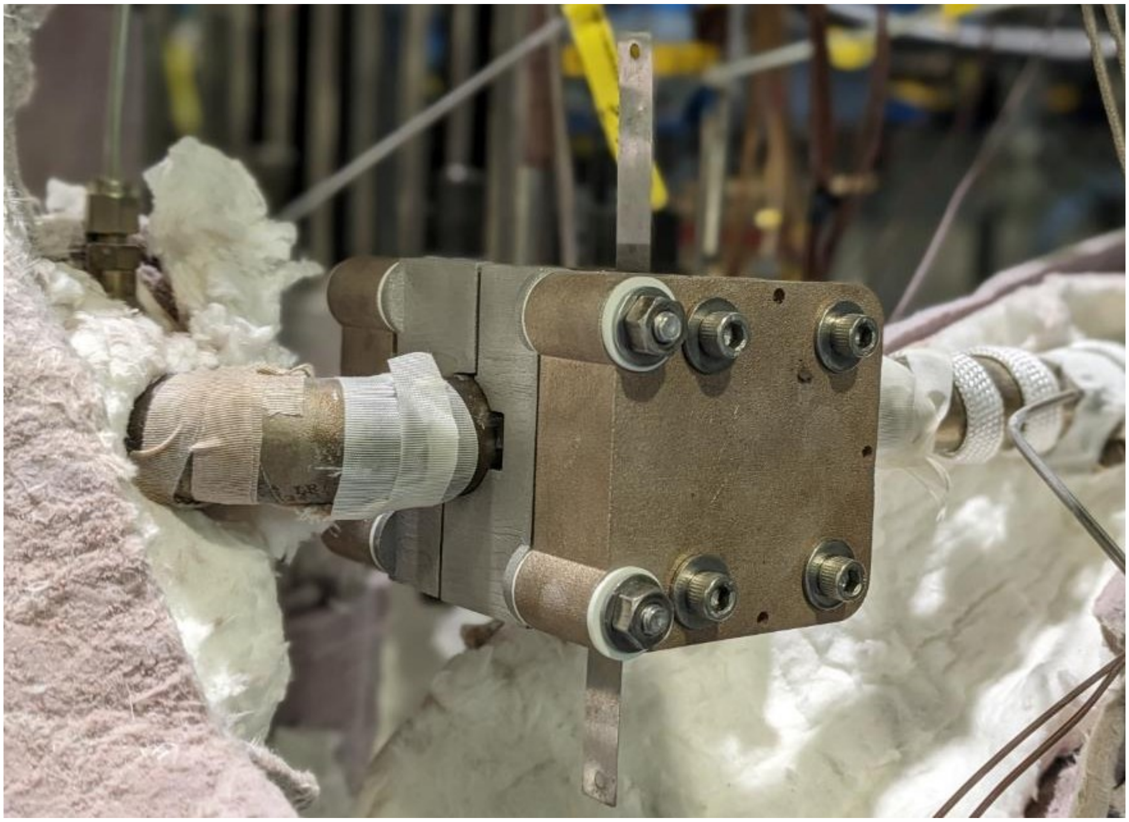

Figure 11: Auxiliary secondary THETA flowmeter as installed before insulating pipe

A finite element analysis (FEA) was performed on the auxiliary secondary flowmeter to determine the generated voltage as a function of system temperature and sodium flow rate. Using the methods described by Weathered in [5], the magnetohydrodynamic (MHD) system was simulated using COMSOL Multiphysics 5.6.

A 15.2 cm (6 in) length of ¾" SCH40 pipe was simulated where the magnetic assembly was positioned at the center of this length and the sodium inlet domain assumed a fully developed flow. Note that the ¾" elbow approximately 4.3 cm downstream of the magnets in the actual flowmeter, Figure 11, was assumed to not have an effect on the measured voltage as a function of flow given the magnetic field has a tendency to reduce/eliminate turbulent effects in the fluid near the field [5]- however this would be a subject for future study to prove this assumption. A 10 cm cube represented the air domain in the simulation, its centroid positioned at the center of the flow pipe.

The sodium flow domain was solved using a k-epsilon turbulence model and was tied to the magnetic and electrical effects using a Lorentz force term. The sodium, stainless steel and SmCo magnet material properties used in the simulation were found in [6], [7], [8]. Figure 12 provides a view of the mesh for the magnet, pipe and sodium domain. The model possesses 202,608 elements with an average element quality (skewness) of 0.672 where 1.0 is the best possible skewness, a histogram showing the mesh element skewness histogram can be found in Figure 12. Note that highlighted in Figure 12 the sodium domain possesses 8 thin boundary layers on the inner wall of the pipe with the first layer having a thickness of 30 μm to satisfy the Hartman layer requirement for accurate MHD analysis [5].

The magnets used in the flowmeter possessed a residual magnetic flux density at room temperature, defined as $B_{r,o}$, of 1.05 T with an average residual magnetic flux density temperature coefficient, defined as α, of -0.03 %/°C [8]. In COMSOL, the sodium domain was replaced with air and the magnetic field was calculated using a residual magnetic flux density of 1.05 T. The distributed magnetic field calculated between the magnets was provided in Figure 13. In order to increase the magnetic field set in COMSOL at the center of the pipe to match the actual measured magnetic field of 19.5 mT, as in Figure 9, a fit factor defined as K_1 was used of 1.075. The equation derived here to calculate the residual magnetic flux density as a function of temperature in COMSOL is provided in Eq. 1.

$$B_{r,T}[T] = K_1 \cdot B_{r,o} \cdot \left(1 - (T[°\mathrm{C}] - 25) \cdot \frac{|\alpha|}{100}\right) \tag{1}$$

The parameters used in the FEA can be found in Table 1. A parametric sweep was performed where every variable combination from Table 1 was used as values for the simulation. The distributed sodium velocity and magnetic field contour lines for the sodium and magnets at 500 and 250 °C, respectively, have been provided in Figure 14 and Figure 15 for a sodium flowrate of 0.5 and 10 GPM, respectively. Note that the sodium velocity profile across the pipe is made constant after traveling across the magnetic field, thus reducing the effects of downstream geometry on the velocity profile in the location of measure. The results for induced voltage as a function of the 16 different cases considered in the parametric sweep can be found in Figure 16 and Figure 17.

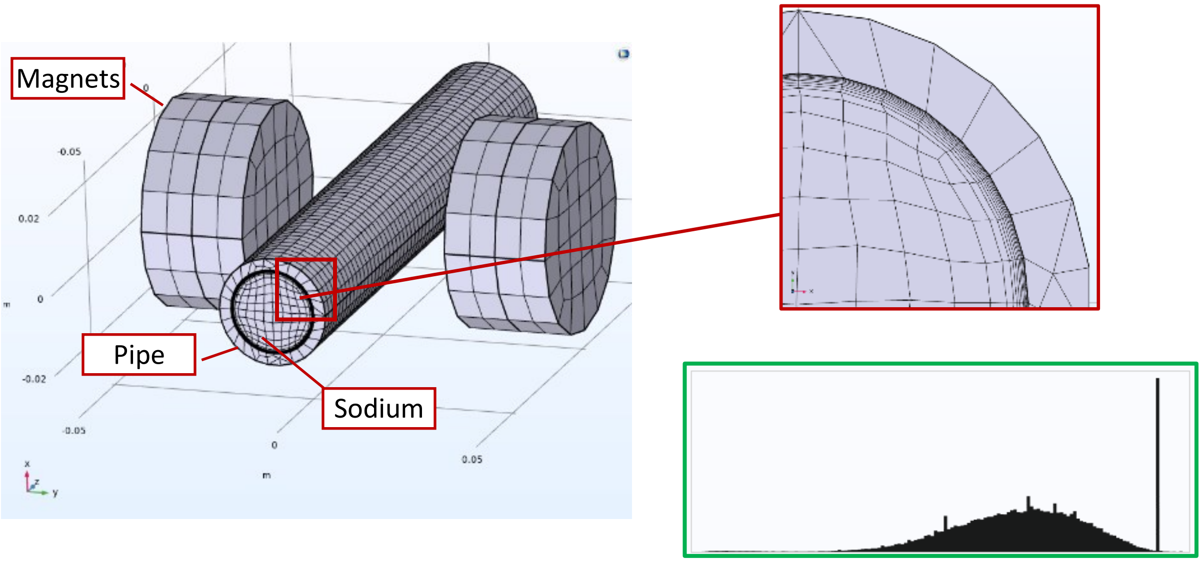

Figure 12: Mesh for magnets, pipe and sodium domain shown on left. Highlighted in top right are the mesh expansion layers in the sodium domain. A histogram in the bottom right shows quality of mesh elements (skewness) rated from 0 (worst) to 1 (best).

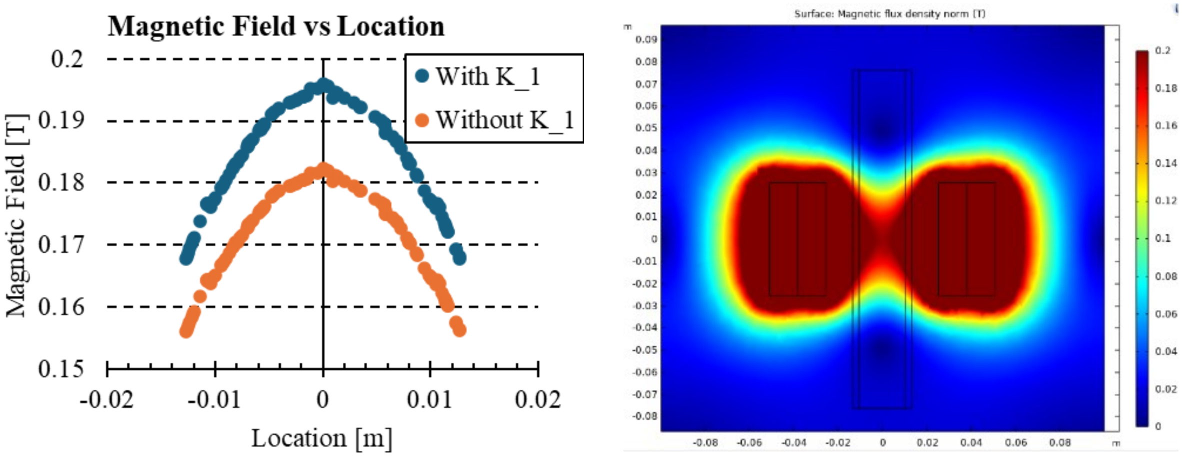

Figure 13: Left: magnetic field vs location in stainless steel pipe filled with air without and with a fit factor K_1 of 1.075. Right: distributed magnetic field with fit factor in air at 25 °C

Table 1: Parameters used in flowmeter FEA

Parameter	Parameter Value List	Parameter Unit
Magnet Temperature	100, 250	°C
Sodium Temperature	100, 500	°C
Sodium Flowrate	0.5, 2, 5, 10	GPM

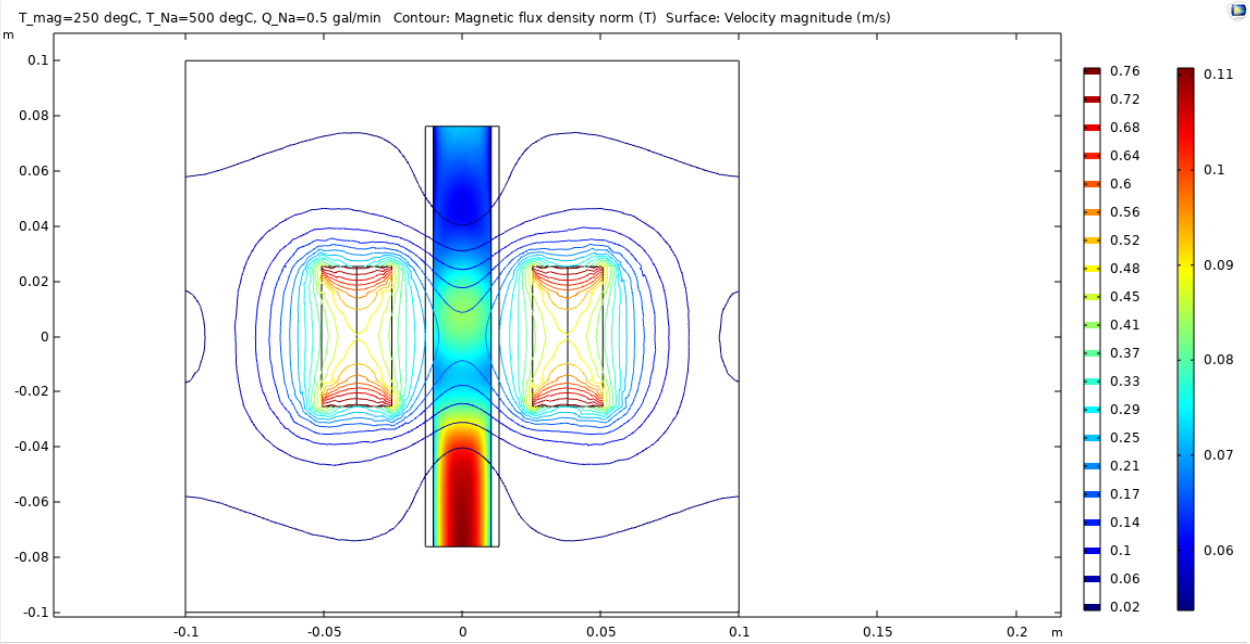

Figure 14: Distributed velocity magnitude shown in surface plot and magnetic flux density shown with contour lines looking top down on the flowmeter with sodium entering the bottom of the pipe. Temperature of magnet 250 °C, temperature of sodium 500 °C, flowrate of sodium 0.5 GPM

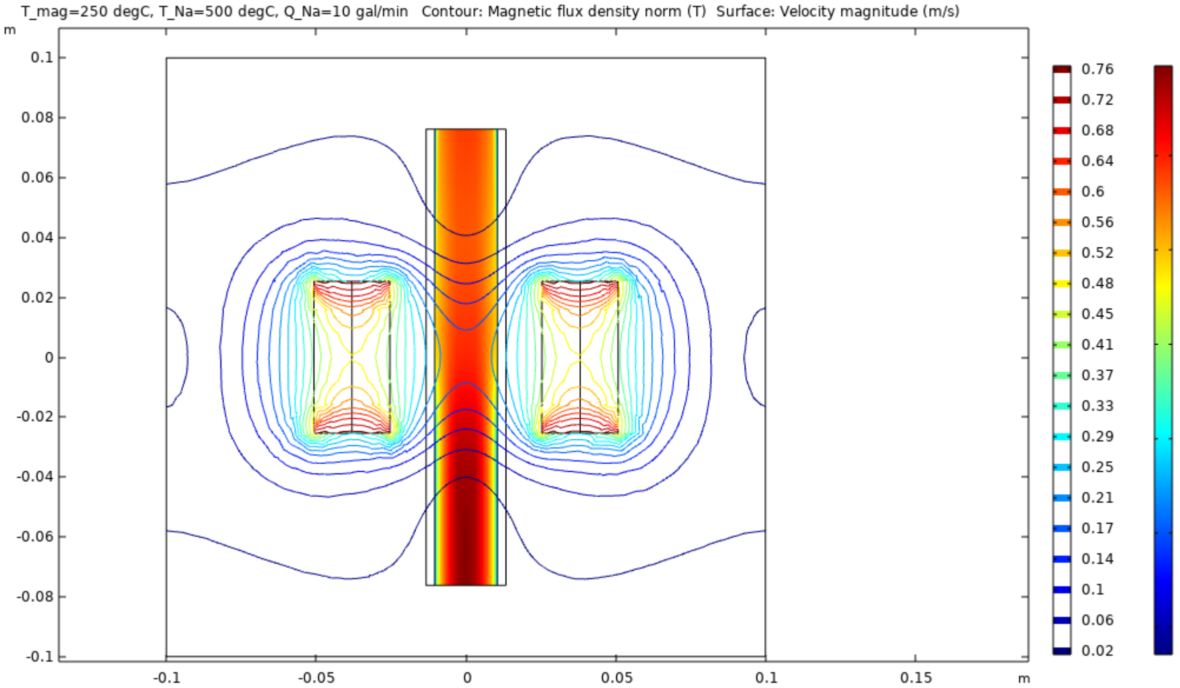

Figure 15: Distributed velocity magnitude shown in surface plot and magnetic flux density shown with contour lines looking top down on the flowmeter with sodium entering the bottom of the pipe. Temperature of magnet 250 °C, temperature of sodium 500 °C, flowrate of sodium 10 GPM

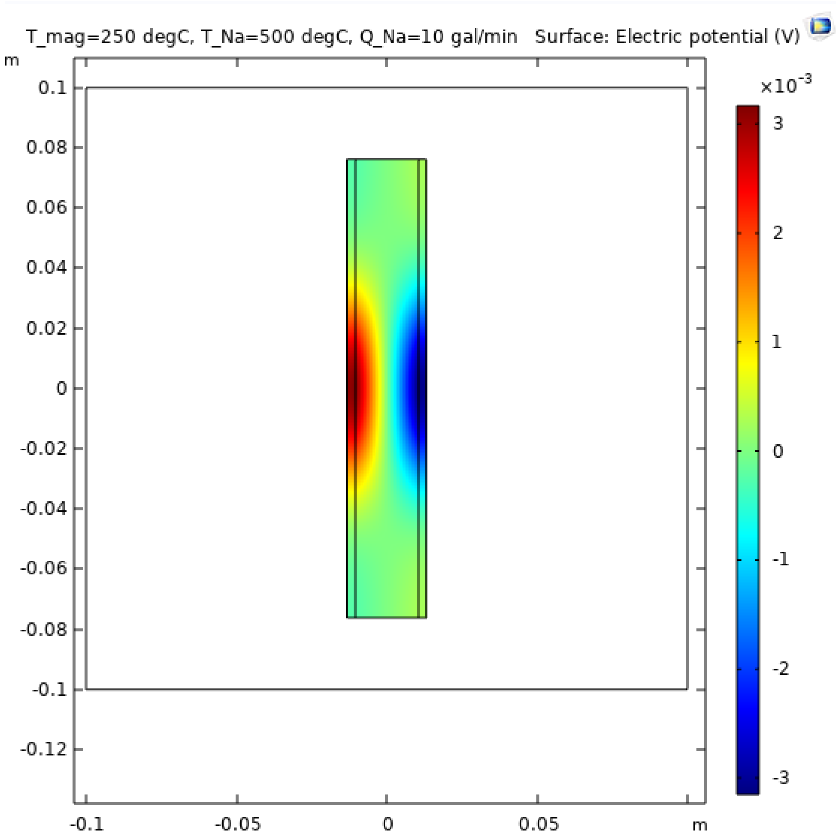

Figure 16: Distributed electrical potential in the plane formed by the two measurement lead locations. Sodium entering the bottom of the pipe. Temperature of magnet 250 °C, temperature of sodium 500 °C, flowrate of sodium 10 GPM

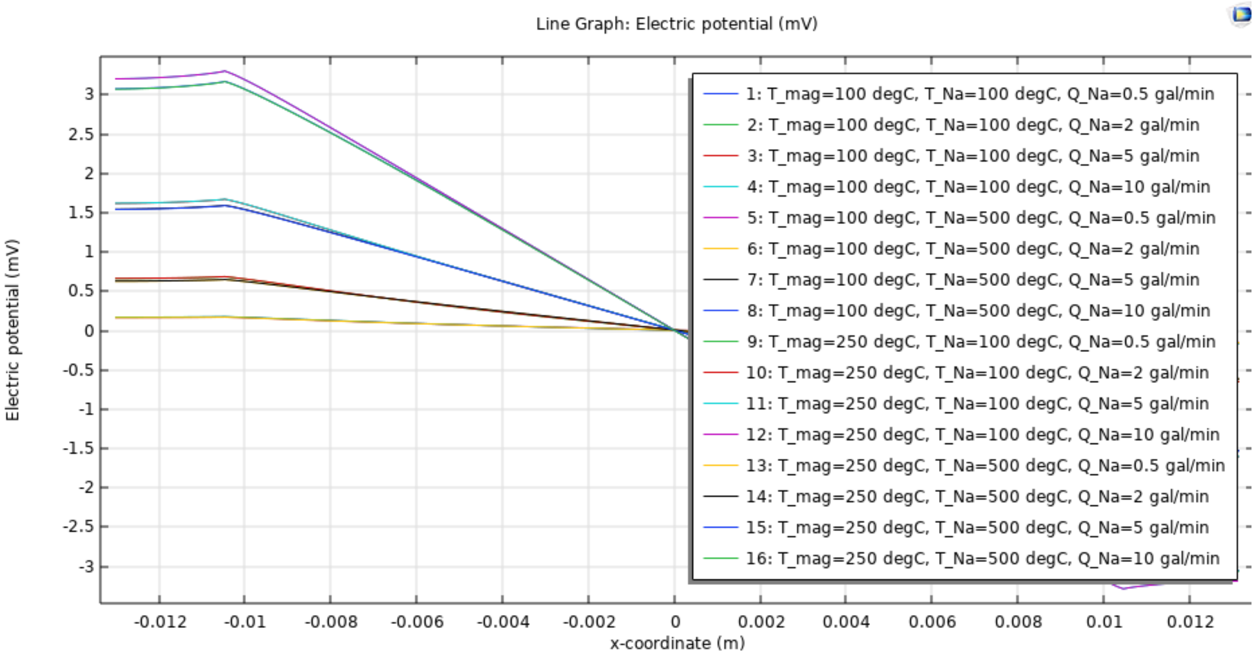

Figure 17: Line graph showing electrical potential for all 16 cases in parametric sweep. Note that data obscured by legend is the negative mirror image of visible data.

The sodium flowrate as a function of FEA calculated induced electric potential across the measurement leads for parameters defined in Table 1 can be found in Figure *18*. As can be seen there is negligible effect from the expected magnet operating temperature over the range of 100-250 °C so it can be ignored. From the FEA simulation results a function was derived to determine sodium flowrate from the sodium temperature, T_{Na}, and measured voltage, V_m, found in Eq. 2.

As mentioned earlier the software based 60 Hz noise rejection appears to provide a satisfactory signal to noise ratio for both the original and auxiliary secondary flowmeters. The auxiliary secondary flowmeter will remain in service and serve as a backup for the original secondary flowmeter and can be used to characterize noise between the two meters.

$$Q[GPM] = \left((1.61E-4)\cdot T_{Na}[^{\circ}\mathrm{C}] + 1.5543\right)\cdot V_m[mV] \tag{2}$$

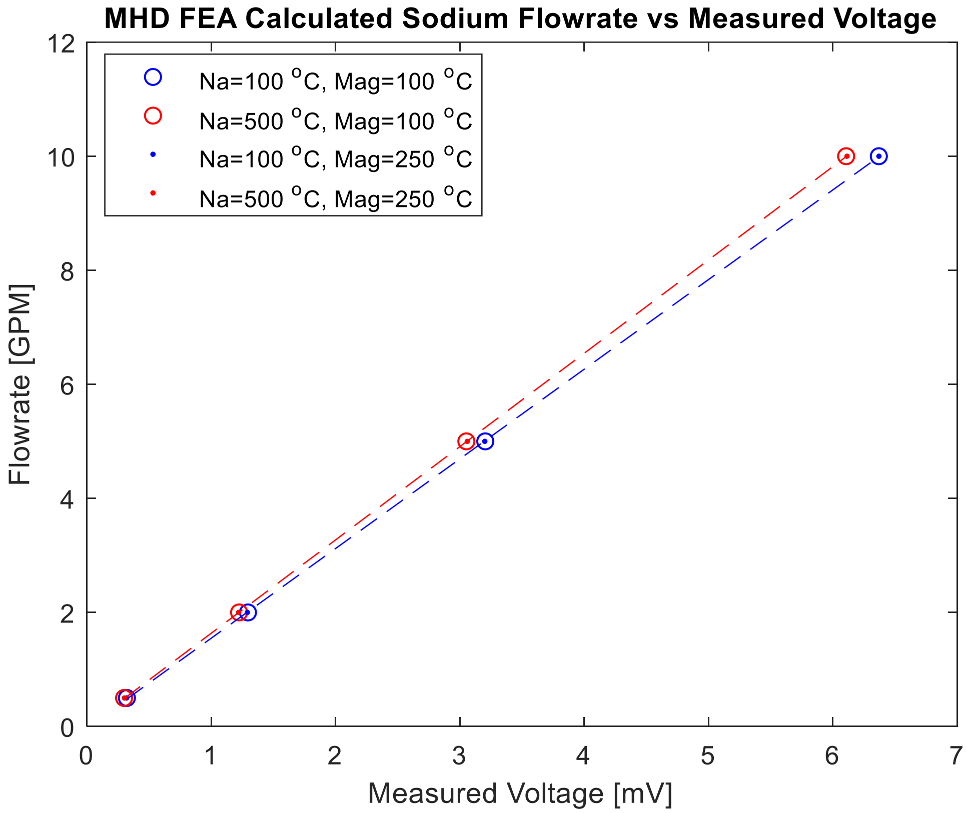

Figure 18*: Sodium flowrate as a function of FEA calculated measured electric potential across the measurement leads*

3. Analysis of THETA Steady State Experimental Data, Test # *2024-05-23-01*

3.1. Test # *2024-05-23-01* Overview

A test with identification *2024-05-23-01* was performed where the primary and secondary systems were brought to steady state at three different core power levels: 5,070, 12,300 and 28,200 W at approximately 50-minute intervals. Throughout the test, the bottom IHX outlet window, located 62.5 [cm] below the bottom of the hot pool redan, was open to allow flow from the IHX shell to the cold pool.

Figure 19 provides the power profile during the test of the measured electric core power, thermal power calculated across the AHX on the sodium side, thermal power calculated across the IHX on the secondary sodium side, and thermal power calculated across the AHX on the air side. The AHX and IHX possess wetted thermocouples on the inlet and outlet and the AHX possesses thermocouples on the inlet and outlet on the air duct which were used in addition to the sodium and air mass flow rate in their respective locations to calculate power. Notice the AHX removes more heat from the secondary sodium than is transferred into the IHX from the primary sodium, especially at higher power levels between 100 and 150 minutes. This is due to the secondary system trace heating and inefficiencies in the AC conduction pump raising the temperature of the secondary sodium between the AHX outlet and the IHX inlet (these two temperatures should be identical in a perfectly adiabatic system). This discrepancy in temperature is seen in Figure 20 where the secondary sodium and air temperatures have been plotted for secondary system components as a function of time.

The AHX blower motor and airspeed have been plotted in Figure 21 for reference. Notice the blower speed needed to be fine tuned with small adjustments between power steps to find steady state. Overhead argon gas pressure in the primary and secondary systems and the laboratory air temperatures were plotted in Figure 22, demonstrating relatively constant conditions throughout the experiment. The AHX ejects hot air into the high bay environment where THETA is located, likely causing the increase in measured laboratory temperature over time.

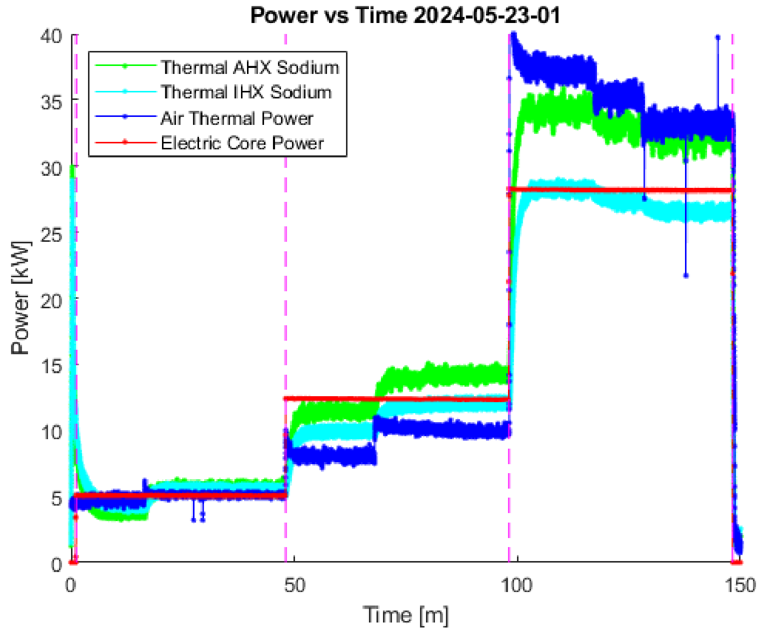

Figure 19: Thermal and electric power as a function of time for Test 2024-05-23-01.

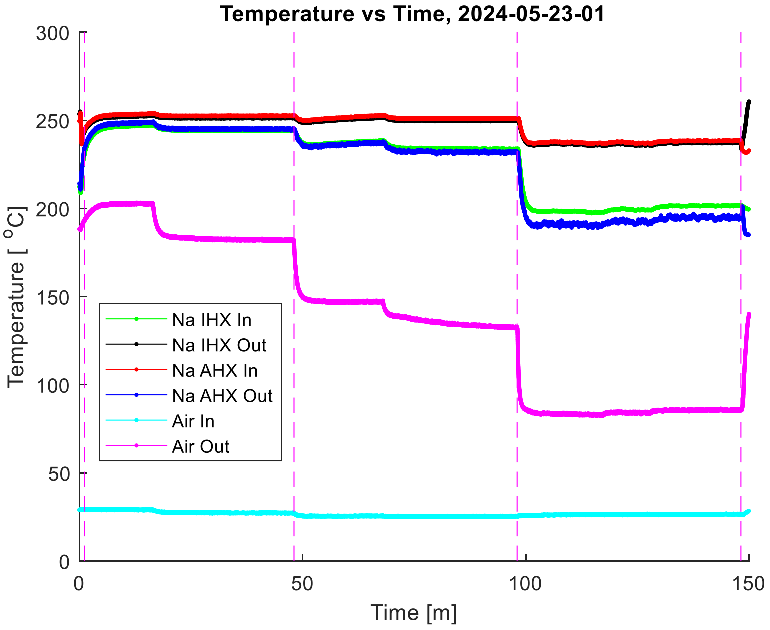

Figure 20: Sodium and air temperatures vs time in the secondary sodium and AHX air duct, respectively

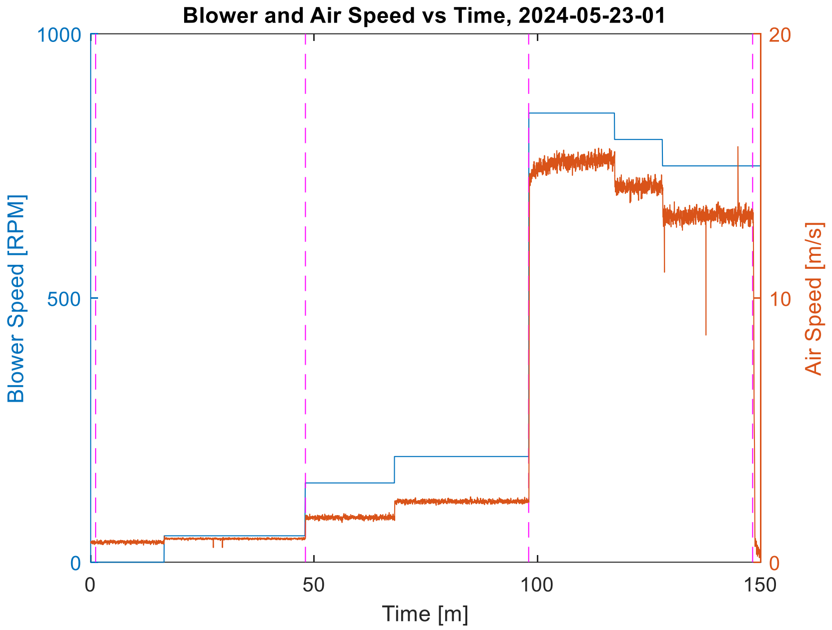

Figure 21: Blower (blue) and air speed (orange) as a function of time

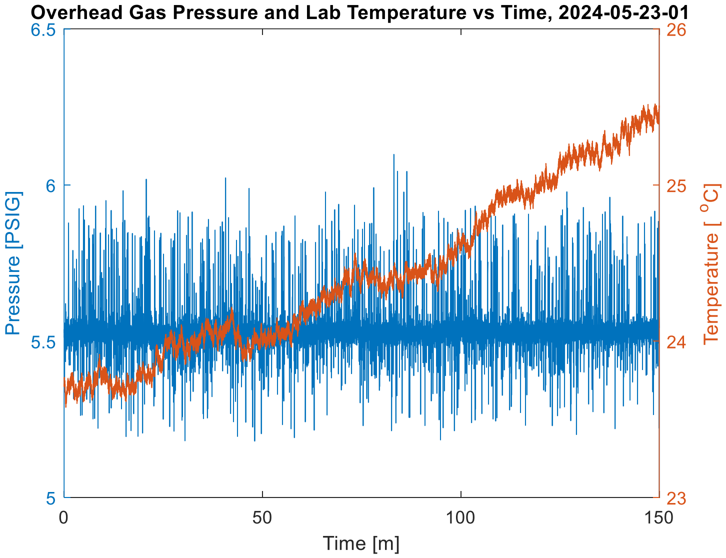

Figure 22: Overhead argon gas pressure in the primary and secondary system (blue) and laboratory air temperature in the vicinity of THETA (orange) as a function of time

During the experiment the primary sodium pump was kept at a constant speed of 950 RPM yielding an approximate flowrate of 12.3 GPM, Figure 23. The secondary AC conduction pump was kept at a constant duty cycle of 55% yielding a flowrate measured by the auxiliary secondary flowmeter of around 10 GPM, Figure 23. The temperature of the primary sodium at the flowmeter and pump inlet have been plotted in Figure 24.

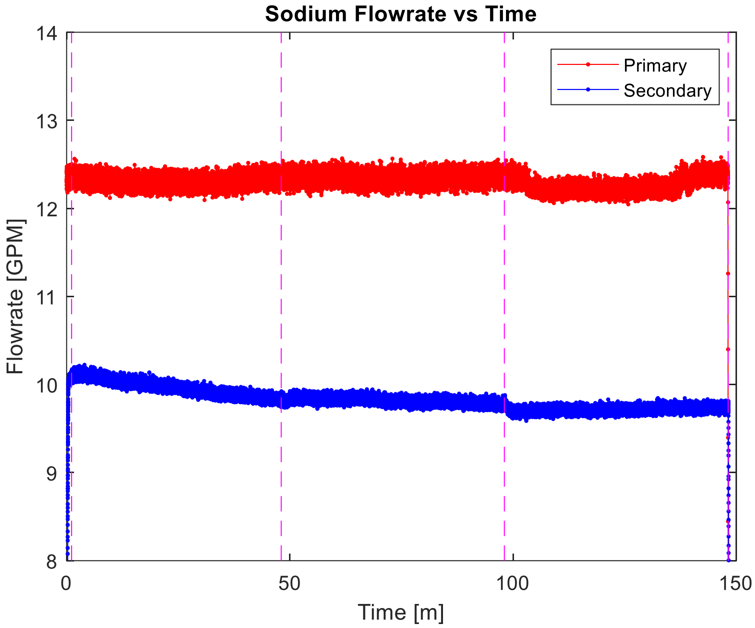

Figure 23: Primary and secondary sodium flowrate as a function of time. Note the secondary flowrate was measured with the auxiliary, clamp on flowmeter as shown in Figure 11

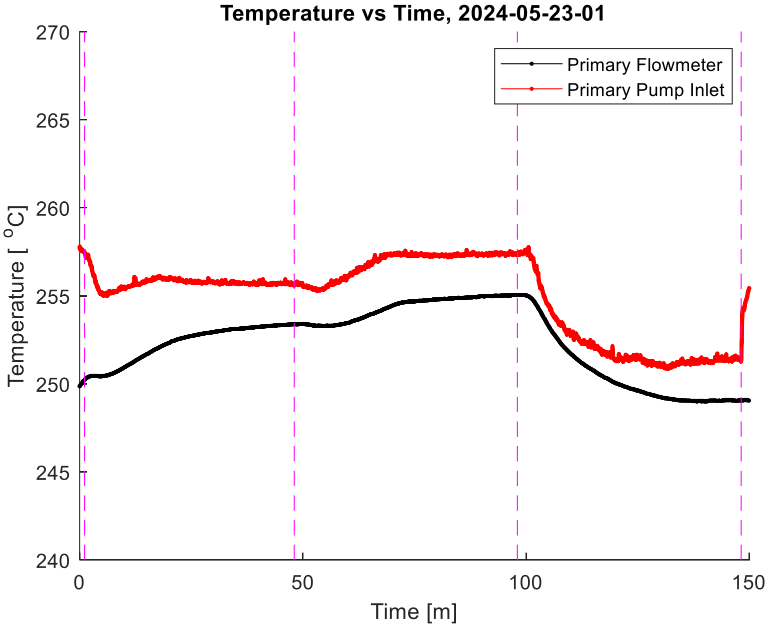

Figure 24: Primary flowmeter and pump inlet temperature as a function of time

Thermocouple rakes are located at positions A,B,C in the hot and cold pool, their locations highlighted in Figure 25. The thermocouple temperatures in the hot and cold pools for positions A,B and C (TCR A/B/C) were plotted in Figure 26, Figure 27, and Figure 28, respectively. Notice the overall thermal stratification between the top of the hot pool (#22) and the bottom of the cold pool (#1) is similar for positions A-C, however, there are discernable temperature differences in certain thermocouple locations. For example, near the bottom of the hot pool the thermocouple junction #14 is markedly colder in position B relative to A, thus the temperature profile is radially complex in addition to the axial thermal stratification. This difference will become more pronounced when the high-resolution optical fiber temperature sensors are analyzed below.

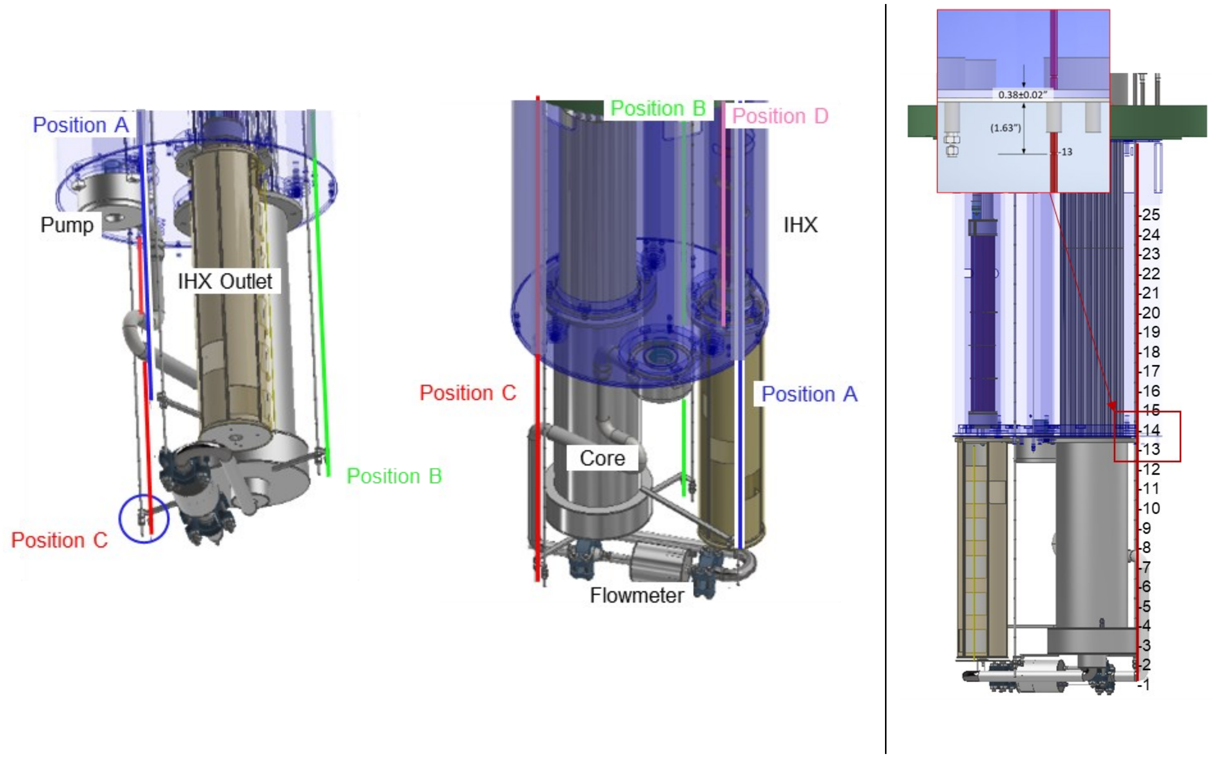

Figure 25: On the left positions A-C labeled where thermocouple rakes (TCR A/B/C) and optical fiber temperature sensors (Fiber A/B/C) are co-located. The thermocouples and fibers run the length of the hot and cold pool, passing through feedthroughs in the bottom of the hot pool redan. The thermocouple and fiber centerline axes are 1.25" from each other. On the right the locations of the 25 junctions for TCR A/B/C have been labeled, where the junction resolution is 2.375" and junction #1 is located 30.13" below the bottom of the redan and junction #13 is the top of the cold pool, 1.63" below the bottom of the redan. Position D is in the shell side of the intermediate heat exchanger and includes a thermocouple rake and fiber.

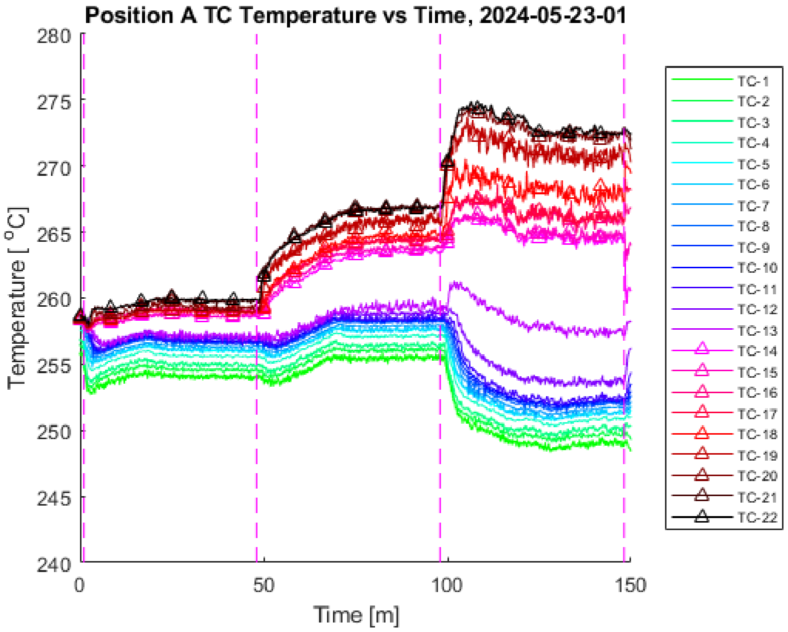

Figure 26: Position A thermocouple temperature as a function of time. Hot pool thermocouple junctions 14-22 are plotted with a triangle marker for clarity

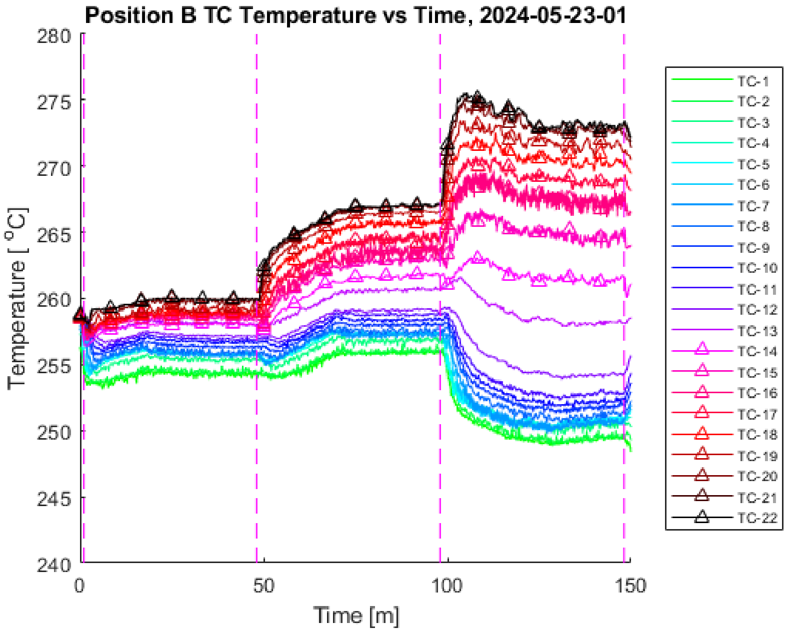

Figure 27: Position B thermocouple temperature as a function of time. Hot pool thermocouple junctions 14-22 are plotted with a triangle marker for clarity

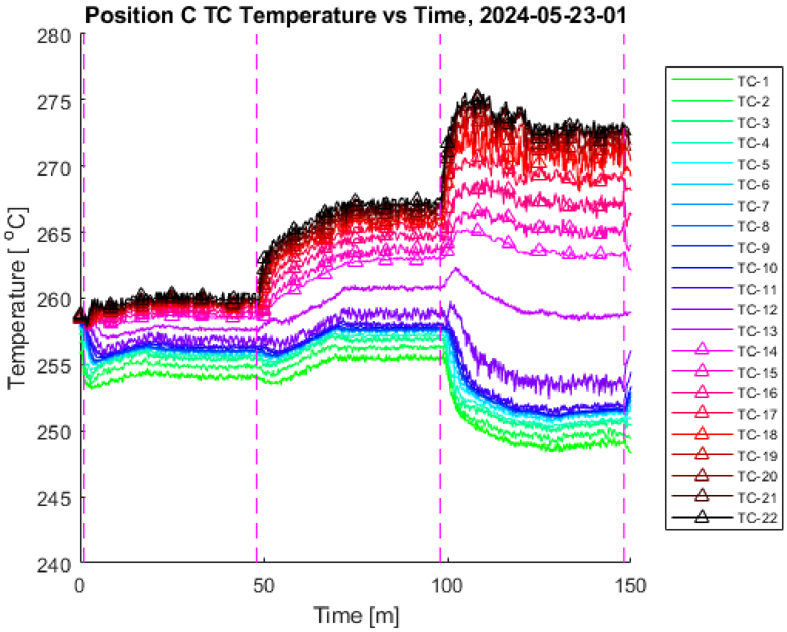

Figure 28: Position C thermocouple temperature as a function of time. Hot pool thermocouple junctions 14-22 are plotted with a triangle marker for clarity

Thermocouple temperatures associated with the core have been plotted in Figure 29. Relative locations for these thermocouples have been included in Figure 30, with more detailed information in Appendix A. The core outlet and core insulator junction #10 thermocouple (TC_HT_OUT and TC_Core in Appendix A) possess large temperature oscillations at power levels above 12,300 W, as can be seen over the time range of 100-150 minutes when the core power was set to 28,200 W. The thermocouple at the center of the core, 3” above the bottom, possesses an oscillation of about +/- 1 °C from 100 to 150 minutes but the thermocouple at the core outlet and the top thermocouple measuring the temperature between the core barrel and core insulator (Core Insulator #10) possesses an oscillation with a range of about +/- 8 °C from 100 to 150 minutes. These two measurements bounce between the Core Insulator #3 and Core Process Ctrl temperature. This suggests some largescale mixing occurring at the outer circumference of the core where cold sodium is sinking down the sides of the core barrel before being entrained in the hot sodium closer to the core center causing thermal striping to occur in this region.

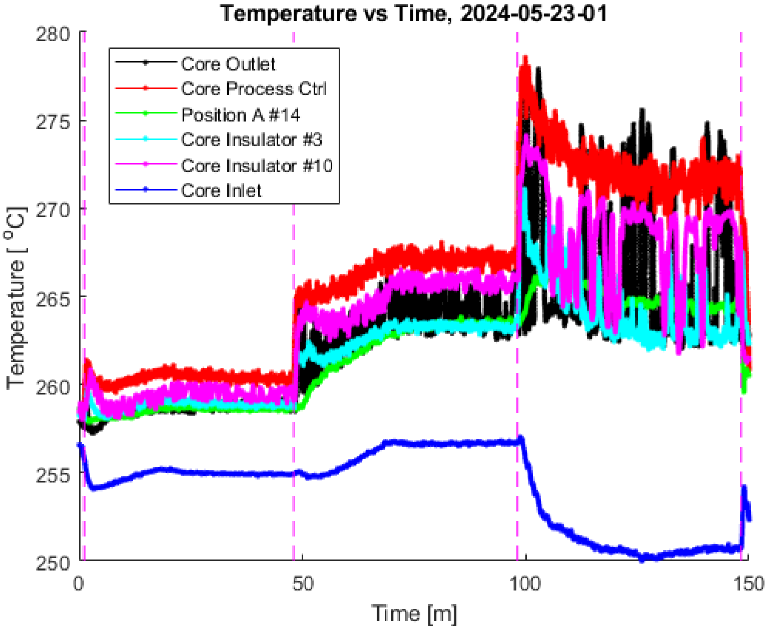

Figure 29: Core temperatures as a function of time. For an overview on the location of the thermocouple measurements see Appendix A

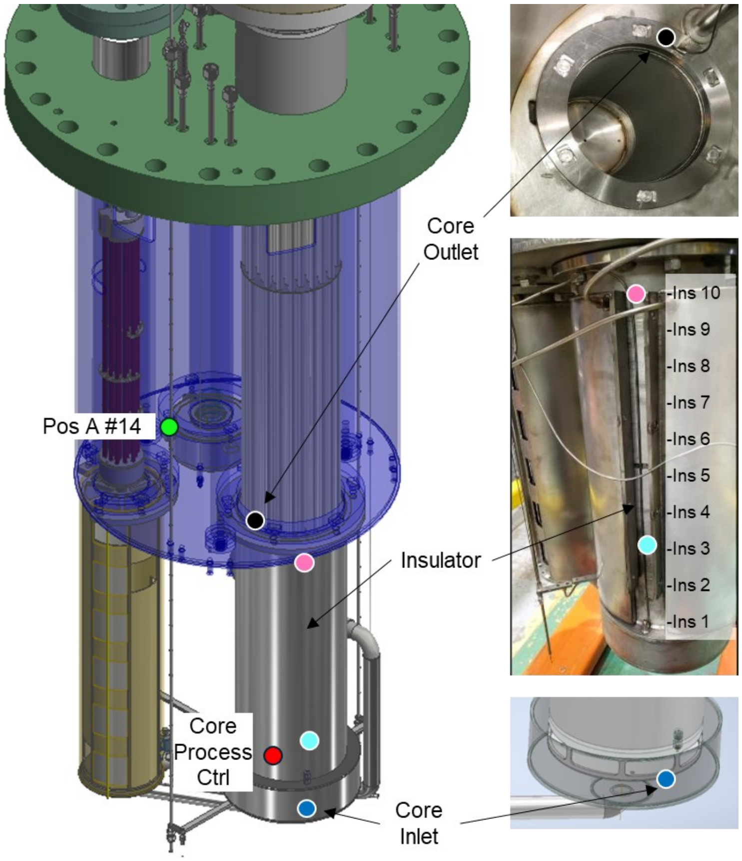

Figure 30: Relative locations of core measurement thermocouples. See Appendix A for more information

3.2. Thermocouple and Optical Fiber Sensor Time Constant

A Rayleigh backscatter based optical frequency domain reflectometry system (Luna Innovations Odisi 6100) was used to acquire distributed frequency shift measurements in single mode silica fibers in the THETA hot and cold pools as well as the intermediate heat exchanger. This frequency shift can be used with a derived correlation to infer distributed temperature, as will be shown later in this report.

The fibers were installed in 21RW (0.0320” OD, 0.0200” ID) stainless steel capillary tubes- these tubes were then slid into 16RW (0.065”+/-0.0005” OD, 0.047” +/-0.0015” ID) 304SS capillary tubes which were installed in the sodium. This double sheath allows for removal of the fiber in case of breakage by removing the inner stainless sheath encasing the fiber. A COMSOL Multiphysics study was performed to assess the time response of the fibers installed in capillary tube. As can be seen in Figure 31, with the optical fiber installed in the outer sheath stainless steel capillary tube (no inner capillary) with helium backfill the time constant with a convective heat transfer boundary condition on the outer capillary tube of 5,000 W/m^{2}K is 275 ms.

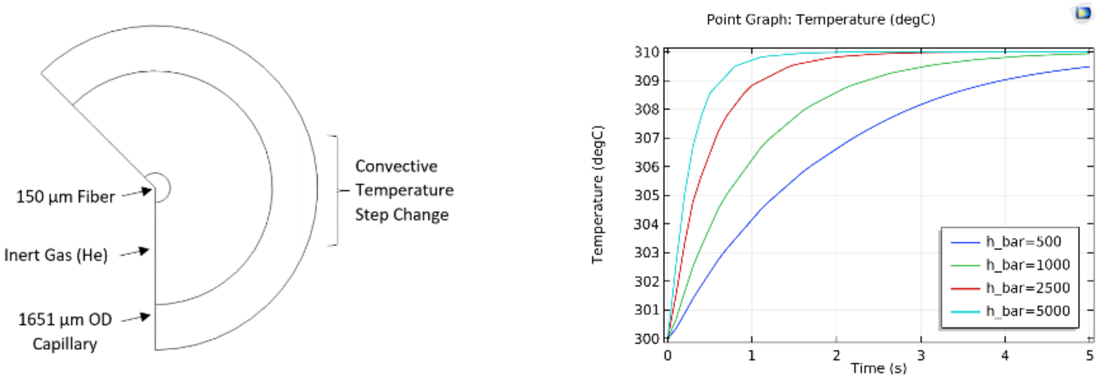

Figure 31: Geometry of axisymmetric finite element analysis to determine fiber in capillary tube time constant, left. Temperature response of optical fiber to step change in surface t4emperatuer of capillary, mean convective coefficients, h_bar, from 500-5000 shown, right.

In order to compare the time response of the optical fiber in capillary to that of an ungrounded K-type thermocouple in sodium, data was taken from literature and interpolated to determine the time constant of the thermocouples used in this work [9]. As can be seen in Figure 32, the time constant for k-type ungrounded thermocouples in flowing sodium at 190 °C has been plotted. The time constant for the 1/8” and ¼” diameter thermocouples used in this work can be approximated as 810-994 ms and 2154-2631 ms, respectively, depending on the treatment of the sheath at the thermocouple junction (swaged vs un-swaged).

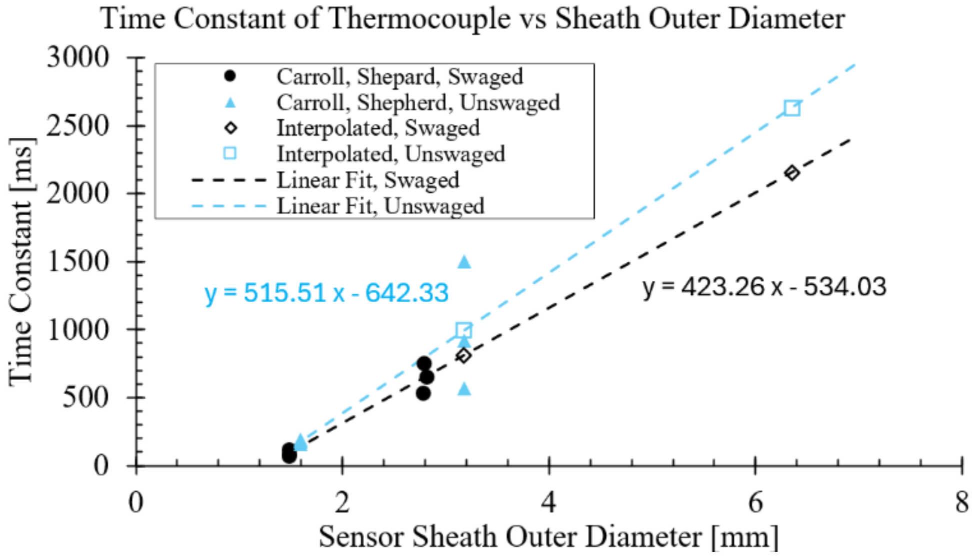

Figure 32: Time constant of K-type ungrounded thermocouple in 190 °C flowing sodium as a function of sensor sheath outer diameter. Thermocouples that were compacted (swaged) demonstrated an improvement in temporal response [9]

3.3. Test # *2024-05-23-01* Optical Fiber Temperature Sensor Data Analysis

The thermocouple temperature as a function of co-located optical fiber frequency shift at positions A, B, and C can be found in Figure 33, where the frequency measurement was taken at the same axial location on the fiber as each of the thermocouple junctions #3-20. Recall from the previous section, the time constant of the fiber in capillary is on the order of 275 ms, while the ¼" diameter thermocouple rake is up to 2631 ms. A smoothing filter was applied to the optical fiber frequency shift data, where a window of 2631 ms was used to average data over a moving window to remove the temperature perturbations with a fast time constant that the thermocouple rake would not pick up. The result of this smoothing filter can be seen in Figure 34 where the correlation between the thermocouple temperature and frequency shift has been improved.

The smoothed data from Figure 34 was used to create quadratic fit correlations between temperature and fiber frequency shift, resulting in three fit curves for positions A, B, and C which were plotted in Figure 35. The quadratic function that determines temperature, *T,* as a function of frequency shift, *S*, has been included in Eq. 3 where the coefficients, *p*, were included for positions A, B and C in Table 2.

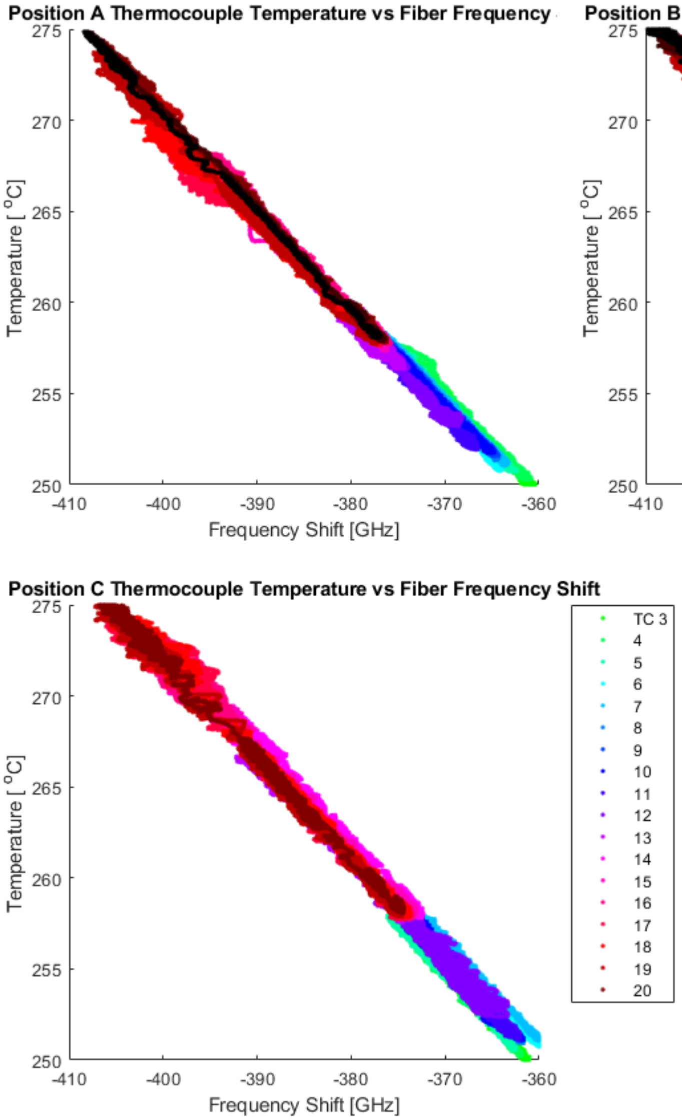

Position A Thermocouple Temperature vs Fiber Frequency

Position B Thermocouple Temperature vs Fiber Frequency

Position C Thermocouple Temperature vs Fiber Frequency Shift

Figure 33: Temperature at thermocouple junctions 3-20 plotted against the fiber gauges at the same vertical elevation for positions A,B,C.

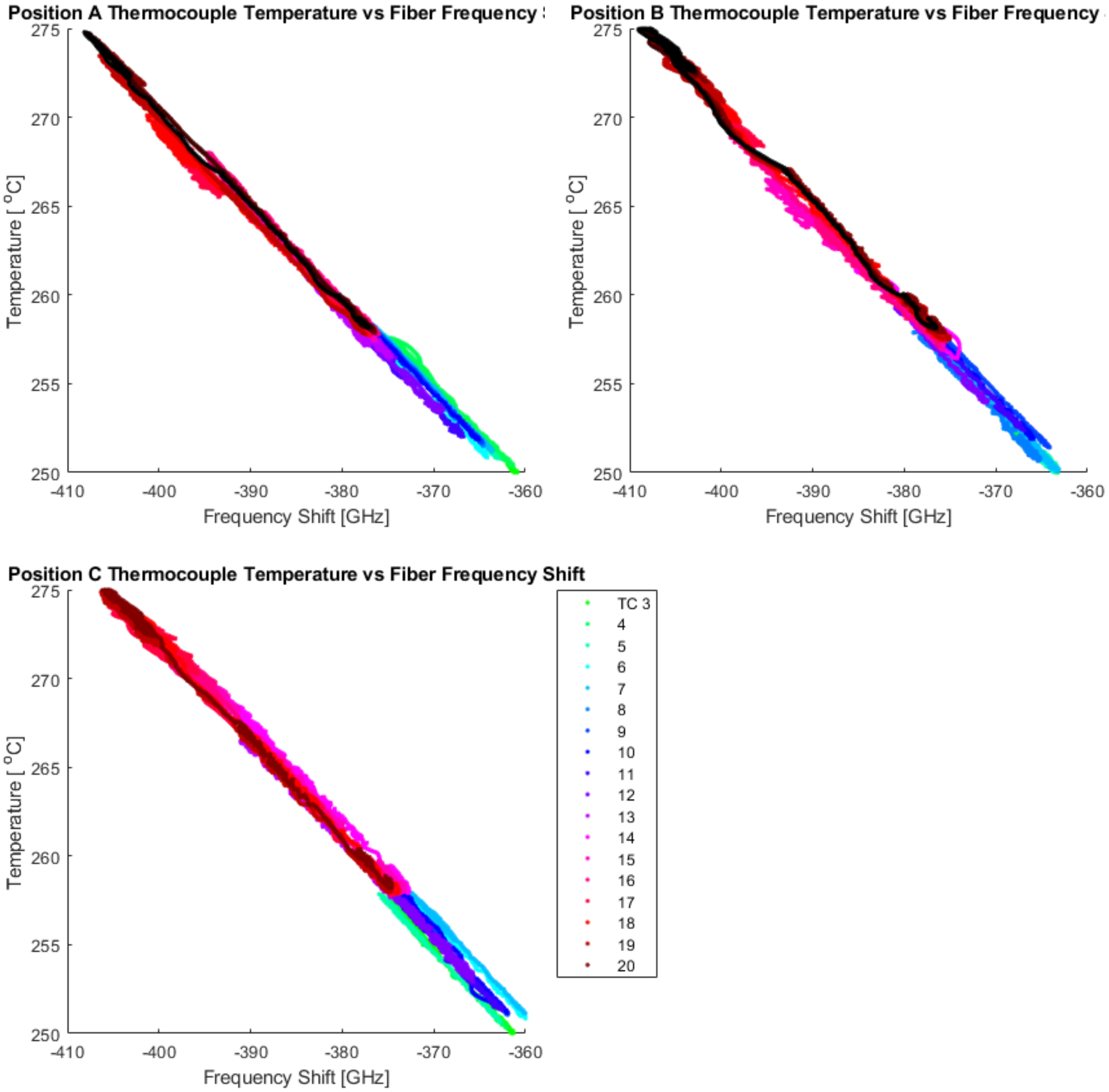

Figure 34: Temperature at thermocouple junctions 3-20 plotted against the fiber gauges at the same vertical elevation for positions A,B,C. Smoothing applied to frequency shift data as a function of time by taking a moving average with window size of 2.63 seconds (time constant of thermocouple)

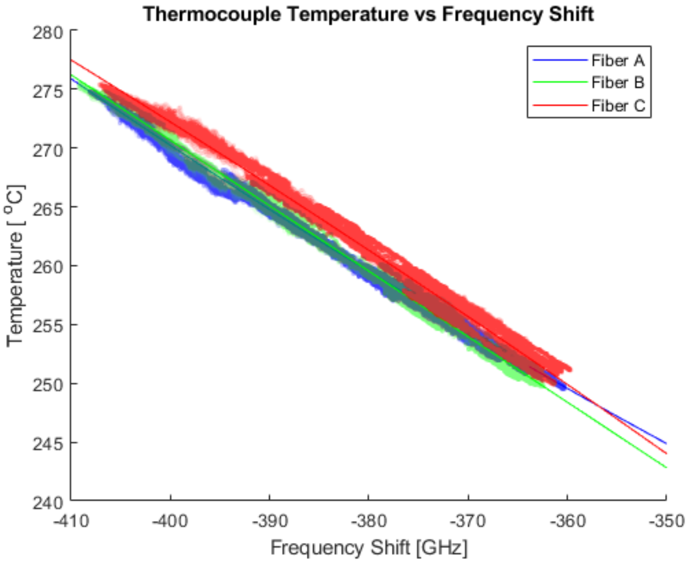

Figure 35: Plotted with transparent dots are each measured thermocouple temperature at positions A, B, C as a function of frequency shift measured by fiber A ,B, C gauge at same axial location in sodium. Also plotted with corresponding color lines are the correlation functions for each fiber position as in Eq. 3 and Table 2

$$T[°\mathrm{C}] = p_1 \cdot (S[GHz])^2 + p_2 \cdot (S[GHz]) + p_3 \tag{3}$$

Table 2: Coefficients for frequency shift to temperature correlation for each fiber position. Also included is the coefficient of determination for each fit

Fiber Position	p_1	p_2	p_3	R^2
A	9.588 E-4	2.117 E-1	201.5	0.9975
B	-1.445 E-5	-5.680 E-1	45.80	0.9976
C	-6.191 E-4	-1.029	-40.16	0.9927
D	5.551 E-4	-1.118 E-1	137.4	0.9868

The fiber at position D (in the IHX shell) was not co-located with a thermocouple in a close enough proximity to perform the same in-situ calibration of frequency shift to temperature as in positions A, B, and C. The center axis of the thermocouple rake in the IHX shell (TC_IHX in Appendix A) was not located close enough to the optical fiber to correlate the high frequency temperature oscillations in the heat exchanger to the fiber. Thus, to fit the measured frequency shift to temperature at the fiber in position D, a quadratic was fit to all of the data from the thermocouple/fiber pairs at positions A, B, and C, Figure 36. The coefficients and coefficient of determination for fiber D shift to temperature correlation can be found in Table 2.

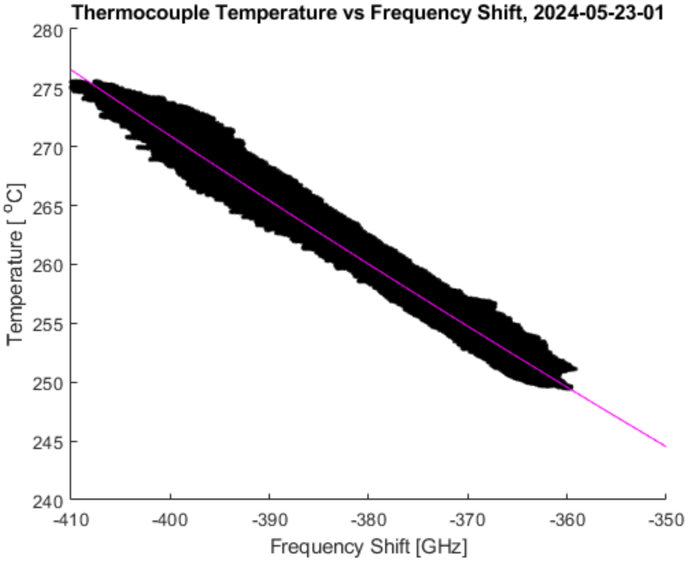

Figure 36: Thermocouple temperature as a function of frequency shift measured with fibers A,B,C. Data used to create fit function for fiber in position D (IHX)

The average thermocouple and fiber temperature for positions A, B, and C for the hot pool over a period of 20 minutes during core power at 28.2 kWe, steady state, can be found in Figure 37 where the y-axis represents the elevation with respect to the bottom of the hot pool redan. As can be seen the thermocouple and fiber data possess good correlation. Note that the hot pool sodium level is located at approximately 55 cm. Thermal stratification exists from 0-30 cm where there is a gradient in temperature of approximately 10 °C. From 30-55 cm there exists little thermal stratification and the hot pool is relatively isothermal.

The average thermocouple and fiber temperatures for positions A, B, and C for the hot pool over a period of 20 minutes for core power at 12,300 and 5,070 W can be found in Figure 37 and Figure 38, respectively. As can be seen for a core power of 12,300 W there exists thermal stratification from 0-30 cm of around 4 °C with an isothermal hot pool from 30-55 cm. The hot pool is relatively isothermal for the lower core power of 5,070 W.

To visualize the thermal stratification in the hot and cold pool for the three core powers the temperature data was normalized using the overall maximum and minimum temperatures for the entire experiment, Figure 40.

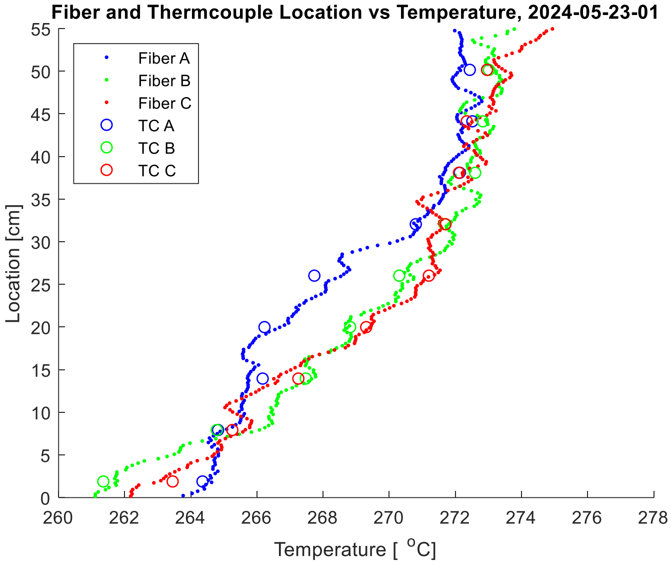

Figure 37: Average fiber and thermocouple temperature of hot pool between 125 and 145 minutes into test (28.2 kW core power at steady state)

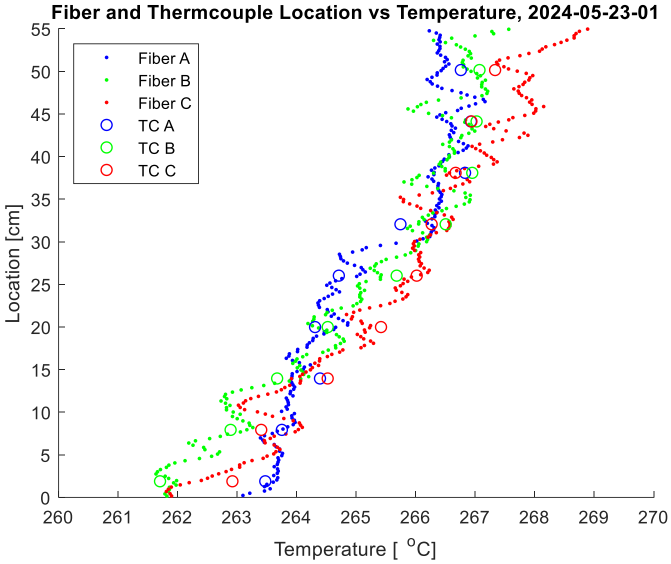

Figure 38: Average fiber temperature of hot pool between 78.3 and 98.3 minutes into test (12.4 kWe core power at steady state)

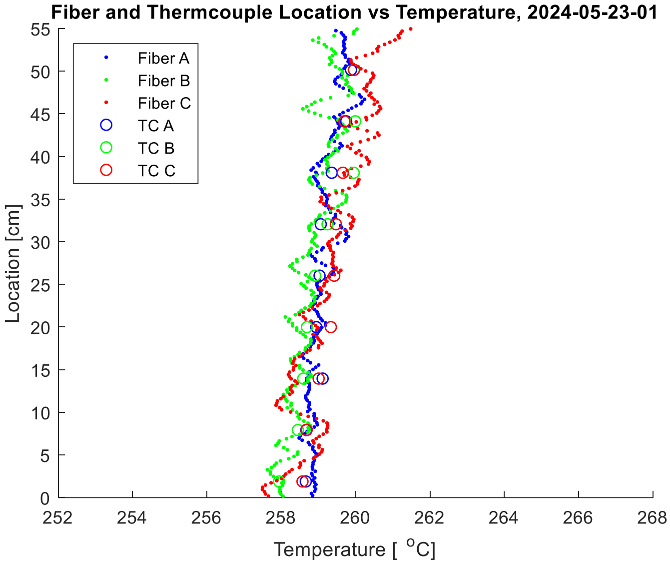

Figure 39: Average temperature of hot pool between 28.3 and 48.3 minutes into test (5,070 W core power at steady state)

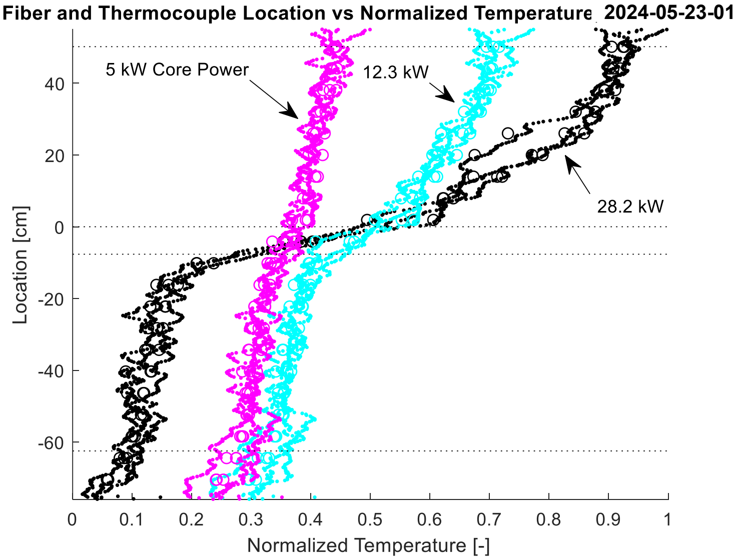

Figure 40: Normalized steady state average thermocouple and fiber temperatures at positions A, B, and C for the three power levels tested. Note the hot pool sodium level (55 cm), bottom of hot pool redan (0 cm), pump inlet (-7.6 cm), and center of bottom IHX outlet window (-62.5 cm) have been labeled with dotted lines.

The thermocouple and corresponding fiber gauge measured temperature for axial positions of 50.2, 32.1, -10.2 and -64.5 cm with respect to the bottom of the hot pool redan at positions A, B, and C have been plotted in Figure 41. As can be seen, the fiber data, plotted in blue, possesses very good correlation to the thermocouple data, in black, over the course of the ~150-minute experiment. There is a slight offset of <= 1°C of the fiber data with respect to the thermocouple data in some of the locations, so a more sophisticated in-situ calibration method may be developed in the future to improve this performance.

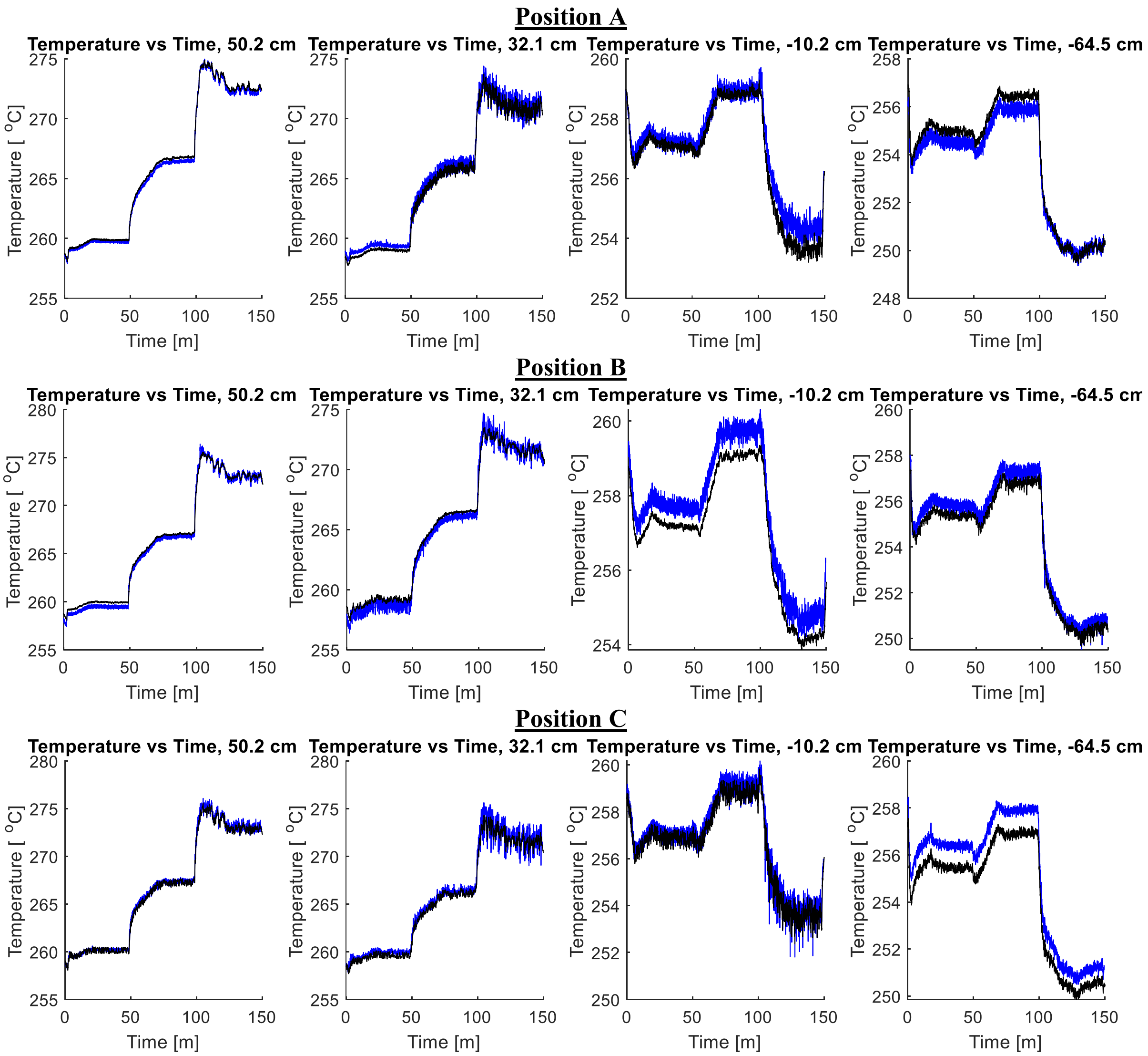

Figure 41: Temperature plotted as a function of time for locations 50.2 cm and 32.1 cm above the bottom of the hot pool redan and 10.2 cm and 64.5 cm below the redan in the cold pool. Thermocouple junction data plotted in black and corresponding fiber gauge location data plotted in blue. Fiber data was fit with Eq. 3 and Table 2

The fiber temperature as a function of position and time for positions A, B, and C between 97 and 150 minutes into the test has been plotted in Figure 42. The pool level, center of IHX shell inlet window and high core power start time have been plotted with magenta dotted lines for reference. At sensor position B there exists a cool region near the bottom of the hot pool. As seen in Figure 25, position B is located between the core and the IHX- the cold region is likely a stagnant region that the plume from the top of the core is not readily injecting hot sodium into as most of the flow is transported to the top of the hot pool before falling down. This region is cooled by the IHX, resulting in a cold volume.

Stratification is apparent from 0-30 cm and temperature oscillations exist at the thermocline at 30 cm. The oscillations seem to be the most aggressive and over the largest axial region in position C. In order to analyze the magnitude of oscillation, the standard deviation of the temperature over a moving one-minute window with respect to time can be found in Figure 43. Indeed, the magnitude and axial distribution of temperature oscillation is greatest at position C. Also apparent is the interaction of the cold region in position B with the rest of the relatively warmer hot pool, creating a region of thermal striping at 7 cm.

The range of the temperature over a moving one-minute window with respect to time can be found in Figure 44. Similar to the standard deviation, the range highlights regions of thermal striping at the thermocline at 30 cm and at the cold volume at 7 cm in position B.

The fiber temperature as a function of position and time for the cold pool region during the high core power (97-150 minutes) for positions A, B, and C can be found in Figure 45. Magenta dotted lines display the vertical location of the pump inlet and center of the IHX window outlet at 7.67 cm and 62.5 cm, respectively. A magenta line also shows the time at 98.06 minute when the core power is increased from 12.3 to 28.2 kW. As can be seen the temperature profiles for the positions are similar and a thermocline with a high degree of thermal stratification exists near the axial position of the pump inlet.

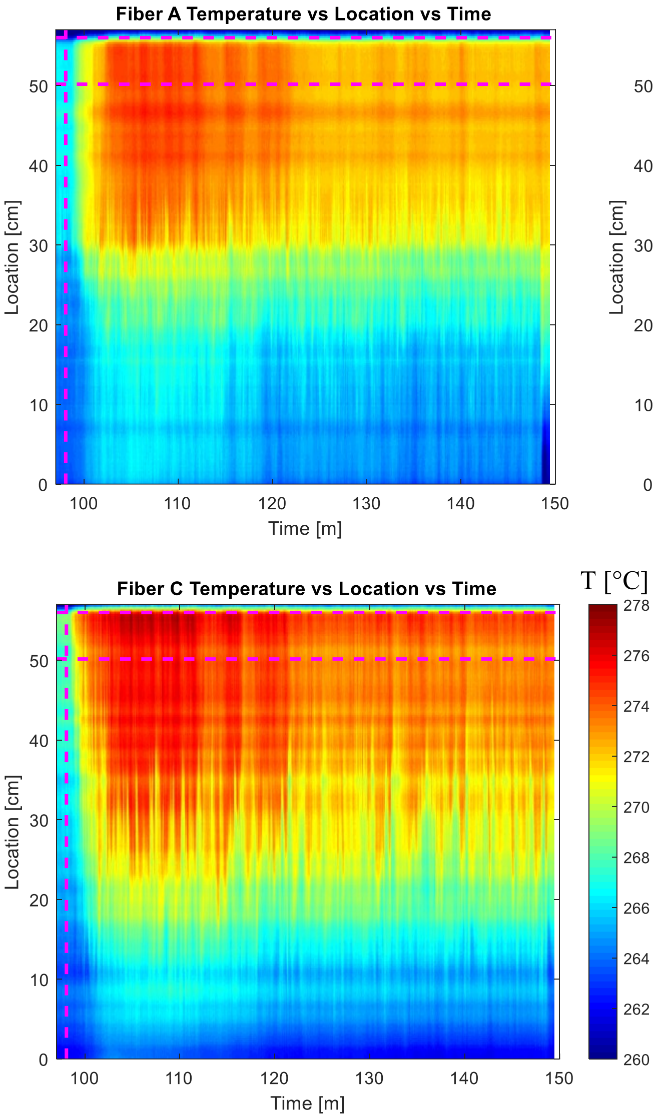

Figure 42: Hot pool optical fiber temperature as a function of location and time during high core power. Magenta dotted lines show the position of the top of the hot pool sodium as well as the center of the IHX shell inlet at 56 cm and 50.17 cm, respectively. Magenta line also shows the time at 98.06 minute when the core power is increased from 12.3 to 28.2 kW.

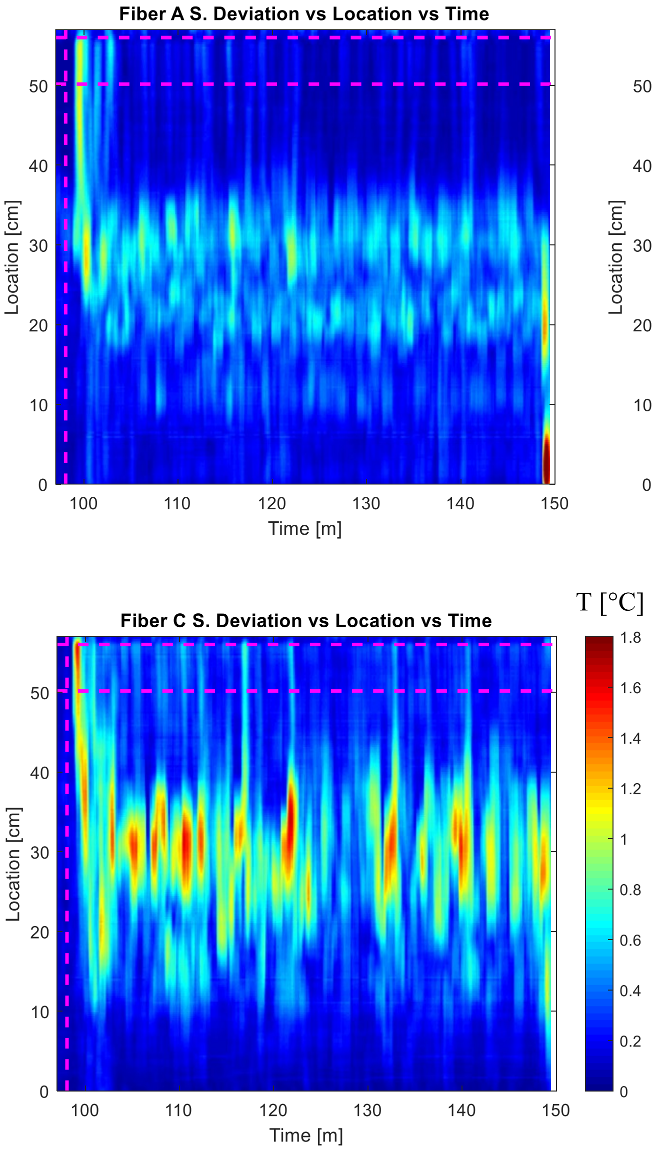

Figure 43: Hot pool optical fiber temperature standard deviation over 1 minute window as a function of location and time during high core power. Magenta dotted lines show the position of the top of the hot pool sodium as well as the center of the IHX shell inlet at 56 cm and 50.17 cm, respectively. Magenta line also shows the time at 98.06 minute when the core power is increased from 12.3 to 28.2 kW.

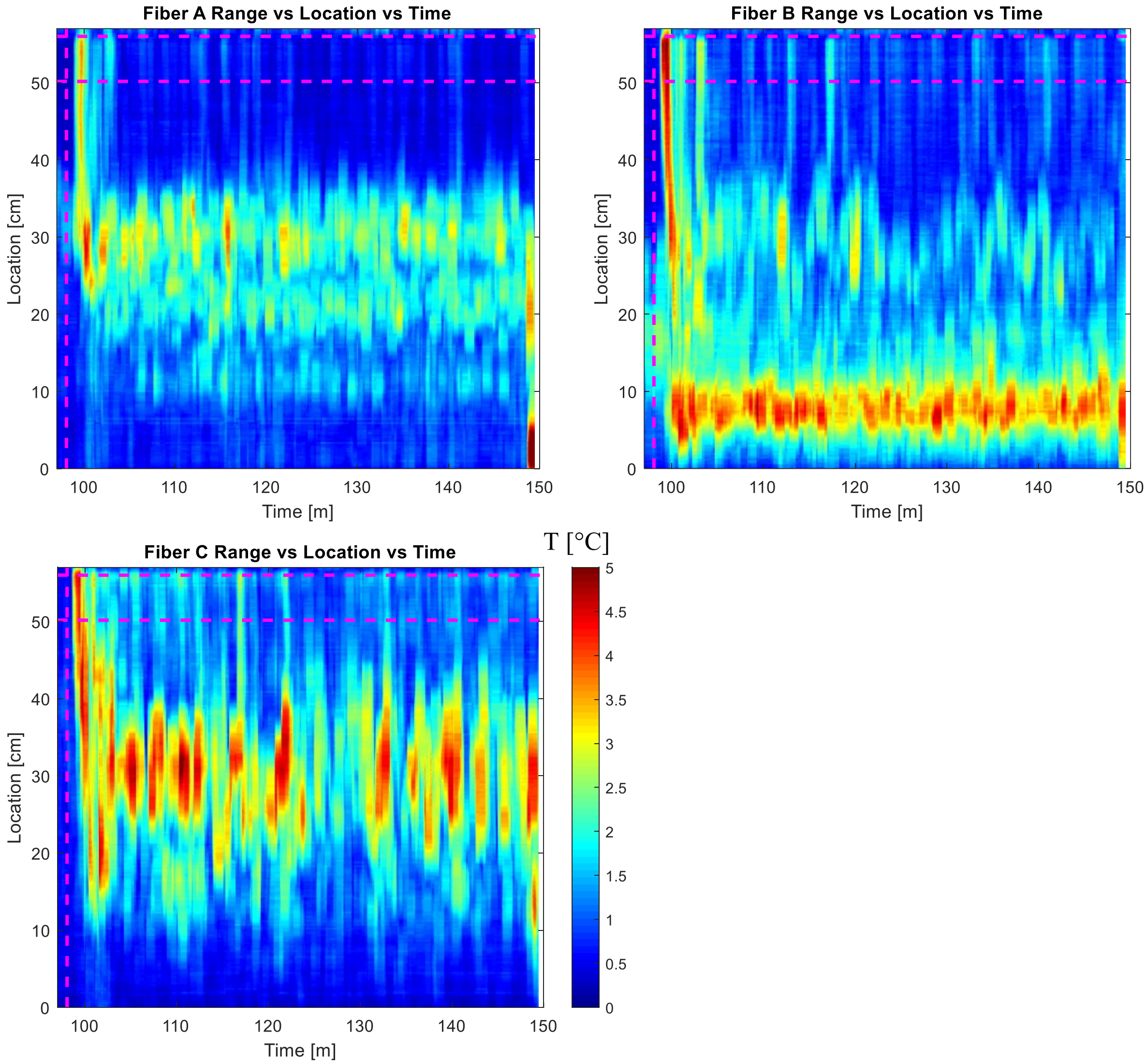

Figure 44: Hot pool optical fiber temperature range over 1 minute window as a function of location and time during high core power. Magenta dotted lines show the position of the top of the hot pool sodium as well as the center of the IHX shell inlet at 56 cm and 50.17 cm, respectively. Magenta line also shows the time at 98.06 minute when the core power is increased from 12.3 to 28.2 kW.

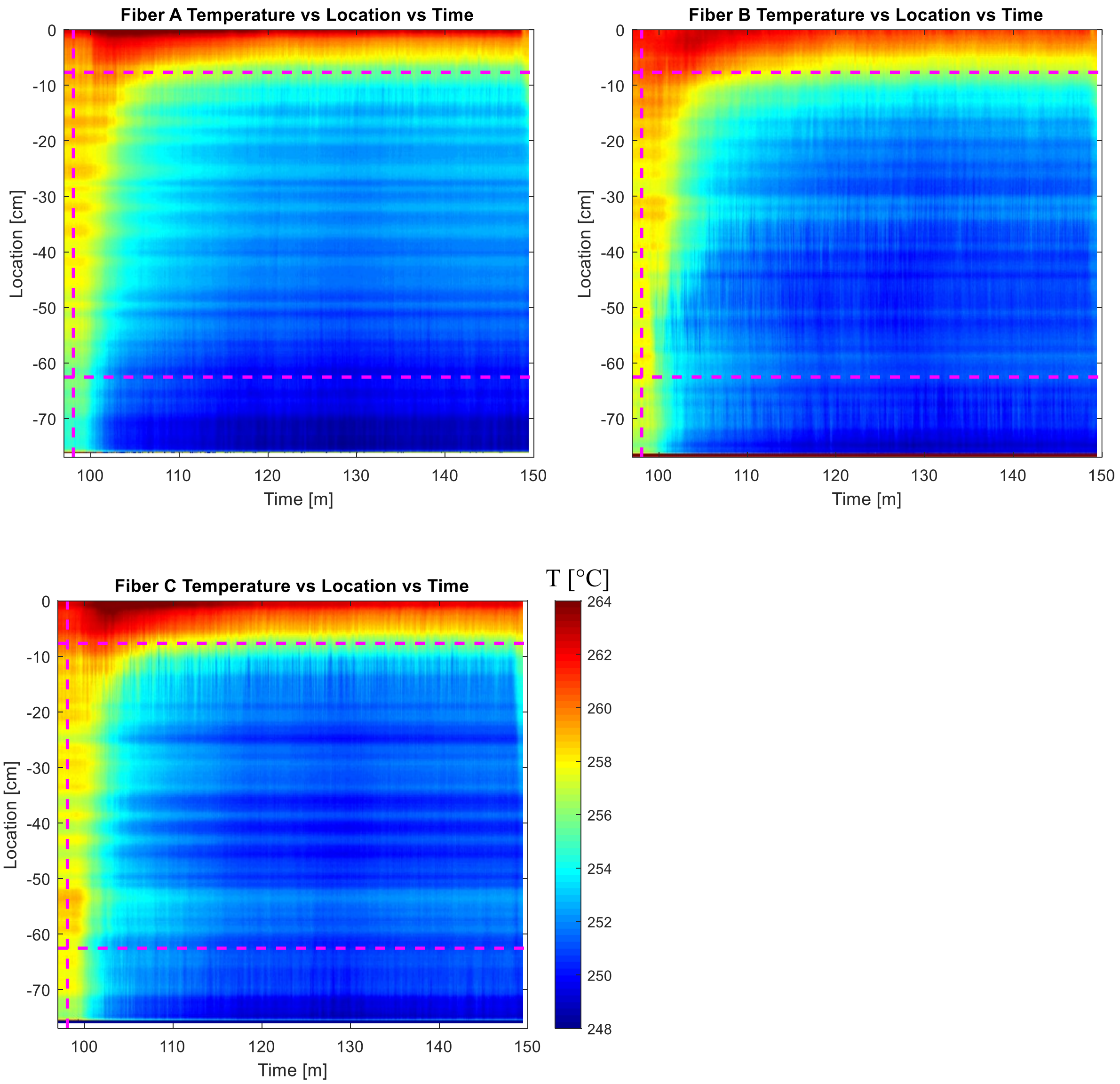
Fiber A Temperature vs Location vs Time

Fiber B Temperature vs Location vs Time

Fiber C Temperature vs Location vs Time

Figure 45: Cold pool optical fiber temperature as a function of location and time during high core power. Magenta dotted lines display the vertical location of the pump inlet and center of the IHX window outlet at 7.67 cm and 62.5 cm, respectively. Magenta line also shows the time at 98.06 minute when the core power is increased from 12.3 to 28.2 kW.

A multijunction thermocouple probe is located in the primary sodium shell of the intermediate heat exchanger (IHX), Figure 46. As can be seen the thermocouple at junction 1 is located at the top of the bottom ‘collector cylinder’ where the downcomer sodium turns around and enters the upcomers. Junction 11 is at the center of the IHX inlet window and junction 12 is near the top of the sodium pool level. The thermocouple rake possesses a resolution of 1.75” between junctions. Figure 47 provides the IHX shell thermocouple junction temperatures as a function of time throughout the experiment.

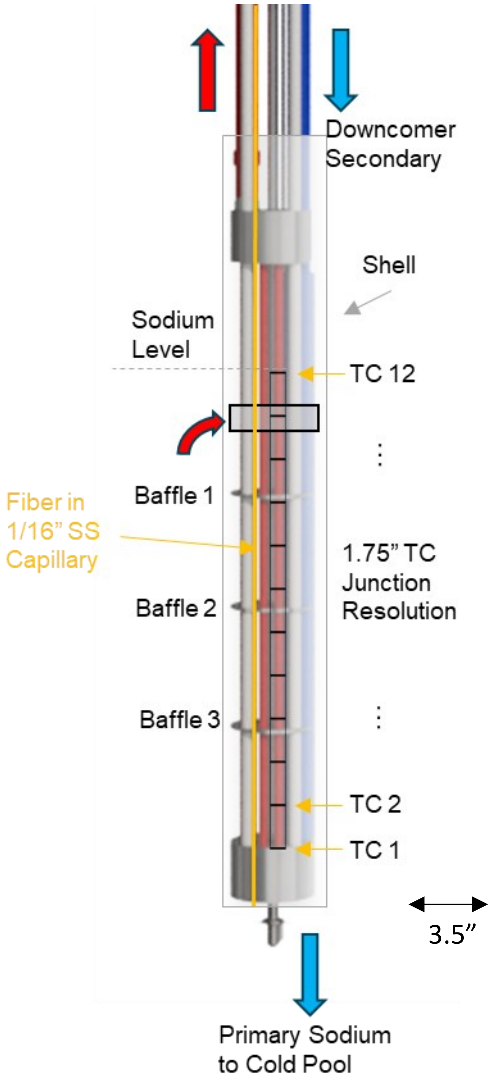

Figure 46: Locations of features, thermocouple junctions, and optical fiber in the IHX. ~3.5” arrow shown for scale.

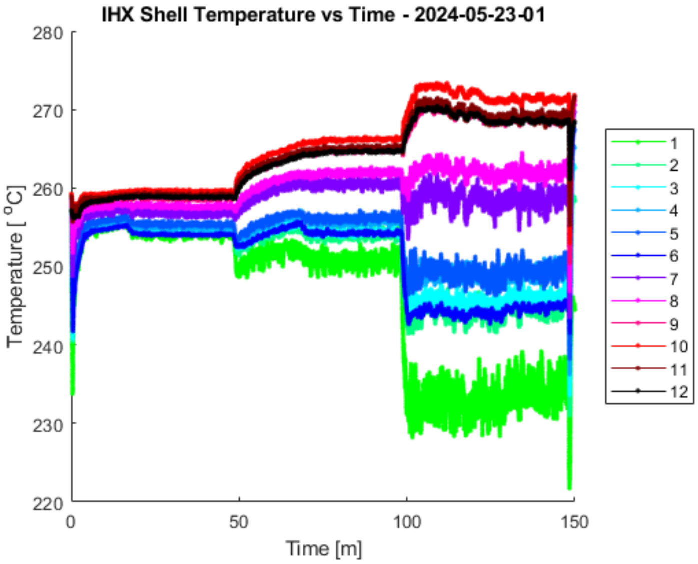

Figure 47: Intermediate heat exchanger primary sodium in shell temperature vs time

An optical fiber is located in ‘position D’ in the IHX primary sodium shell side, running along the same length as the multijunction thermocouple probe just discussed, where the center line of the fiber axis is 2” from the center of the thermocouple probe. The IHX shell thermocouple temperature was plotted as a function of position D fiber frequency shift, Figure 48. As can be seen, the fit line (Figure 36 and Table 2) for position D fiber was also plotted. There is poor correlation between the fiber and thermocouple in this region due to the relatively larger distance between sensor centerline axes for a system with high thermal complexity both spatially and temporally. This does not mean the fiber is measuring temperature less accurately, only that an in-situ calibration with the co-located thermocouple is not advisable, thus as previously described the frequency to temperature quadratic correlation was derived with data from the co-located thermocouples and fibers at positions A, B, and C.

The average temperature of the IHX fiber and thermocouple probe has been plotted for high, medium, and low core power steady state in Figure 50, Figure 51, and Figure 52, respectively. The locations of the collector cylinder, baffles, IHX window center, and sodium hot pool level were provided with gray dashed lines. As can be seen at all power levels there exist sharp temperature gradients at locations where the baffle plates and collector cylinder exist as trapped volumes of primary sodium are mixed between these features becoming somewhat isothermal giving a ‘stair-step’ like profile to the axial temperature distribution.

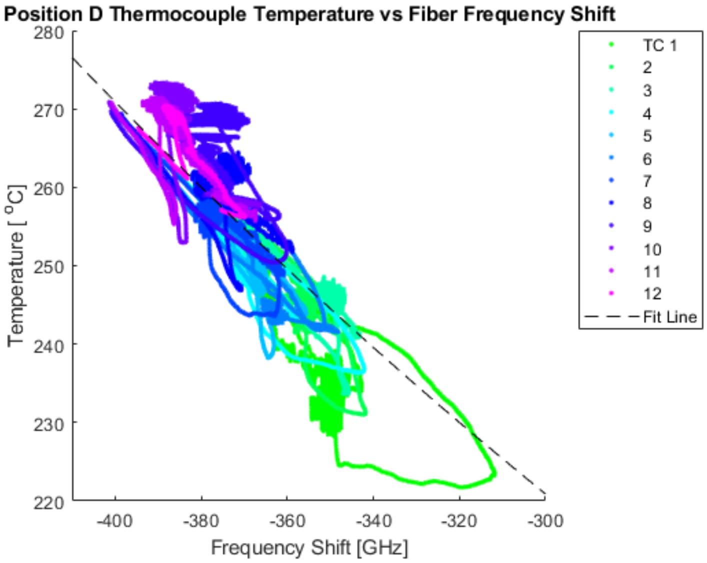

Figure 48: Thermocouple temperature plotted as a function of frequency shift for position D in the shell side of the IHX. Note the fit line derived in Figure 36 included with a black dashed line for reference.

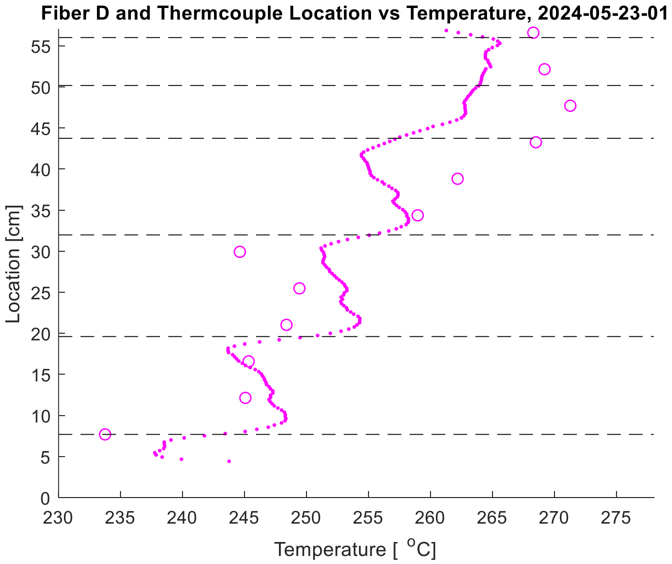

Figure 49: Average temperature of IHX between 125 and 145 minutes (high core power at steady state). Optical fiber measurements shown with small magenta dots, thermocouple measurements plotted with magenta circles. Highlighted with gray dashed lines are the top of the bottom collector cylinder (7.70 cm), the bottom baffle (19.6 cm), the middle baffle (32.0 cm), the top baffle (43.7 cm), the center of the shell inlet (50.2 cm) and the approximate location the height of the hot pool sodium (56 cm).

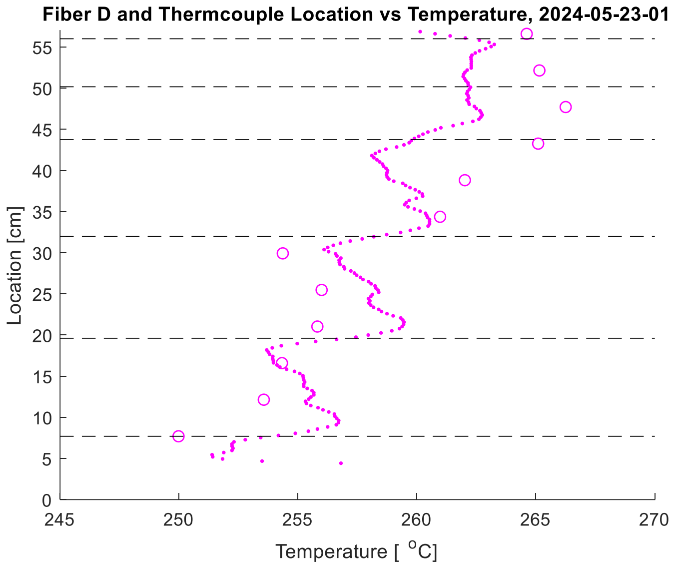

Figure 50: Average temperature of IHX between 78.3 and 98.3 minutes (medium core power at steady state). Optical fiber measurements shown with small magenta dots, thermocouple measurements plotted with magenta circles. Highlighted with gray dashed lines are the top of the bottom collector cylinder (7.70 cm), the bottom baffle (19.6 cm), the middle baffle (32.0 cm), the top baffle (43.7 cm), the center of the shell inlet (50.2 cm) and the approximate location the height of the hot pool sodium (56 cm).

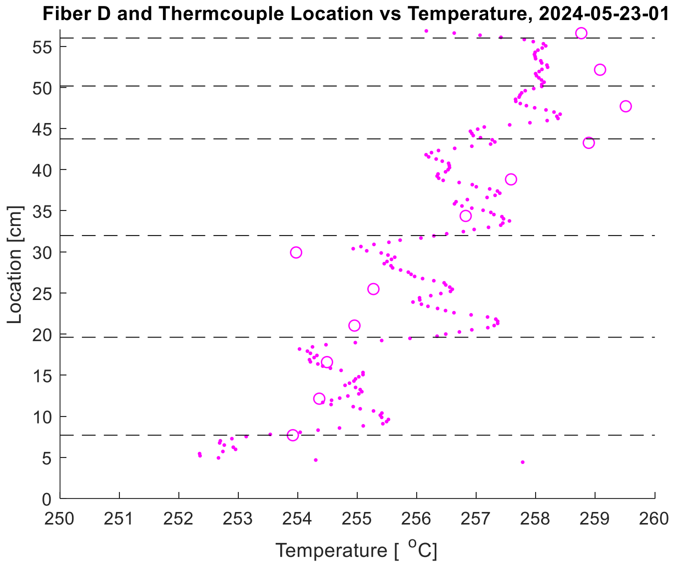

Figure 51: Average temperature of IHX between 28.3 and 48.3 minutes (low core power at steady state). Optical fiber measurements shown with small magenta dots, thermocouple measurements plotted with magenta circles. Highlighted with gray dashed lines are the top of the bottom collector cylinder (7.70 cm), the bottom baffle (19.6 cm), the middle baffle (32.0 cm), the top baffle (43.7 cm), the center of the shell inlet (50.2 cm) and the approximate location the height of the hot pool sodium (56 cm).

The fiber temperature as a function of location and time in the IHX has been provided in Figure 52. A stairstep profile in temperature with isothermal regions of sodium between obstructions (baffles, collector cylinder) is apparent. A large amount of oscillation in temperature exists at the top baffle plate (43.7 cm). Figure 53 provides the standard deviation as a function of location and time for the optical fiber, using a 1-minute moving time window. As can be seen, the standard deviation is highest at the top baffle, especially when the high-power regime begins at ~98 minutes. Figure 54 provides the temperature range as a function of location and time over a 1-minute moving window. Thermal striping at the baffle plates is readily apparent.

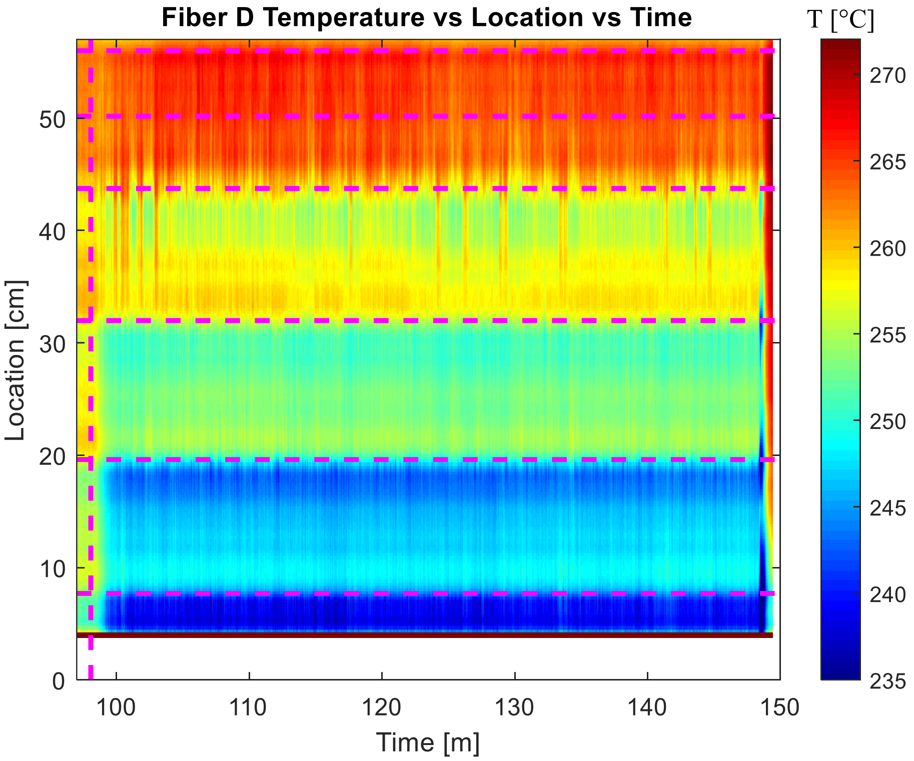

Figure 52: Temperature vs location vs time for optical fiber in position D (IHX primary shell sodium). Magenta lines display the location of the top of the bottom collector cylinder (7.70 cm), the bottom baffle (19.6 cm), the middle baffle (32.0 cm), the top baffle (43.7 cm), the center of the shell inlet (50.2 cm) and the approximate location the height of the hot pool sodium (56 cm) . Magenta line also shows the time at 98.06 minute when the core power is increased from 12.3 to 28.2 kW.

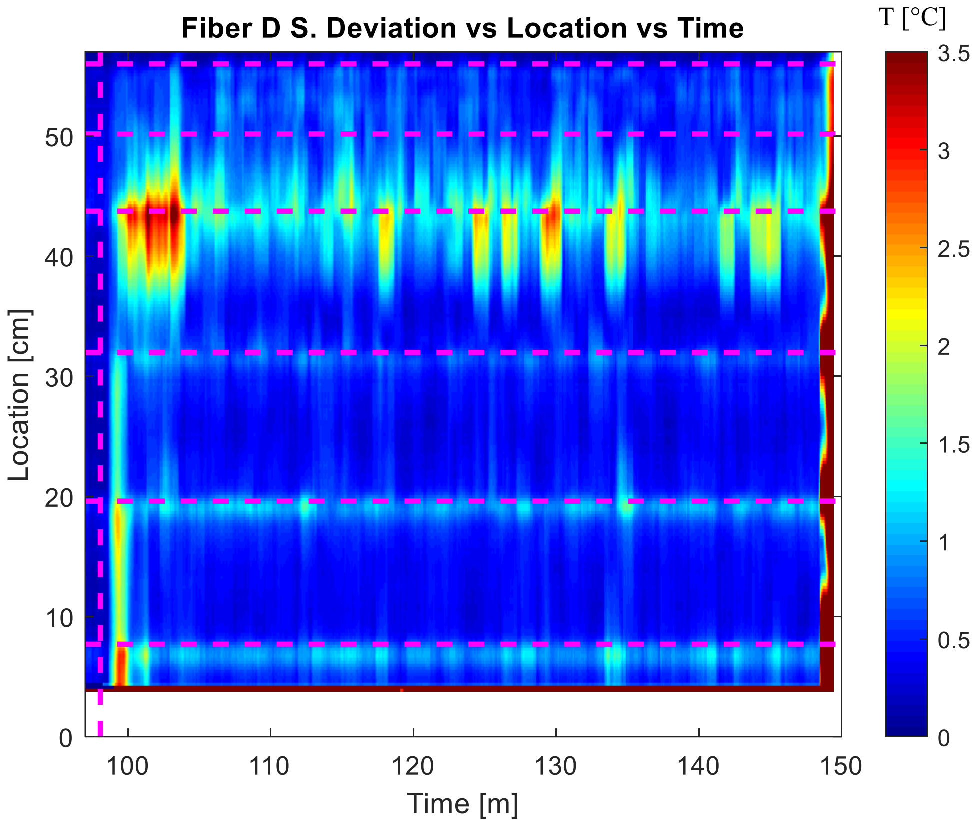

Figure 53: Temperature standard deviation over 1 minute window vs location vs time for optical fiber in position D (IHX primary shell sodium). Magenta lines display the location of the top of the bottom collector cylinder (7.70 cm), the bottom baffle (19.6 cm), the middle baffle (32.0 cm), the top baffle (43.7 cm), the center of the shell inlet (50.2 cm) and the approximate location the height of the hot pool sodium (56 cm). Magenta line also shows the time at 98.06 minute when the core power is increased from 12.3 to 28.2 kW.

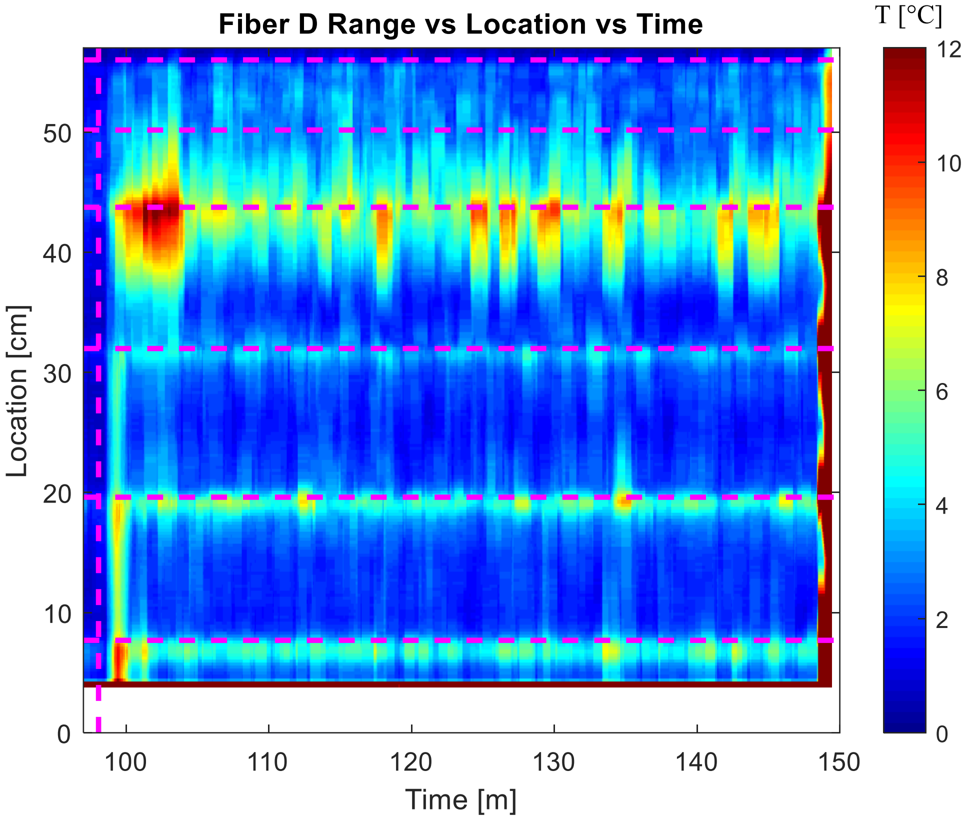

Figure 54: Temperature range over 1 minute window vs location vs time for optical fiber in position D (IHX primary shell sodium). Magenta lines display the location of the top of the bottom collector cylinder (7.70 cm), the bottom baffle (19.6 cm), the middle baffle (32.0 cm), the top baffle (43.7 cm), the center of the shell inlet (50.2 cm) and the approximate location the height of the hot pool sodium (56 cm). Magenta line also shows the time at 98.06 minute when the core power is increased from 12.3 to 28.2 kW.

4. CRADA 2021-21121 Oklo Testing

4.1. Overview of Experimental Test Matrix

A test matrix was developed by Argonne and Oklo engineers as part of a CRADA to acquire experimental data for code validation. Table 3 provides an overview of all of the testing performed, which included over 100 tests over the span of 91.3+ hours. The testing was broken down into Phases 1-7, where most of the tests in each phase were completed in identical Sets to characterize repeatability and assess the environmental effects on test data (laboratory temperature, etc.).

Table 3: High level overview of testing for CRADA 2021-21121

Phase	Description	Number of Unique Tests	Avg Time/ Test [hr]	Total Tests	Total Duration [hr]
1	Thermal stratification at nominal conditions	12	1	24	24
1.5	Characterization of core wall insulation	6	1	12	12
2	Secondary system characterization	4	1	7	7
3	Natural circulation startup flow conditions	10	0.6	20	12
4	Power level transient flow behavior	12	1	24	24
5	Flow behavior due to loss of heat sink / loss of flow	4	1	8	8
6	System-wide thermal hydraulic response	2	1	4	4
7	Characterization of core temperature oscillation	1	.3	1	.3
			Total:	100 Tests	91.3 Hours

The following sections describe each Phase of testing and provide a high-level overview of data. Note that in each Phase when the primary THETA vessel band heaters were set to 'ON' it is a manual duty cycle for each of the 4 band heater zones that was determined to produce a quasi-adiabatic condition throughout testing, where the heat lost through the thermal insulation was balanced by heating. This was determined by setting the primary pump to a speed >= 1 GPM and determining a steady state heater set point that maintained a constant sodium temperature as a function of time +/- ~2°C. Note also that each vessel heater zone power meter data was continuously recorded throughout testing to facilitate the calculation of a boundary condition on the vessel.

Note that Appendix B provides the identification numbers for all of the 100 tests performed.

4.1.1. Phase 1: Thermal Stratification at Nominal Conditions

Phase 1 testing was performed to characterize hot and cold pool thermal stratification at various operating conditions. *Table 4* provides the values of vessel band heater power setting, IHX outlet window, primary pump flowrate and core power that were set to complete a parametric study to thoroughly characterize the stratification of THETA. Note that throughout this testing the secondary system was not online and the core barrel and IHX outlet barrel were not insulated.

Figure 55 provides typical core power and flowmeter data for one of the 24 total tests performed for Phase 1. As can be seen the core power was set to 0 kW for the first minute of the test in order to collect steady state pool temperature data. From minute 1 to 31 the core power was turned on to a nominal 37.6 kWe before being set to 0 kW for the remainder of the test.

In order to demonstrate the repeatability of the testing between Sets, Figure 56 provides hot and cold pool data for a sample of the same Item A (vessel heaters off), Test 1 for each Set. As can be seen the temperature data shows good test repeatability even though they were performed 6 months apart. All testing in Phase 1 shows high repeatability between Sets.

Figure 57 provides the thermocouple temperature data at position A for all flowrates and IHX outlet window elevations to visually demonstrate the effect these variables have on stratification. As can be seen, the lower Richardson number conditions with a high primary pump flow rate results in less stratification in both the hot and cold pool. The bottom IHX window open condition results in less thermal stratification in the cold pool, especially at a nominal primary pump flow rate of 12.5 GPM.

Table 4: Phase 1, Thermal Stratification at Nominal Conditions

Item	Test Number	IHX Outlet Elevation	Primary Pump Flow Rate [GPM]	Core Power [kWe]
Item A / Item B (vessel process heat OFF/ON)	1	Top	12.5	37.6
	2	Top	8.64	37.6
	3	Top	1	37.6
	4	Bottom	12.5	37.6
	5	Bottom	8.64	37.6
	6	Bottom	1	37.6

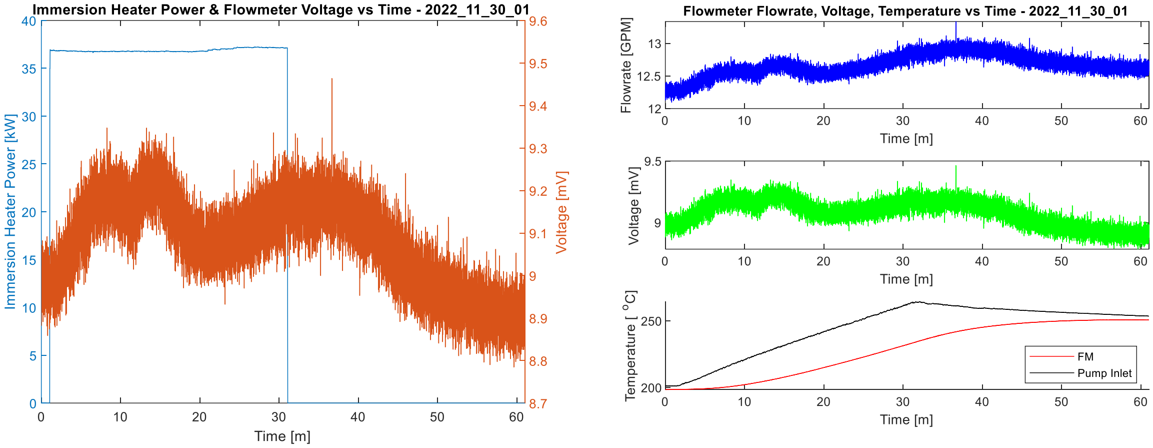

Figure 55: Data from Phase 1, Set 2, Item A, Test 1. Core (immersion heater) power and flowmeter voltage plotted versus time on left showing general characteristics for all Phase 1 testing. Flowmeter flowrate, measured voltage and temperature at flowmeter magnets and pump inlet plotted as a function of time on right.

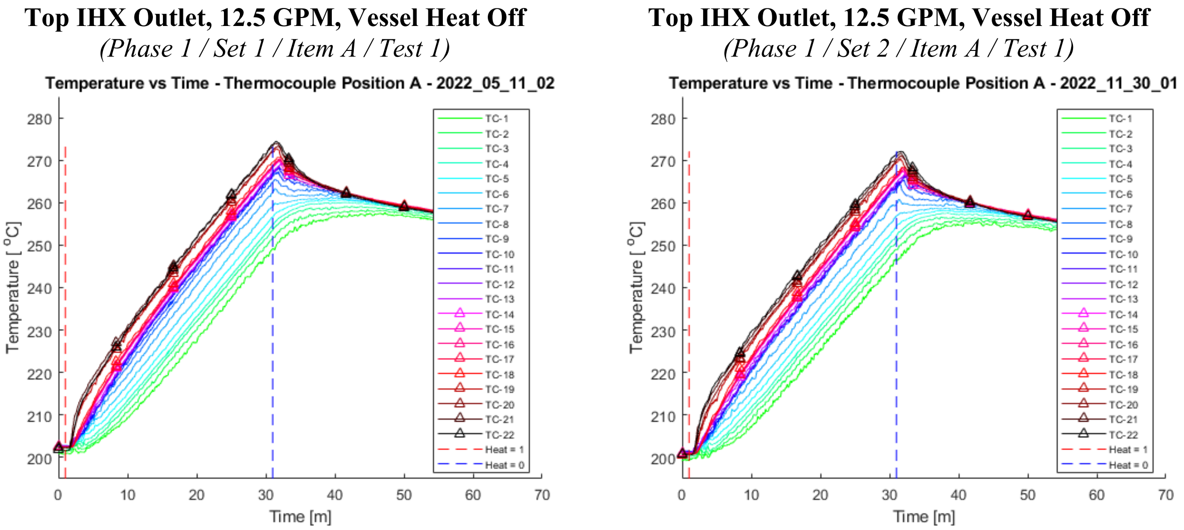
Top IHX Outlet, 12.5 GPM, Vessel Heat Off
(Phase 1 / Set 1 / Item A / Test 1)

Top IHX Outlet, 12.5 GPM, Vessel Heat Off
(Phase 1 / Set 2 / Item A / Test 1)

Figure 56: Comparing temperature data from the thermocouple at position A. Set 1 and Set 2 for Phase 1, Item A, Test 1. Marked with a red and blue dotted lines are the start and stop of core power at 37.6 kWe, respectively

Top IHX Outlet, 12.5 GPM, Vessel Heat Off
(Phase 1 / Set 2 / Item A / Test 1)

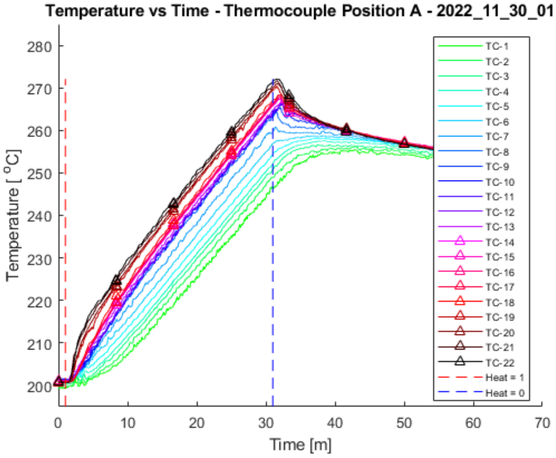

Top IHX Outlet, 8.6 GPM, Vessel Heat Off
(Phase 1 / Set 2 / Item A / Test 2)

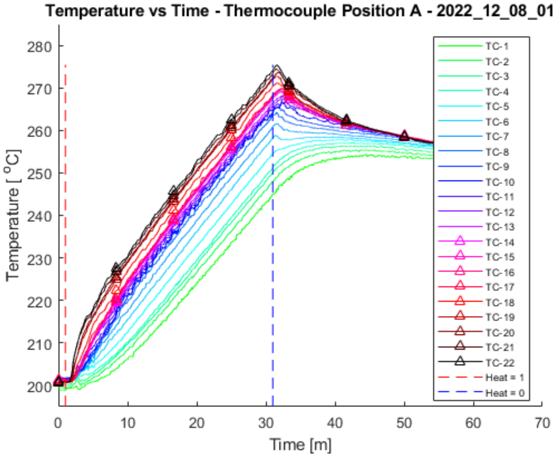

Top IHX Outlet, 1 GPM, Vessel Heat Off
(Phase 1 / Set 2 / Item A / Test 3)

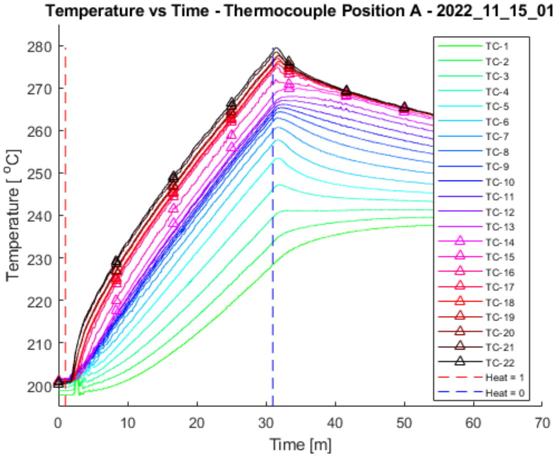

Bottom IHX Outlet, 12.5 GPM, Vessel Heat Off
(Phase 1 / Set 2 / Item A / Test 4)

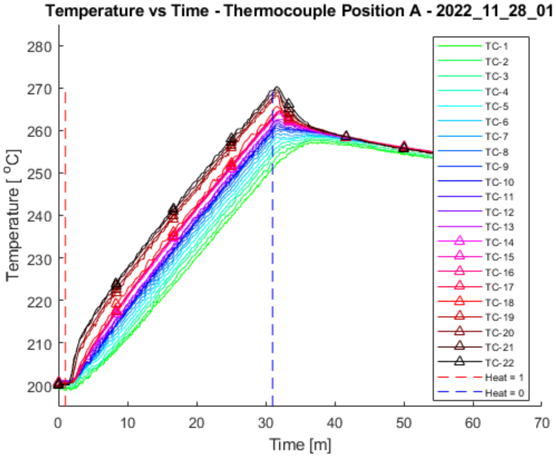

Bottom IHX Outlet, 8.6 GPM, Vessel Heat Off
(Phase 1 / Set 2 / Item A / Test 5)

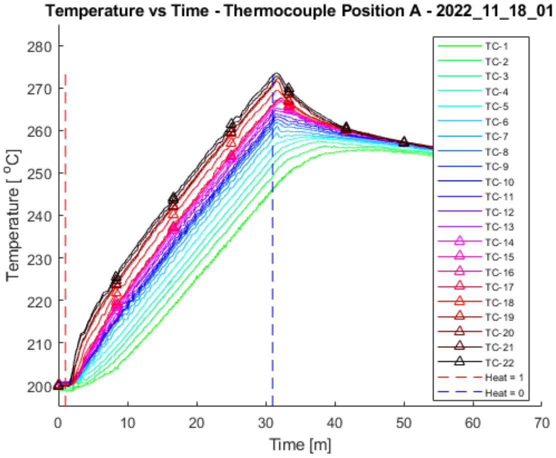

Bottom IHX Outlet, 1 GPM, Vessel Heat Off
(Phase 1 / Set 2 / Item A / Test 6)

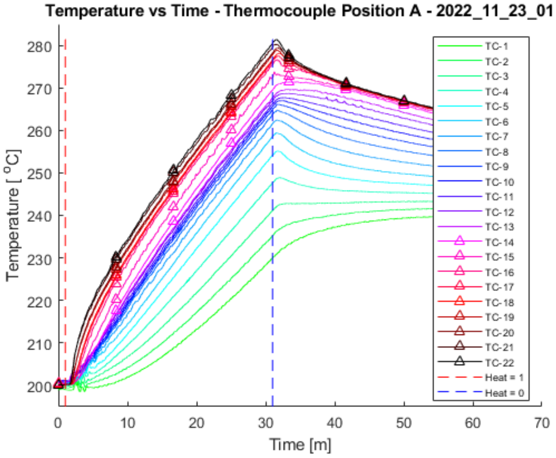

Figure 57: Phase 1, Set 2, Item A, Test 1-6 thermocouple position A temperature vs time. Marked with a red and blue dotted lines are the start and stop of core power at 37.6 kWe, respectively. In the left column the top IHX outlet window is open, in the right column the bottom IHX outlet window is open.

In order to compare Items A and B (vessel heat off / on, respectively) Figure 58 provides the position A thermocouple temperatures as a function of time for Items A and B, tests 1 and 3. As can be seen there is a high degree of correlation on the shape and magnitude of thermal stratification developed between Items A and B. The vessel heater power has a marginal effect on the maximum temperature reached in the hot pool and cold pools while the core power is on. However, the hot and cool pool temperatures drop at a noticeably faster rate with the vessel heat off after the core power is turned off at ~30+ minutes.

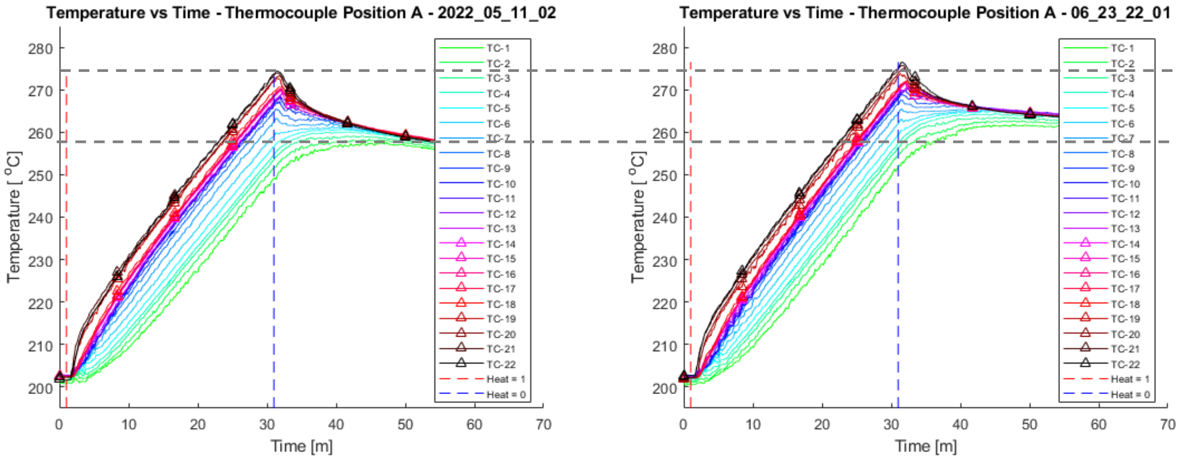

Top IHX Outlet, 12.5 GPM, Vessel Heat Off
(Phase 1 / Set 1 / Item A / Test 1)

Top IHX Outlet, 12.5 GPM, Vessel Heat On
(Phase 1 / Set 1 / Item B / Test 1)

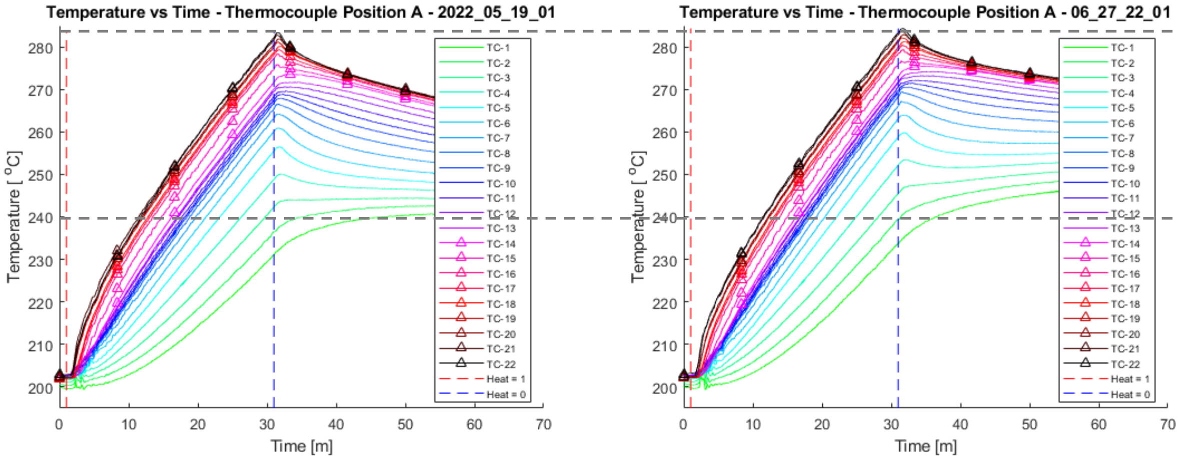

Top IHX Outlet, 1 GPM, Vessel Heat Off
(Phase 1 / Set 1 / Item A / Test 3)

Top IHX Outlet, 1 GPM, Vessel Heat On
(Phase 1 / Set 1 / Item B / Test 3)

Figure 58: Comparing thermocouple pool temperatures between Items A (vessel heaters off) and Items B (vessel heaters constant 'adiabatic' duty cycle) for Test 1 (12.5 GPM primary pump) and Test 3 (1 GPM). All tests were part of Set 1

4.1.2. Phase 1.5: Characterization of Core Wall Insulation

Following the Phase 1 testing it was determined that a significant amount of heat from the core was being conducted through the core barrel wall directly into the cold pool. Estimates from CFD analyses determined over half of the heat was being lost to the cold pool during certain operations [10]. It was also determined that the IHX outlet barrel was conducting a significant amount of thermal energy from the sodium inside the barrel, reducing the effect of different outlet elevations on the stratification of the cold pool. In order to reduce the thermal conductivity in these two features an Inconel sheet metal structure was constructed to trap a volume of inert gas to create a thermal blanket; [2] describes the calculated effectiveness and installation of these insulators.

Phase 1.5 testing was meant to experimentally characterize the performance of the system with the core barrel and IHX outlet insulators installed. *Table 5* provides the parameters tested during this Phase. The core power was actuated on and off at identical times as in Phase 1. Notice that the three tests in Phase 1.5 are a repeat of Tests 1, 4 and 6 from Phase 1, Table 4.

Figure 59 provides a comparison of Phase 1 and Phase 1.5 test data where the thermocouple temperatures at position A have been plotted as a function of time for select tests with identical system settings between the two Phases. Notice the top two plots in Figure 59 compare uninsulated vs insulated components for a flowrate of 12.5 GPM and the top IHX outlet window open. The cold pool thermal stratification is markedly higher, and the maximum temperature reached in the hot and cold pool is greater in the system with insulated core barrel and IHX outlet. Similarly in the bottom two plots of Figure 59 the position A thermocouple temperatures have been plotted to compare the un-insulated and insulated system condition for a primary pump flowrate of 12.5 and the bottom IHX outlet window open. Notice the enhanced cold pool thermal stratification and the increased maximum temperature of the hot and cold pools for Phase 1.5 (insulated) as compared to Phase 1 (uninsulated) testing.

*Table 5: Phase 1.5, Characterization of Core Wall Insulation. *Note that identical primary pump settings were used for Phase 1 and 1.5 to achieve a flowrate of 12.5 GPM, however a flowrate of less than 12.5 was measured by the permanent magnet flowmeter after reinstalling the primary system for Phase 1.5 testing. This was due to poor sodium wetting on the flowmeter wall which disappeared during Phase 2+ testing due to prolonged exposure of the inner pipe wall to sodium to facilitate full wetting.*

Item	Test Number	IHX Outlet Elevation	Primary Pump Flow Rate [GPM]	Core Power [kWe]
Item A (band heaters OFF)	1	Top	12.5*	37.6
	2	Bottom	12.5*	37.6
	3	Bottom	1	37.6
Item B (band heaters ON)	1	Bottom	12.5*	37.6
	2	Top	12.5*	37.6
	3	Bottom	1	37.6

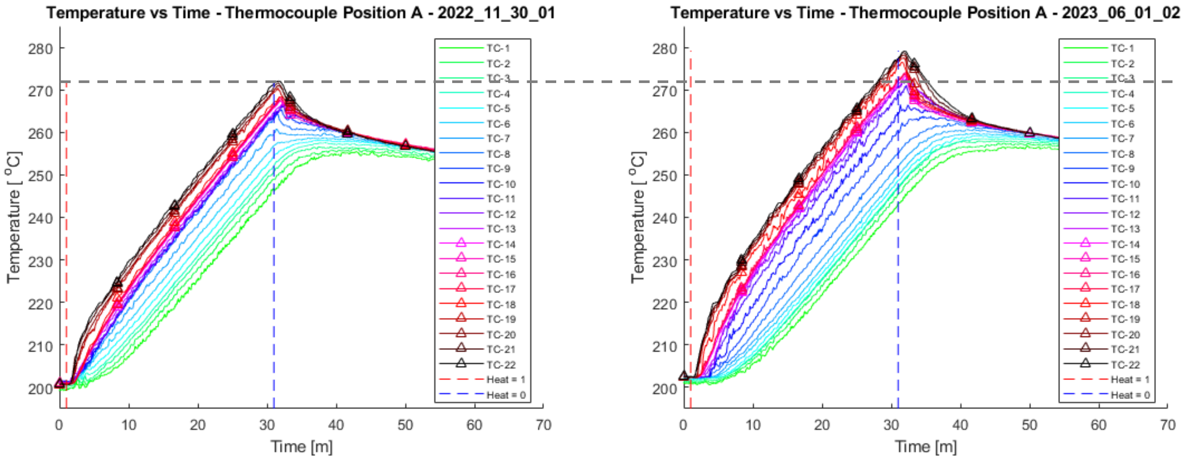

No Insulation, Top IHX Outlet, 12.5 GPM
(Phase 1 / Set 2 / Item A / Test 1)

Insulation, Top IHX Outlet, 12.5 GPM
(Phase 1.5 / Set 2 / Item A / Test 1)

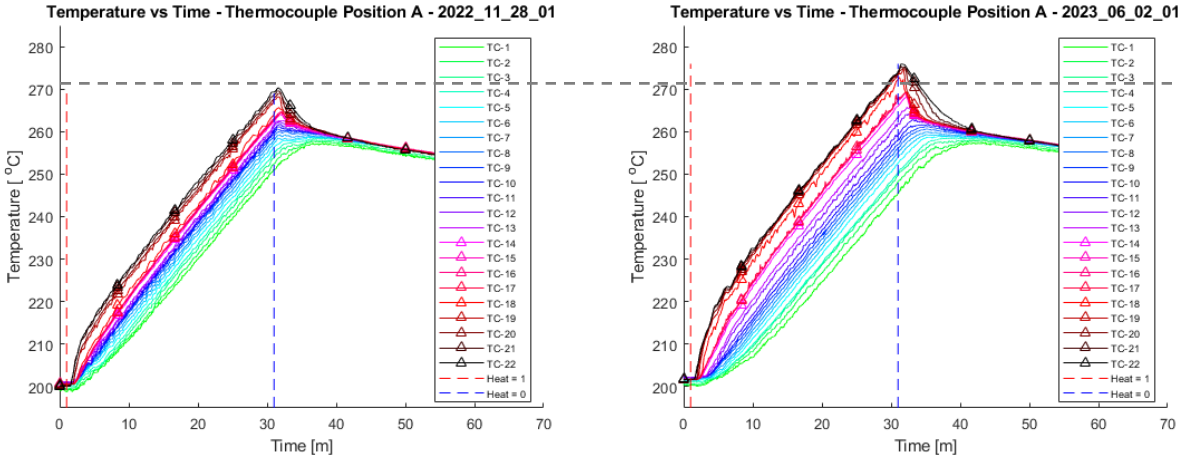

No Insulation, Bottom IHX Outlet, 12.5 GPM
(Phase 1 / Set 2 / Item A / Test 4)

Insulation, Bottom IHX Outlet, 12.5 GPM
(Phase 1.5 / Set 2 / Item A / Test 2)

Figure 59: Top: non-insulated vs insulated system components for a flowrate of 12.5 GPM with top IHX window open. Bottom: non-insulated vs insulated system components for a flowrate of 12.5 GPM with the bottom IHX window open.

Figure 60 provides a comparison of the hot and cold pool temperature for the un-insulated vs the insulated core barrel and IHX outlet barrel. Both tests were run with a primary pump measured flowrate of 1 GPM (same pump shaft speed) and the bottom IHX outlet window open. As can be seen the maximum temperatures at each location on the position A thermocouple rake and the overall thermal stratification in the hot and cold pool are significantly greater with the insulated system components. Also notice the bottom most TC (TC-1) in the cold pool shows a marked reduction in minimum temperature in the insulated condition.

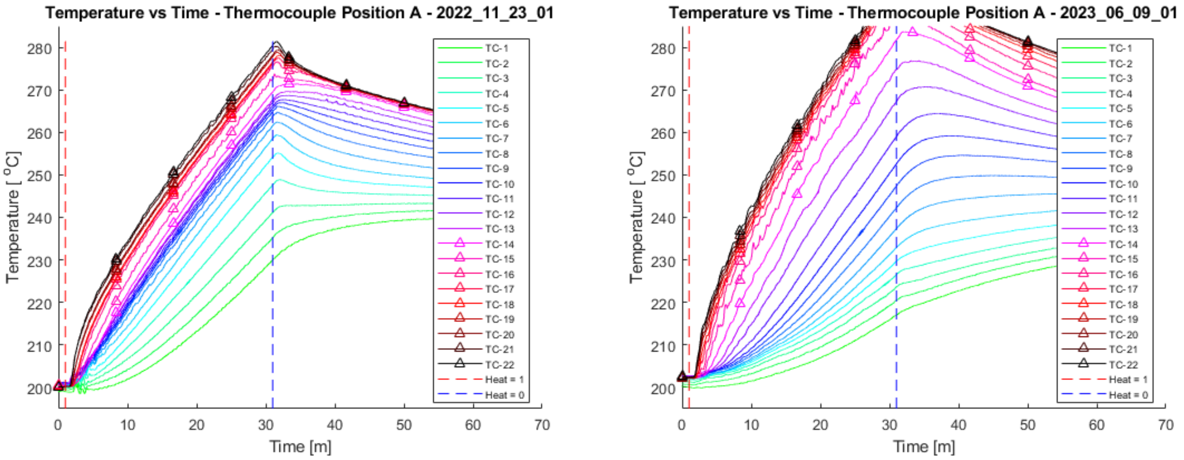

No Insulation, Bottom IHX Outlet, 1 GPM
(Phase 1 / Set 2 / Item A / Test 6)

Insulation, Bottom IHX Outlet, 1 GPM
(Phase 1.5 / Set 2 / Item A / Test 3)

Figure 60: Position A thermocouple temperature as a function of time for the non-insulated (left) and insulated (right) system conditions with a primary system flowrate of 1 GPM through the core barrel and the bottom IHX window open.

4.1.3. Phase 2: Secondary System Characterization

Phase 2 was performed to characterize the steady state THETA performance with the secondary system installed at two baseline operating conditions determine through a scaling analysis [11]. The tests aimed to match a modified Froude number while also maintaining similar flow regimes and dominant heat transfer processes, ensuring the Reynolds, Grashof, Peclet, and Rayleigh numbers were above certain thresholds. The testing conditions are provided in Table 6.

Tests 1 and 2 were performed to identify the sodium-to-air heat exchanger (AHX) blower speed and secondary pump speed required to achieve steady state with a primary pump flowrate of 3.6 and 6.3 GPM, respectively, and a core power of 32.7 kWe with the top IHX outlet window opened. Once the secondary system steady state parameters were determined with Tests 1 and 2, Tests 3 and 4 were performed to assess the time response of the secondary system by turning on the primary and secondary system components at steady state set points from a steady state isothermal start condition where the primary pump was running at the specified flowrate in Table 6 for a period of 60 seconds into each test before triggering the core and secondary system on. Tests 3 and 4 were performed twice to ensure repeatability, defined as Sets 1 and 2. The tests in Phase 2 were terminated when the system had reached a steady state condition for a period of 10 minutes. During this testing the vessel process heaters were set to a constant duty cycle to achieve a quasi-adiabatic condition with power meter data recording each heater zone energy.

Table 6: Phase 2, Secondary System Characterization

Category	Test Number	IHX Outlet Elevation	Primary Pump Flow Rate [GPM]	Core Power [kWe]
Secondary system characterization	1	Top	3.6 (high Fr)	32.7
	2	Top	6.3 (low Fr)	32.7
Secondary system time delay	3	Top	6.3 (low Fr)	32.7
	4	Top	3.6 (high Fr)	32.7

Figure 61 provides the thermocouple rake at position A temperature as a function of time for Sets 1 and 2 for Tests 3 and 4. The time constant can be used to measure the response time of a system to a step input, defined as when the system reaches 63.2% of its final value. In

Table *7* the time constant of the cold pool for Tests 3 and 4, as measured with TC-1 and TC-12 at thermocouple rake position A, was provided as well as the time constant for the hot pool as measured with TC-14 and TC-22. As can be seen the top of the hot pool, TC-22, possesses the shortest time constant likely due to the lack of a significant upper internal structure above the core facilitating the plume from above the core to readily inject hot sodium to the top of the hot pool to allow this volume to come to steady state quickly. In every region of the hot and cold pool the higher Froude number condition (Test 4, 3.6 GPM) possessed longer time constants as compared to the lower Froude number condition (Test 3, 6.3 GPM), as one would expect.

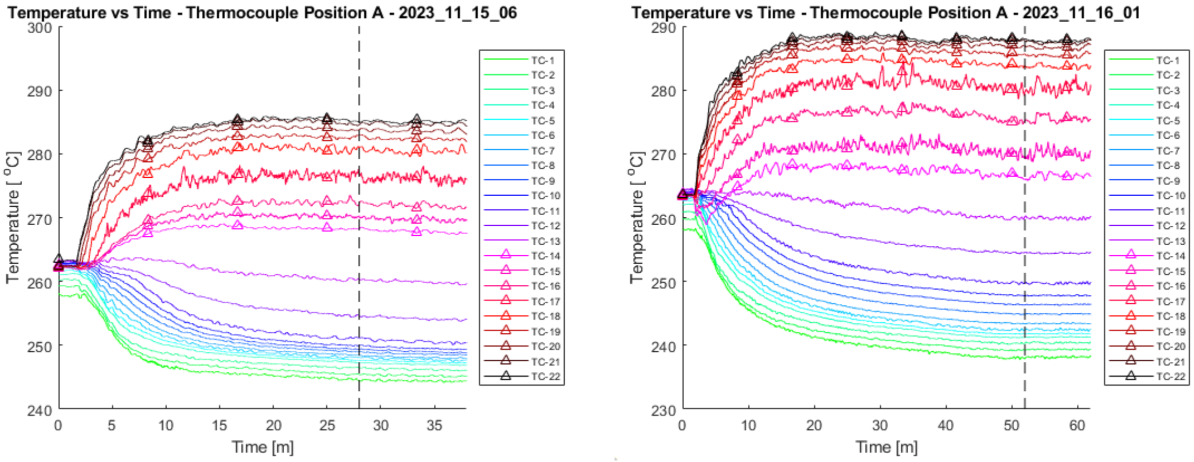
Primary Pump 6.3 GPM
(Phase 2 / Set 1 / Test 3)

Primary Pump 3.6 GPM
(Phase 2 / Set 1 / Test 4)

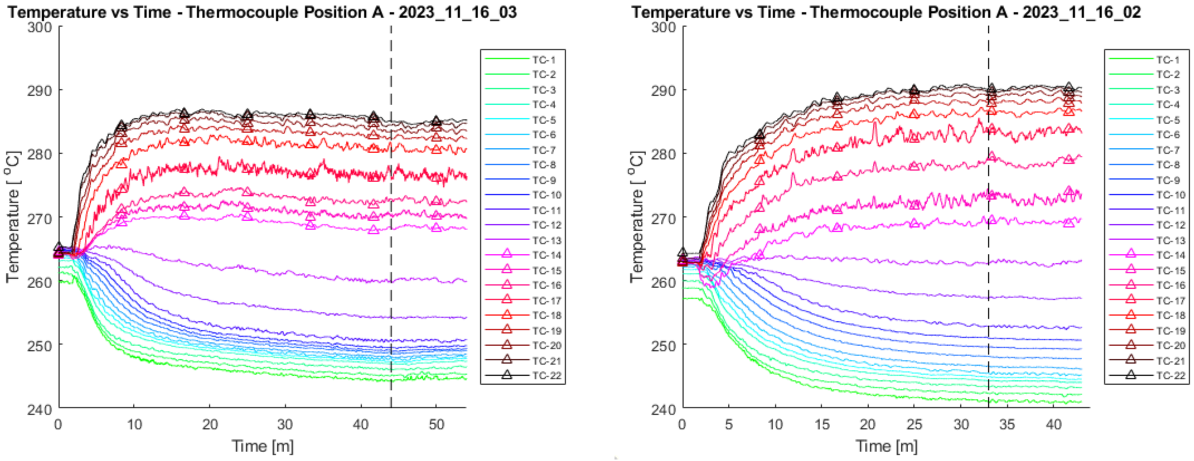
Primary Pump 6.3 GPM
(Phase 2 / Set 2 / Test 3)

Primary Pump 3.6 GPM
(Phase 2 / Set 2 / Test 4)

Figure 61: Thermocouple at position A temperature as a function of time for Phase 2, Set 1 and 2, Tests 3 and 4. Highlighted with a vertical dotted line is where the system operator determined steady state was reached at which point the system was run for a period of 10 minutes before terminating the test.

Table 7: Time constant of thermocouple junctions rounded to nearest second. Initial 60 second isothermal state from each test subtracted from time constant.

Test	Set	Position A Measured Time Constant [sec]			
		TC-1	**TC-12**	**TC-14**	**TC-22**
3	1	331	813	274	188
	2	352	847	236	172
4	1	568	1123	521	233
	2	431	890	653	293

4.1.4. Phase 3: Natural Circulation Startup Flow Conditions

Phase 3 investigated the timescales required to establish natural circulation flow, stratification rates, and the nonlinear transition from a stagnant flow condition. Ten unique tests were performed in two Sets for a total of 20 tests for Phase 3. The testing conditions for this Phase have been provided in *Table 8*.

During this testing the vessel process heaters were set to a constant duty cycle to achieve a quasi-adiabatic condition with power meter data recording each heater zone energy. For Tests 1-8 the system was initiated with a steady state isothermal condition at the specified pump speed (380 RPM for 3.6 GPM and 580 RPM for 6.3 GPM), the final 60 seconds of this steady state isothermal condition was recorded for each test. The pump was then shut off for a period of 30 seconds to create an isothermal, stagnant condition.

For tests 1, 3, 5, and 7 the core power was then set to 32.7 kWe and the primary pump was set to the specified flowrate as defined in *Table 8*. Test 1, 3, 5, and 7 was terminated after about 13.5 minutes to keep the primary system maximum temperature below 300 °C (temperature limit of the polyimide coated optical fibers). Figure 62 provides measured core power and primary system flowrate as a function of time for Test 1 (Set 2), where the initial stagnant condition is seen from 60-90 seconds followed by the step to a primary system flowrate of approximately 3.6 GPM and a core power of 32.7 kWe. The position A thermocouple rake temperature as a function of time was plotted for Tests 1, 3, 5, and 7 in Figure 63. The primary pump speed and IHX outlet window does not seem to have a discernable effect on the temperature profiles in Figure 63.

Table 8: Phase 3, Natural Circulation Startup Flow Conditions

Test No.	IHX Outlet Elevation	Primary Pump Flow Rate [GPM]	Core Power [kWe]	Secondary System Operation
1	Top	Step 0 → 3.6	Step 0 → 32.7	IHX flow off, AHX blower off
2	Top	Step 0 → 3.6	Step 0 → 32.7	Step to known steady state configuration (Phase 2, Test 1,4)
3	Bottom	Step 0 → 3.6	Step 0 → 32.7	IHX flow off, AHX blower off
4	Bottom	Step 0 → 3.6	Step 0 → 32.7	Step to known steady state configuration (Phase 2, Test 1,4)
5	Top	Step 0 → 6.3	Step 0 → 32.7	IHX flow off, AHX blower off
6	Top	Step 0 → 6.3	Step 0 → 32.7	Step to known steady state configuration (Phase 2, Test 2,3)
7	Bottom	Step 0 → 6.3	Step 0 → 32.7	IHX flow off, AHX blower off
8	Bottom	Step 0 → 6.3	Step 0 → 32.7	Step to known steady state configuration (Phase 2, Test 2,3)
9	Top	Pump Off	Step 0 → 32.7	Step to known steady state configuration (Phase 2, Test 1,4)
10	Bottom	Pump Off	Step 0 → 32.7	Step to known steady state configuration (Phase 2, Test 1,4)

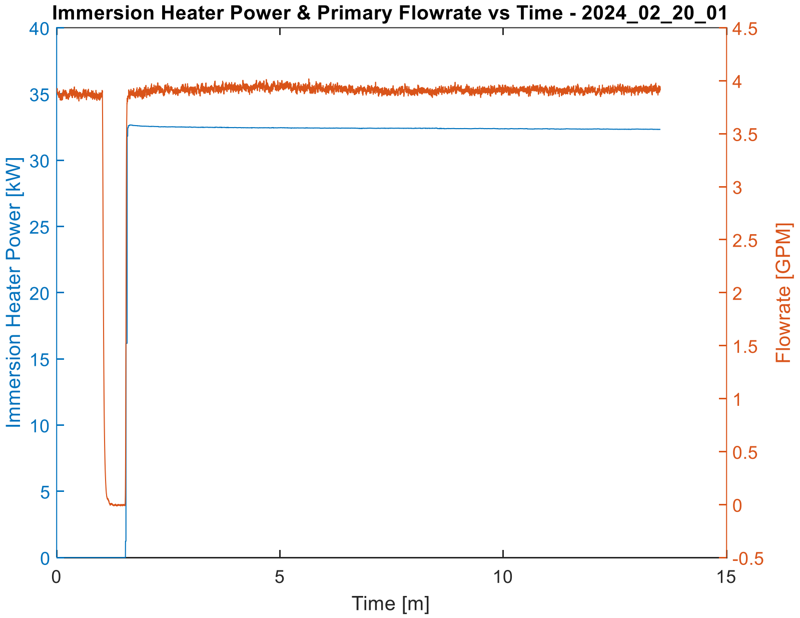

Figure 62: Phase 3, Set 2, Test 1, immersion heater power (blue) and primary pump flowrate (orange) as a function of time.

Primary Pump 3.6 GPM, Top IHX Outlet
(Phase 3 / Set 2 / Test 1)

Primary Pump 3.6 GPM, Bottom IHX Outlet
(Phase 3 / Set 2 / Test 3)

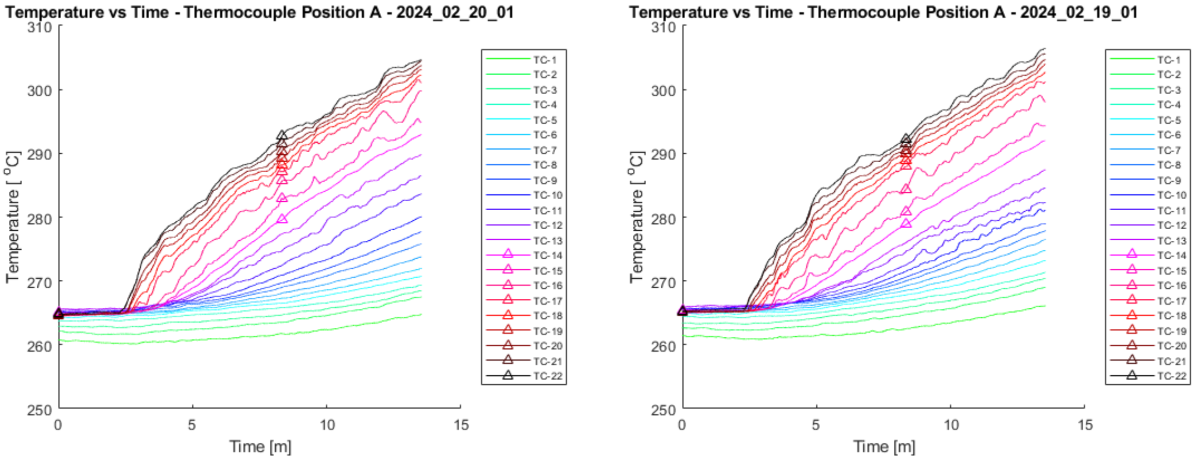

Primary Pump 6.3 GPM, Top IHX Outlet
(Phase 3 / Set 2 / Test 5)

Primary Pump 6.3 GPM, Bottom IHX Outlet
(Phase 3 / Set 2 / Test 7)

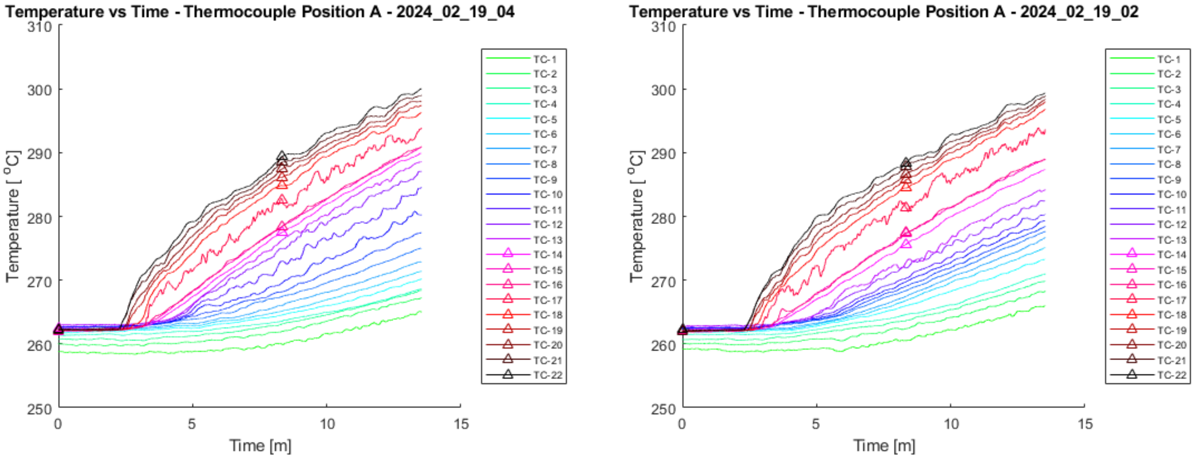

Figure 63: Thermocouple position A temperature as a function of time for Tests 1, 3, 5, 7 (Set 2)

For Tests 2, 4, 6, and 8 the secondary system was first activated by setting a known steady state condition determined in Phase 2 for the low Froude number (6.3 GPM primary flow) and high Froude number (3.6 GPM primary flow) states. The secondary system was allowed to operate for a period of 3 minutes before triggering a step increase in the primary pump and core to the parameters provided in *Table 8*. The secondary system AHX blower motor speed and secondary flowmeter voltage were plotted as a function of time for Test 2, Set 2 in *Figure 64*. The primary system core and flowmeter measured flowrate were also plotted as a function of time for Test 2, Set 2 in *Figure 65*. The position A thermocouple temperature was plotted as a function of time for Tests 2, 4, 6 and 8 (Set 2) in Figure 66. As can be seen there is an initial dip in the hot pool temperatures during the 3 minutes the secondary system is operating without the core power or primary pump activated. The initial 15 minutes of Test 4 (3.6 GPM primary pump) and Test 8 (6.3

GPM primary pump) were plotted in Figure 67. As can be seen the bottom hot pool temperatures (TC14-15) rise more rapidly at the lower Froude number condition (6.3 GPM).

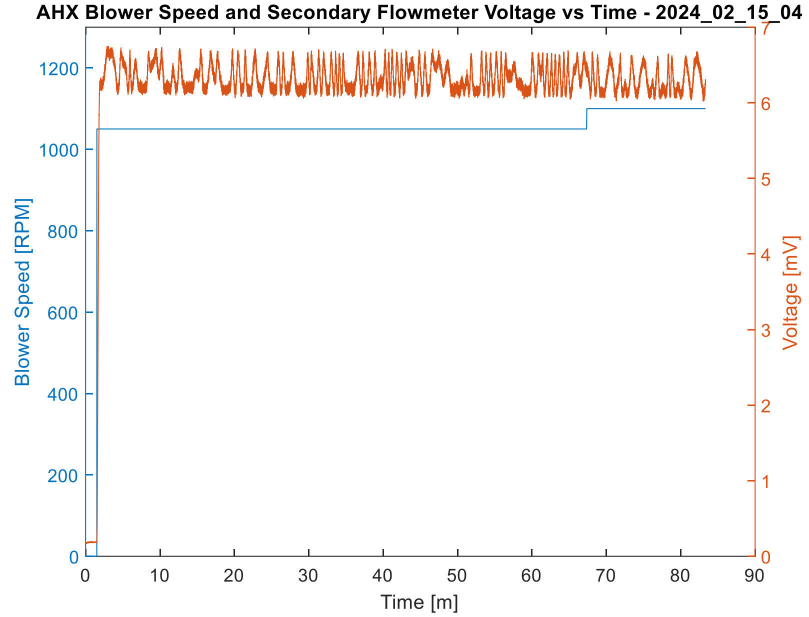

Figure 64: Phase 3, Set 2, Test 2 AHX blower motor speed and measured flowmeter voltage as a function of time

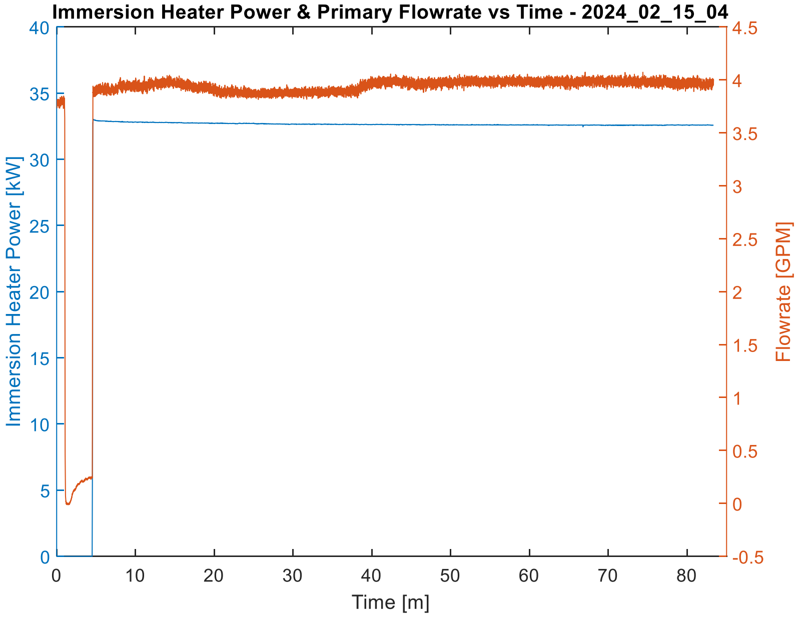

Figure 65: Phase 3, Set 2, Test 2 measured core power and primary flowrate as a function of time

Primary Pump 3.6 GPM, Top IHX Outlet *(Phase 3 / Set 2 / Test 2)*

Primary Pump 3.6 GPM, Bottom IHX Outlet *(Phase 3 / Set 2 / Test 4)*

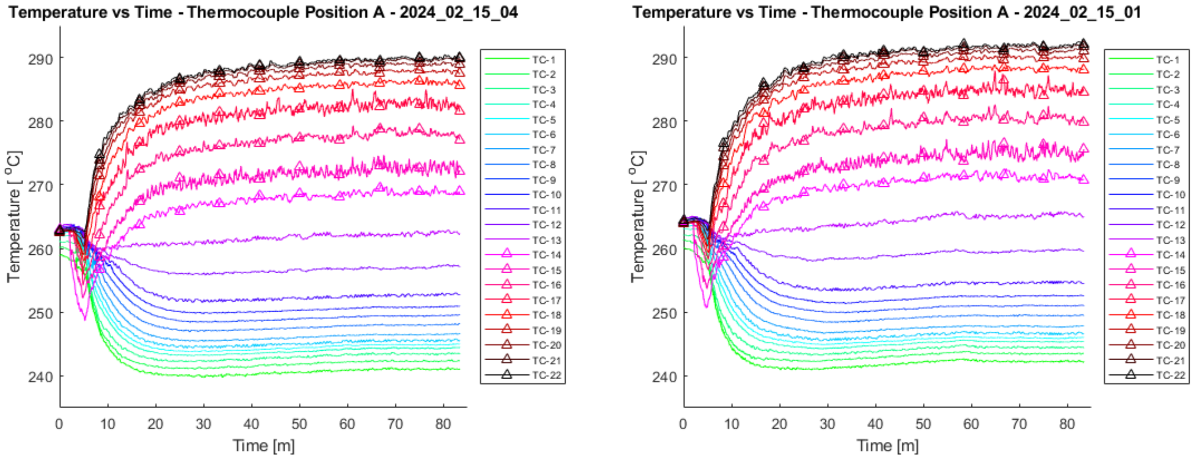

Primary Pump 6.3 GPM, Top IHX Outlet *(Phase 3 / Set 2 / Test 6)*

Primary Pump 6.3 GPM, Bottom IHX Outlet *(Phase 3 / Set 2 / Test 8)*

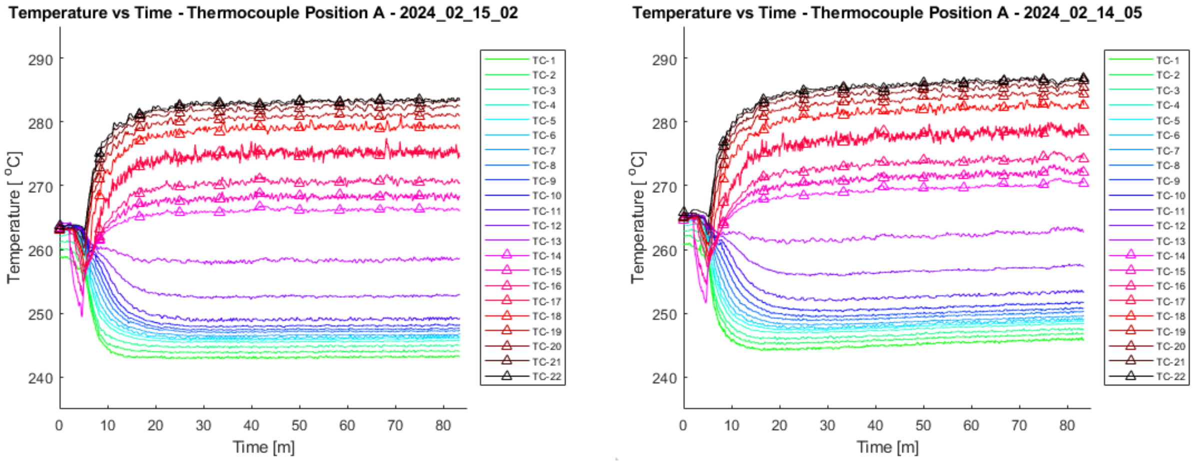

Figure 66: Thermocouple position A temperature as a function of time for Tests 2, 4, 6, 8 (Set 2)

Primary Pump 3.6 GPM, Bottom IHX Outlet *(Phase 3 / Set 2 / Test 4)*

Primary Pump 6.3 GPM, Bottom IHX Outlet *(Phase 3 / Set 2 / Test 8)*

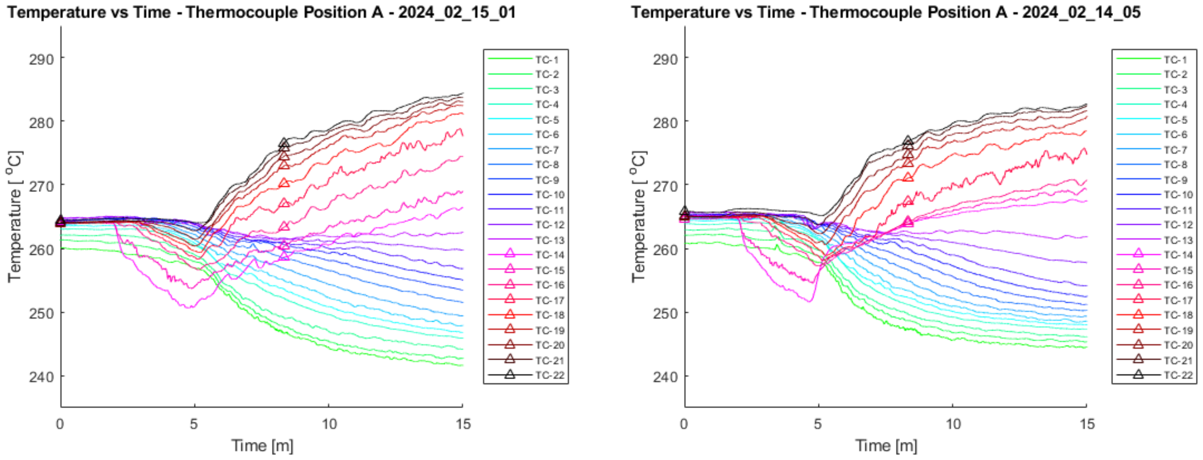

Figure 67: Thermocouple position A temperature as a function of time for first 15 minutes of Tests 4 and 8 (Set 2)

Figure 68 provides an overview of Test 9 and 10 data. The location of the IHX outlet does not appear to have a large effect on the development of natural circulation or temperature distribution in the primary system. A small increase in natural circulation flow as measured by the primary flowmeter was apparent in the bottom IHX outlet opening test (Test 10) as compared to Test 9.

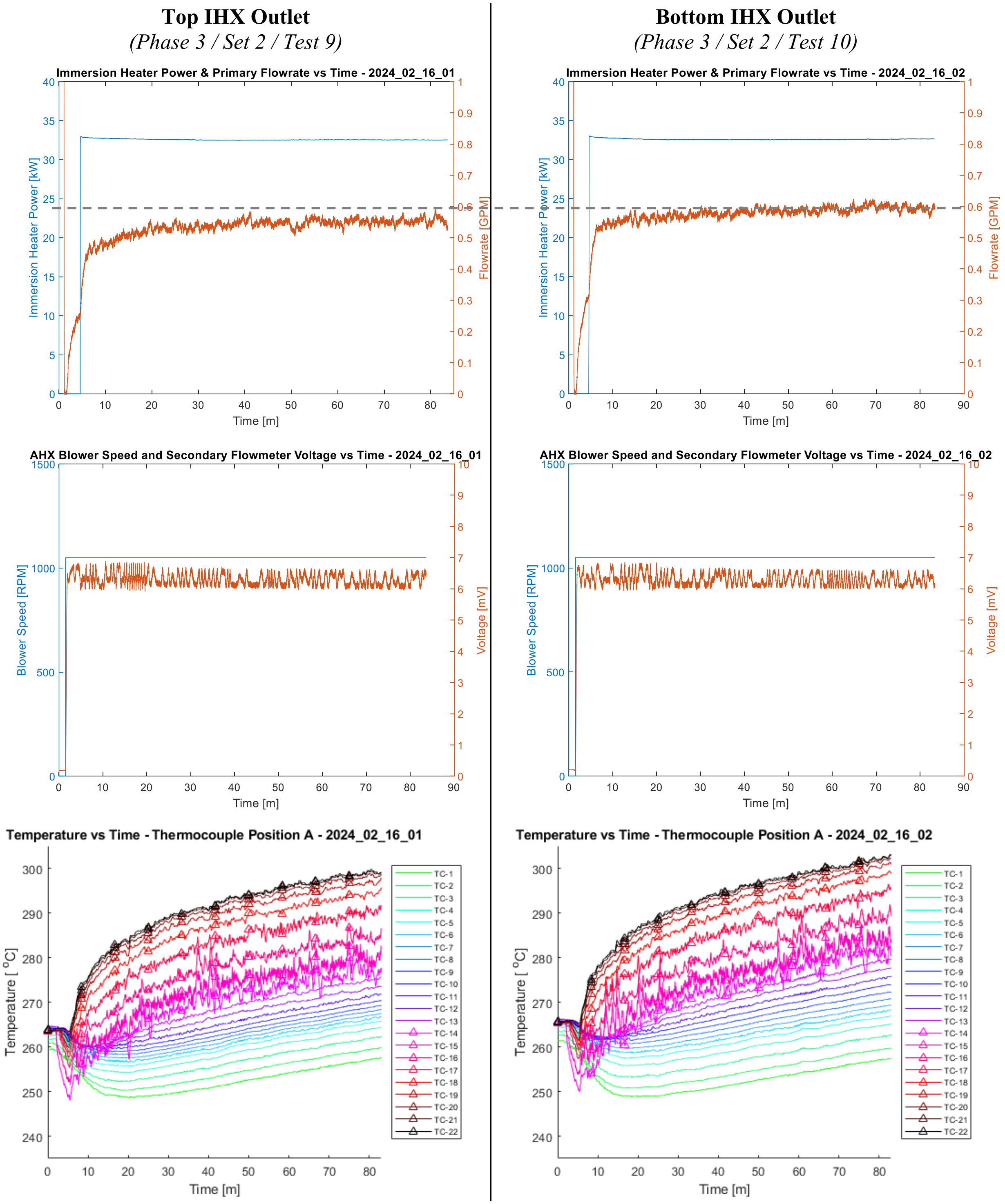

Figure 68: Comparing Test 9 (left) with Test 10 (right) immersion heater power and primary flowrate vs time (top). AHX blower speed and secondary flowmeter voltage vs time (middle). Thermocouple position A temperature vs time (bottom).

4.1.5. Phase 4: Power Level Transient Flow Behavior

Phase 4 testing investigated the thermal hydraulic response to a step change in the core heat power. The reason for this test was to simulate the flow behavior that can occur during an event where core power changes quickly (overpower or underpower). The parameters for the two Sets of 12 Tests that were completed for this Phase are included in Table 9. Note that the starting condition for all of the tests was steady state with secondary system activated as defined in Phase 2 for a primary pump flowrate of ~3.6 and ~6.3 GPM.

For Test 1, 3, 5, and 7 the core power was reduced 10% after 30 seconds of steady state from 32.7 to 29.5 kWe. The IHX outlet set point is provided for these tests in Table 9. For Test 2, 4, 6, and 8 the core power was increased 10% from 32.7 to 36.0 kWe. The secondary system steady state parameters were unchanged during Test 1-8.

For Tests 9 and 11 the primary system conditions were not changed from the initial steady state and the secondary system heat removal was increased by 10% after 30 seconds of steady state. Similarly for Tests 10 and 12 the primary system conditions were not changed from the initial steady state and the secondary system heat removal was decreased by 10% after 30 seconds of steady state.

Figure 69 provides a figure of the core power being reduced at 30 seconds for Test 1 (Set 2). The position A thermocouple temperature was plotted in Figure 70 as a function of time for Tests 1, 3, 5, and 7 (all Tests part of Set 2). As can be seen the higher thermal stratification in the lower flow tests (Test 1, 3) is maintained in the hot and cold pools throughout the 60-minute test after the core power is reduced as compared to the higher flow test (Test 5, 7). The IHX outlet position does not have a significant effect on the thermal stratification.

Figure 71 Provides the position A thermocouple temperature for Test 2, 4, 6 and 8 where the core power was increased by 10% after an initial steady state with secondary system operating. The higher thermal stratification in the hot and cold pool was maintained for the lower flowrate Tests 2 and 4 as compared to the higher flowrate Tests 6 and 8. The IHX outlet position does not have a significant effect on the thermal stratification.

Table 9: Phase 4, Power Level Transient Flow Behavior

Test Number	IHX Outlet Elevation	Initial Condition	Core Power [kWe]	Secondary System Operation
1	Top	Phase 2, Test No. 1 (3.6 GPM)	32.7 → 29.5 (-10%)	No change
2	Top	Phase 2, Test No. 1 (3.6 GPM)	32.7 → 36.0 (+10%)	No change
3	Bottom	Phase 2, Test No. 1 (3.6 GPM)	32.7 → 29.5 (-10%)	No change
4	Bottom	Phase 2, Test No. 1 (3.6 GPM)	32.7 → 36.0 (+10%)	No change
5	Top	Phase 2, Test No. 2 (6.3 GPM)	32.7 → 29.5 (-10%)	No change
6	Top	Phase 2, Test No. 2 (6.3 GPM)	32.7 → 36.0 (+10%)	No change
7	Bottom	Phase 2, Test No. 2 (6.3 GPM)	32.7 → 29.5 (-10%)	No change
8	Bottom	Phase 2, Test No. 2 (6.3 GPM)	32.7 → 36.0 (+10%)	No change
9	Top	Phase 2, Test No. 2 (6.3 GPM)	32.7	+10% secondary heat removal
10	Top	Phase 2, Test No. 2 (6.3 GPM)	32.7	-10% secondary heat removal
11	Bottom	Phase 2, Test No. 2 (6.3 GPM)	32.7	+10% secondary heat removal
12	Bottom	Phase 2, Test No. 2 (6.3 GPM)	32.7	-10% secondary heat removal

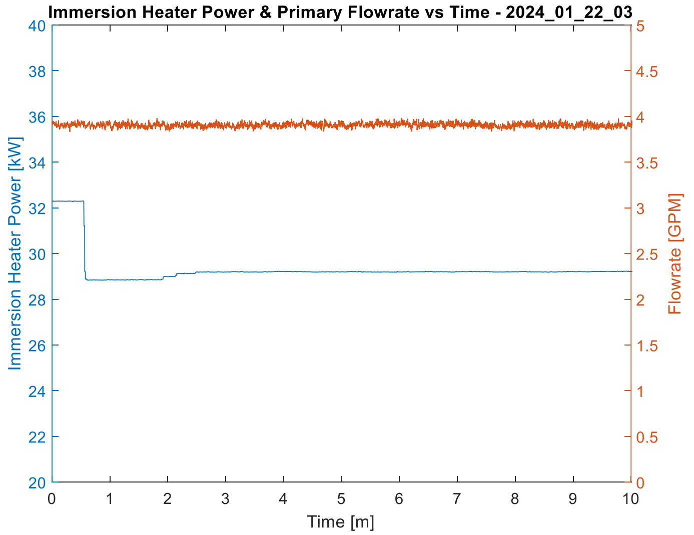

Figure 69: Phase 4, Set 2, Test 1, core power and primary flowrate vs time

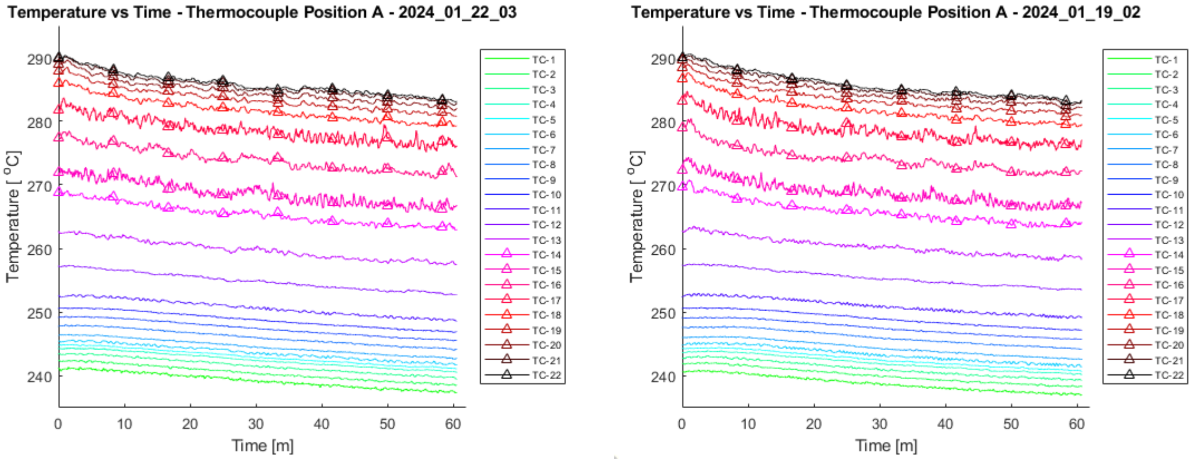

Primary Pump 3.6 GPM, Top IHX Outlet
(Phase 4 / Set 2 / Test 1)

Primary Pump 3.6 GPM, Bottom IHX Outlet
(Phase 4 / Set 2 / Test 3)

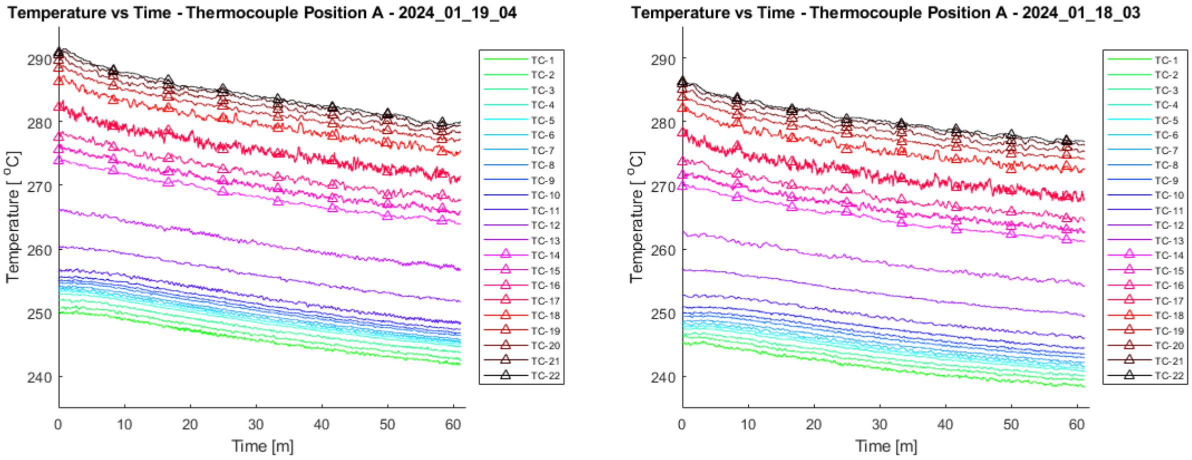

Primary Pump 6.3 GPM, Top IHX Outlet
(Phase 4 / Set 2 / Test 5)

Primary Pump 6.3 GPM, Bottom IHX Outlet
(Phase 4 / Set 2 / Test 7)

Figure 70: Position A thermocouple temperature as a function of time for Set 2, Tests 1, 3, 5, and 7

Primary Pump 3.6 GPM, Top IHX Outlet
(Phase 4 / Set 2 / Test 2)

Primary Pump 3.6 GPM, Bottom IHX Outlet
(Phase 4 / Set 2 / Test 4)

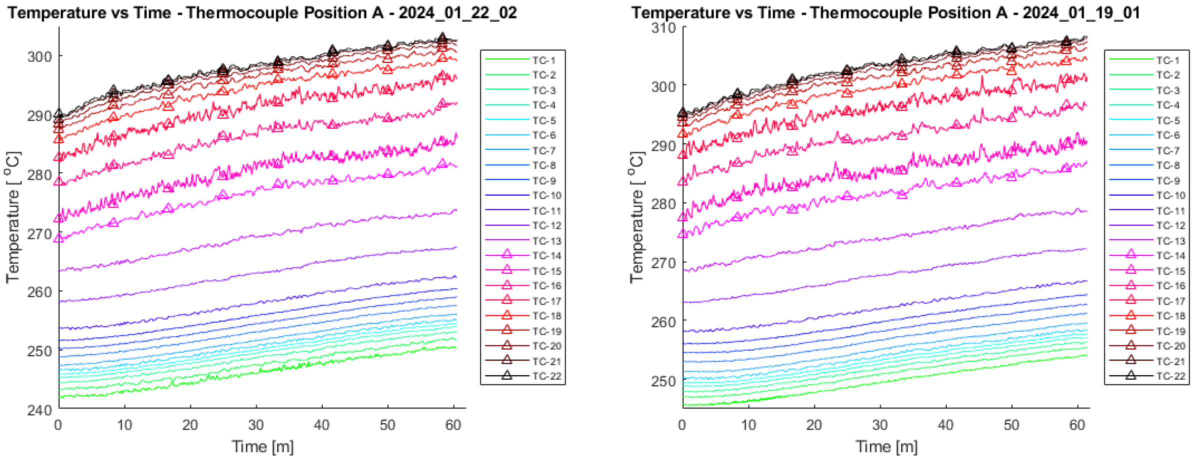

Primary Pump 6.3 GPM, Top IHX Outlet
(Phase 4 / Set 2 / Test 6)

Primary Pump 6.3 GPM, Bottom IHX Outlet
(Phase 4 / Set 2 / Test 8)

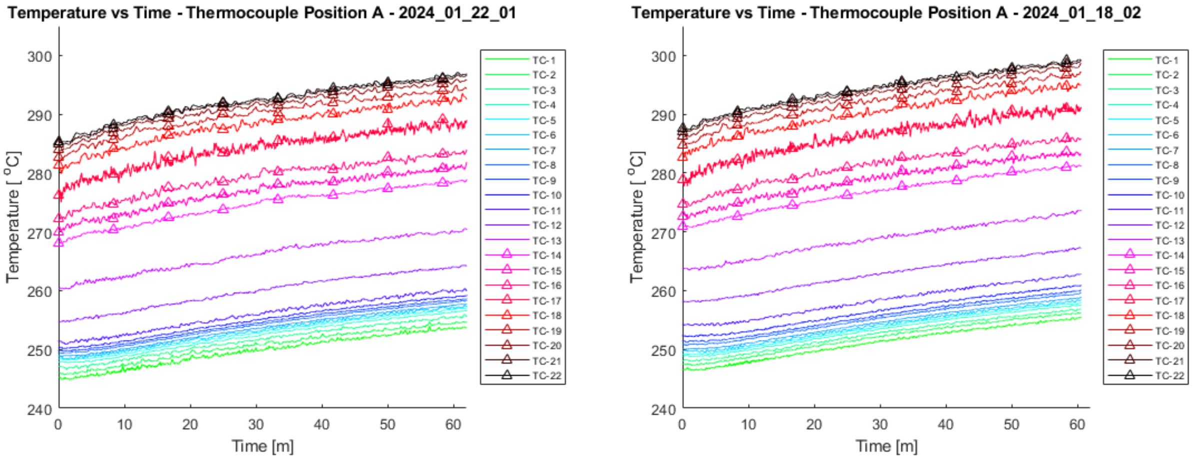

Figure 71: Position A thermocouple temperature as a function of time for Set 2, Tests 2, 4, 6, and 8

Position A thermocouple temperatures were plotted in Figure 72 for Tests 9 and 10 (Set 2). As can be seen the same amount of stratification is maintained in the hot and cold pools for both an increase and decrease in secondary system heat removal.

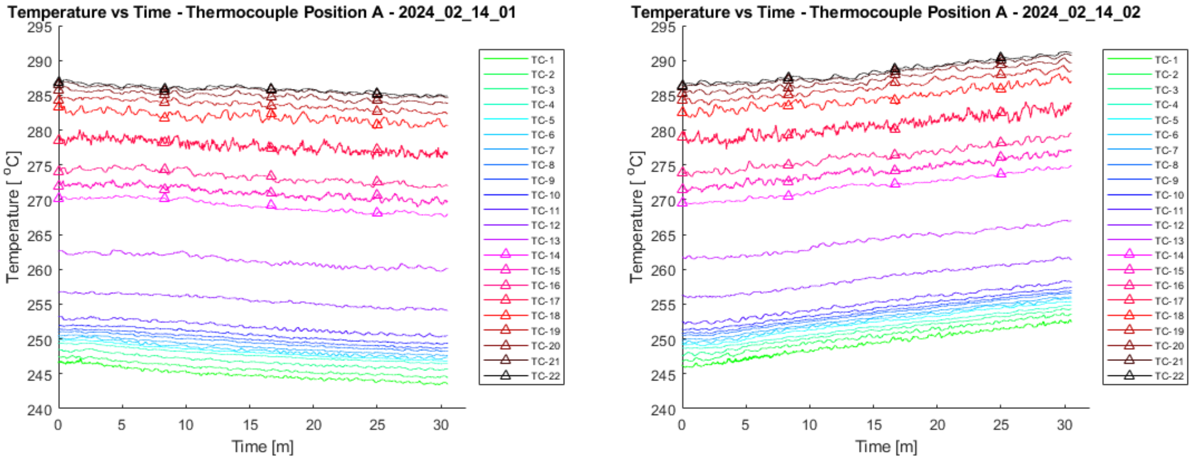

+10% Secondary Heat Removal
(Phase 4 / Set 2 / Test 9)

-10% Secondary Heat Removal
(Phase 4 / Set 2 / Test 10)

Figure 72: Position A thermocouple temperature as a function of time for Set 2, Tests 9 and 10

4.1.6. Phase 5: Flow Behavior Due to Loss of Heat Sink / Loss of Flow

During Phase 5 testing the flow behavior was characterized following loss of heat sink and flow. This was performed by bringing the primary and secondary system to a steady state condition, as defined in Table 10, followed by all primary and secondary system components being instantaneously turned off (primary pump, core, secondary pump, AHX blower). The position A thermocouple temperature was plotted for Tests 1 and 3 in Figure 73. The relatively greater thermal stratification in the low flowrate Test 1 reduces to match that of Test 3 at the end of the ~55-minute test, where both tests reach a relatively steady state stagnant condition with equal temperature distribution in the hot and cold pool. Note that Test 2 and 4 possess similar characteristics to 1 and 3, the IHX outlet elevation appears to have negligible effect on the development of a stagnant temperature distribution.

Table 10: Phase 5, Flow Behavior Due to Loss of Heat Sink / Loss of Flow

Test Number	IHX Outlet Elevation	Initial Condition
1	Top	Phase 2, Test No. 1 (High Fr, 3.6 GPM)
2	Bottom	Phase 2, Test No. 1 (High Fr, 3.6 GPM)
3	Top	Phase 2, Test No. 2 (Low Fr, 6.3 GPM)
4	Bottom	Phase 2, Test No. 2 (Low Fr, 6.3 GPM)

Primary Pump 3.6 GPM, Top IHX Outlet
(Phase 5 / Set 2 / Test 1)

Primary Pump 6.3 GPM, Top IHX Outlet
(Phase 5 / Set 2 / Test 3)

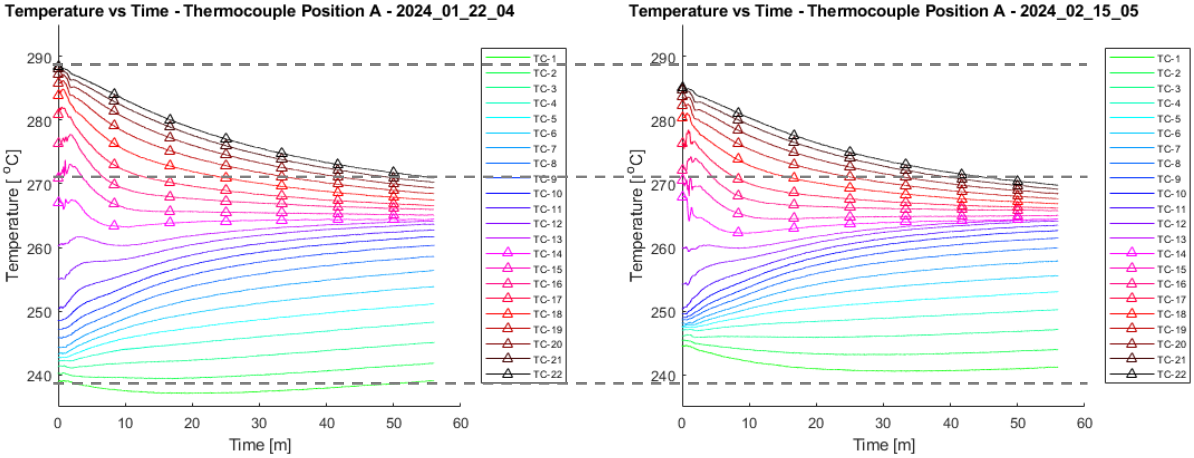

Figure 73: Position A thermocouple temperature as a function of time for Set 2, Tests 1 and 3

4.1.7. Phase 6: System-Wide Thermal Hydraulic Response

During Phase 6 the system was brought to a steady state with the secondary system online. The primary pump flow and core power were then reduced at the 30 second mark over a period of 60 minutes via a specified continuous function (provided by Oklo engineers). The secondary system was immediately turned off at the 30 second mark. This test simulates an unprotected loss of heat sink accident. Table 11 provides the Phase 6 system parameters and Figure 74 provides the core power and primary pump flowrate as well as position A thermocouple temperature as a function of time for Test 1 and 2, Set 2.

Table 11: Phase 6, System-Wide Thermal Hydraulic Response

Test Number	**IHX Outlet Elevation**	**Primary Pump Flow Rate [GPM]**	**Core Power [kWe]**	**Secondary System Operation**
1	Bottom	Function 12 → 3	Function 32.7 → 0	Step Steady State → OFF
2	Top	Function 4 → 1	Function 32.7 → 0	Step Steady State → OFF

Primary Pump 12 → 3 GPM Function, Core 32.7 → 0 kW Function, Bottom IHX Outlet

(Phase 6 / Set 2 / Test 1)

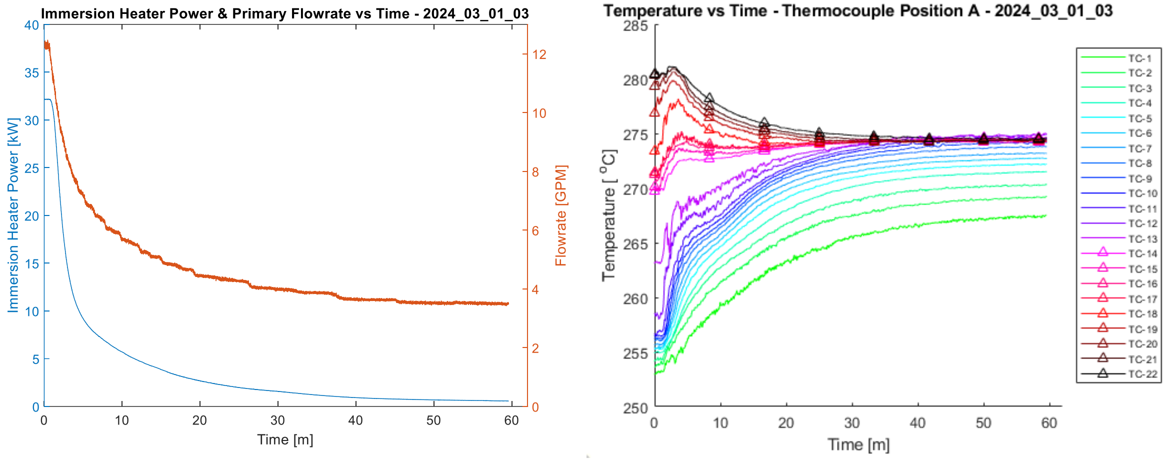

Primary Pump 4 → 1 GPM Function, Core 32.7 → 0 kW Function, Top IHX Outlet

(Phase 6 / Set 2 / Test 2)

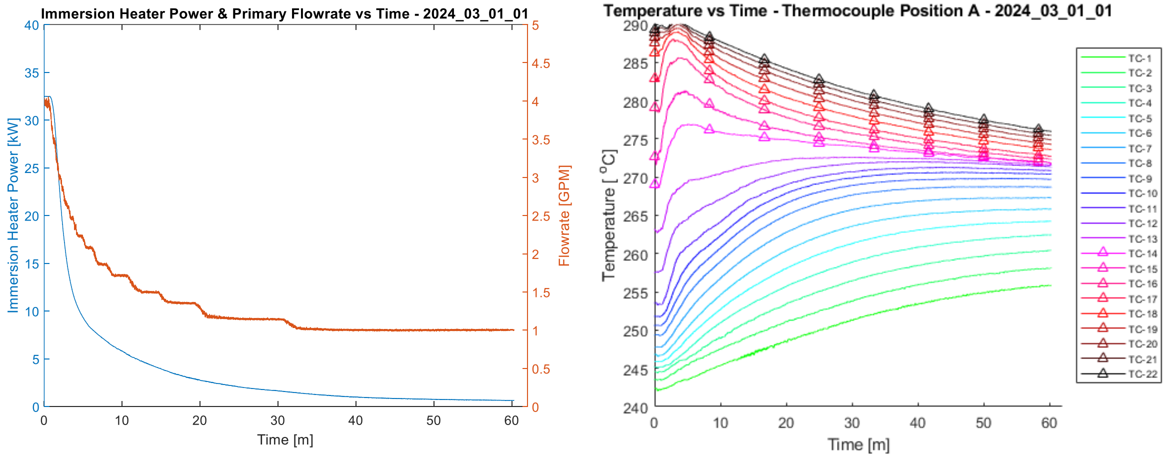

Figure 74: Core power and primary flowrate vs time, left. Position A thermocouple temperature as a function of time, right. Set 2, Tests 1 (top) and 2 (bottom)

4.1.8. Phase 7: Characterization of Core Temperature Oscillation

Significant oscillations in the core outlet thermocouple temperature were apparent during previous testing. In order to characterize the relationship between core power and temperature oscillation magnitude at the core outlet, a core power stairstep profile was implemented for the single Phase 7 test as shown in Figure 75. As can be seen the core power profile include the following 7 steps, all in units of kWe: 0, 4.1, 10.2, 17, 25.6, 36.8, 0. The test begins with an isothermal hot and cold pool at approximately 202 °C with a flowrate of 12.5 GPM. The primary flowrate was maintained at 12.5 GPM throughout the test and the secondary system was kept offline.

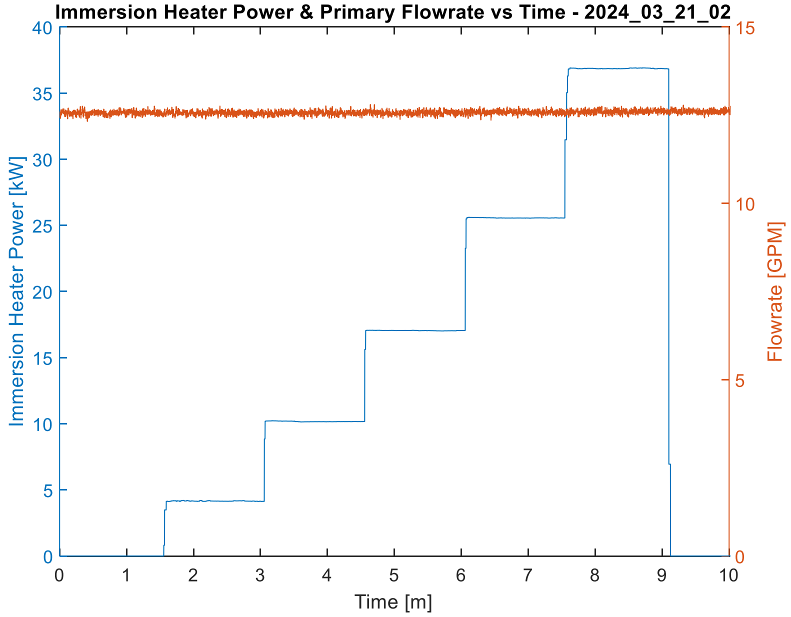

Figure 75: Phase 7 core power (blue) and primary pump flowrate (orange) as a function of time

The position A thermocouple temperature is plotted as a function of time in Figure 76. The core insulator thermocouples 1-10 as well as the core outlet thermocouple and core process control (PC) thermocouples are plotted in Figure 77. As can be seen there is a significant amount of temperature oscillation in the core outlet thermocouple at core powers greater than 4.1 kWe. In Figure 78 the core inlet, outlet, process control, position A thermocouple junction 14 (at bottom of hot pool) and the top core insulator thermocouple (#10) temperatures are plotted as a function of time. The core outlet oscillation appears to be oscillating between the core process control temperature and the temperature in the bulk sodium at the bottom of the hot pool. This is evidence of largescale mixing occurring at the outer circumference of the core where cold sodium is sinking down the sides of the core barrel before being entrained in the hot sodium closer to the core center causing thermal striping to occur in this region. Further work should be performed to characterize this effect including testing at higher primary system flowrate to see if there is a threshold where the flow is high enough to reduce re-entrainment of cold sodium in the core region. In addition, a computational fluid dynamics model should be developed which should be able to help characterize the temperature oscillation.

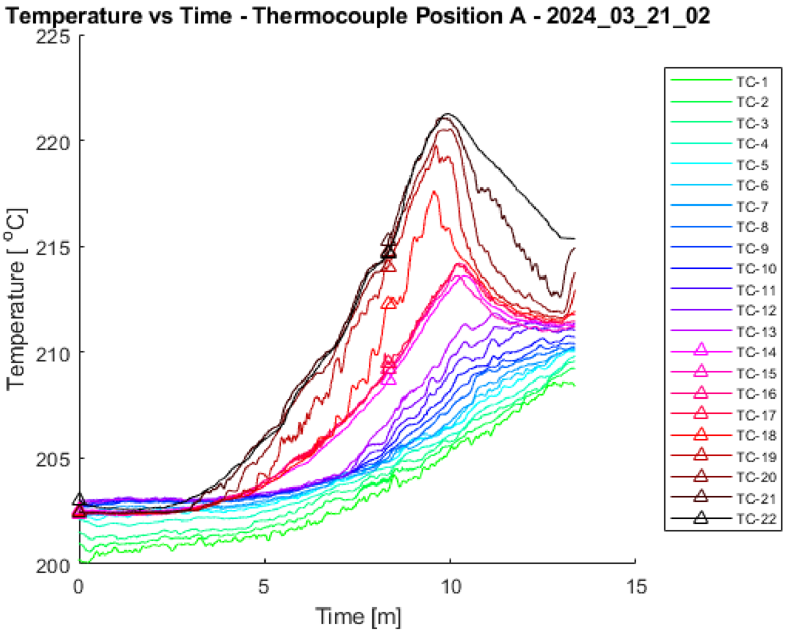

Figure 76: Position A thermocouple temperature as a function of time

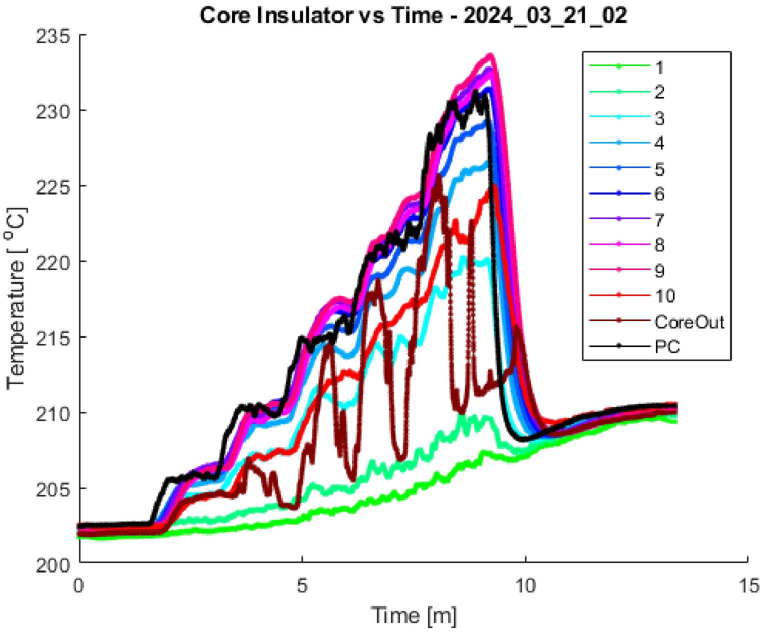

Figure 77: Core insulator, core outlet, and core process control (PC) temperature as a function of time. See Figure 30 for a diagram of sensor location

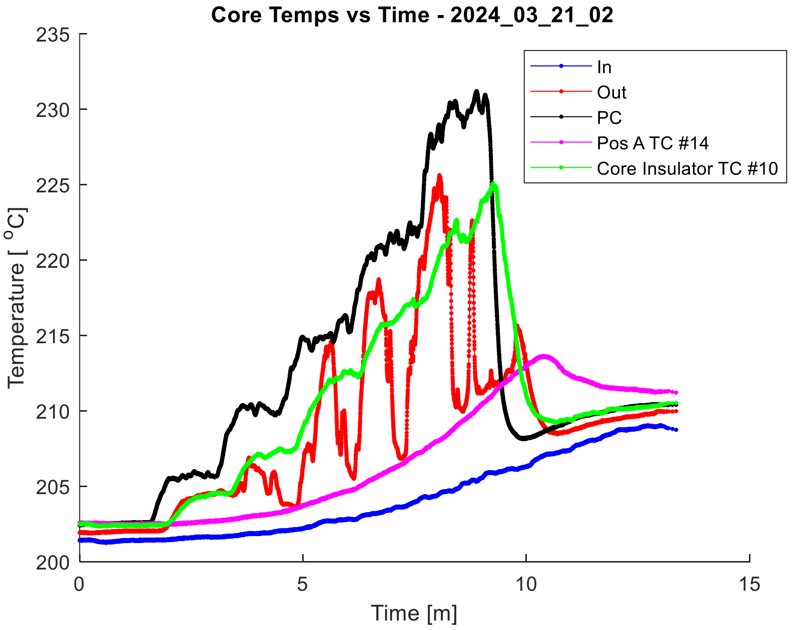

Figure 78: Core inlet, outlet, process control (PC), TCR A #14 and core insulator #10 temperature as a function of time. See Figure 30 for a diagram of sensor location

5. Conclusions

Following the completion of the installation of all THETA secondary system components and piping in 2023, extensive testing was completed this fiscal year 2024.

Noise in the secondary system flowmeter data was determined to be a result of 60 Hz noise from the AC conduction pump and process control heaters. A 60 Hz noise filter built into the data acquisition system was utilized which greatly improved performance. An auxiliary, 3D printed permanent magnet type electromagnetic flowmeter was developed that could be clamped onto an existing section of piping in an attempt to relocate the flowrate measurement away from sources of 60 Hz noise (secondary AC conduction pump). An FEA study was performed to yield a function to convert measured voltage and sodium temperature to flowrate. The auxiliary flowmeter was installed and demonstrated to operate successfully in Test #2023-05-23-01.

In this report an overview of Test ID #2023-05-23-01 was provided where steady state operations were demonstrated at core powers of 5, 12.3, and 28.2 kW. The optical fiber temperature sensors were calibrated using an in-situ method with co-located thermocouples. Fiber temperature data was then used to visualize complex thermal hydraulic features such as stratification and striping in the hot and cold pools and the intermediate heat exchanger.

An overview was provided of testing for the CRADA 2021-21121 Oklo-THETA partnership. This testing included over 100 tests with 90+ hours of active test time. Select data from each of the seven phases was presented to provide a high-level overview of the testing.

Experimental and analytical work will continue on THETA in the following fiscal year 2025 to run more tests to support systems code and computation fluid dynamics model validation efforts within Argonne and with industry and academic partners and to develop a database of test results.

Acknowledgements

The authors would like to acknowledge Daniel Andujar of the METL team for all his hard work and dedication to supporting the THETA test article. In addition, the authors would like to thank Argonne Central Shops employees for their quality craftsmanship and support, including Bill Toter, Mark Rooney, Dan Berkland, Tyler Anderson, Kristi Wood and Jonathan Torres.

This work is funded by the U.S. Department of Energy Office of Nuclear Energy's Advanced Reactor Technologies (ART) program. A special acknowledgement of thanks goes to Ms. Kaatrin Abbott, Fast Reactor Program Manager for the DOE-NE ART program, Dr. Bo Feng, the National Technical Director for Fast Reactors for the DOE-NE ART program, Ms. Savannah Fitzwater, DOE Federal Manager for National Reactor Innovation Center, and to Mr. Bradley Tomer, Acting National Technical Director for the National Reactor Innovation Center for their consistent support of the Mechanisms Engineering Test Loop and its associated experiments, including THETA.

This work was sponsored in part by the U.S. Department of Energy's Office of Nuclear Energy as part of the Gateway for Accelerated Innovation in Nuclear (GAIN) Voucher program. This work has significantly benefitted from contributions and input from the project partner, Oklo, Inc.

References

[1] Weathered, "Thermal Hydraulic Experimental Test Article - Fiscal Year 2023 Final Report," Argonne National Laboratory, Lemont, 2023.

[2] Weathered, "Thermal Hydraulic Experimental Test Article - Status Report for FY2019 Rev. 1," Argonne National Laboratory, Lemont, 2019.

[3] Jeong, Weathered and Ibarra, "Experimental Validation of Thermal Hydraulic Behavior in Sodium Fast Reactors (SFR) with the Thermal Hydraulic Experimental Test Article (THETA)," Argonne National Laboratory, Lemont, 2024.

[4] Magnet Shop, "Samarium Cobalt Disc Magnets," [Online]. Available: https://www.magnetshop.com/samarium-cobalt-disc-magnets-p-2278.html. [Accessed 01 07 2024].

[5] M. Weathered, C. Grandy, M. Anderson and D. Lisowski, "High Temperature Sodium Submersible Flowmeter Design and Analysis," *IEEE Sensors Journal,* vol. 21, no. 15, pp. 16529 - 16537, 2021.

[6] J. Fink and L. Leibowitz, "Thermodynamic and transport properties of sodium liquid and vapor," Argonne National Laboratory, Argonne, 1995.

[7] C. Ho and T. Chu, "Electrical Resistivity and Thermal Conductivity of Nine Selected AISI Stainless Steels," CINDAS, 1977.

[8] Magnet Searcher, "Samarium Cobalt Magnets," Magnet Searcher, [Online]. Available: https://www.magnetsearcher.com/index.php?c=products&a=view&id=2. [Accessed 1 7 2024].

[9] R. Carroll and R. Shepard, "Measurement of the transient response of thermocouples and resistance thermometers using an in situ method. [LMFBR]," Oak Ridge National Laboratory, 1977.

[10] J. McCay, O. Akinsulire, I. Dabkowski, P. Everett and M. Weathered, "Comparison of Sodium Stratification in CFD to Experimental Data from the Thermal Hydraulic Experimental Test Article," in *20th International Topical Meeting on Nuclear Reactor Thermal Hydraulics (NURETH-20)* , Washington D.C., 2023.

[11] Oklo, *Experimental Matrix for Oklo-THETA Partnership,* Internal Memo, 2023.

Appendix A: THETA Instrumentation Overview

Introduction

This document provides a description of instrumentation in the Thermal Hydraulic Experimental Test Article (THETA), including the specification and the position of the instrument in the experiment.

Table 12: THETA instrumentation list including the port number where the sensor is fed through the top of the THETA experiment. See Figure 79 for a schematic illustrating the location of the ports on the top of the THETA primary flange. *Previous names for these sensors included here, names were updated as of this FY'24 report for clarity so that the fiber and thermocouple names match

Port	Instrument	Instrument Name	Measurement
1a	Single TC	TC_PMP_IN	Pump inlet temperature
1b	Single TC	TC_HT_IN	Core inlet temperature
1c	Blank	-	-
1d	Blank	-	-
2a	Single TC	TC_HT_OUT	Core outlet temperature
2b	Rake TC	TC_CORE	Heater Shroud
2c	Blank	-	-
2d	Blank	-	-
3	Fiber	Fiber B (Fiber 2*)	Hot and cold pool distributed axial temperature
4	Rake TC	TCR B (TCR1*)	Hot and cold pool distributed axial temperature
5a	Rake TC	TCIHX	IHX outlet and inner vessel near wall temperature
5b	Single TC	TC_PMP_OF	Pump shaft column overflow temperature
5c	Blank	-	-
5d	Blank	-	-
6	Rake TC	TCR A (TCR2*)	Hot and cold pool distributed axial temperature
7	Fiber	Fiber A (Fiber 1*)	Hot and cold pool distributed axial temperature
8	Rake TC	TCIV	Inner vessel near wall temperature in cold pool
9	Rake TC	TCR C (TCR3*)	Hot and cold pool distributed axial temperature
10	Fiber	Fiber C (Fiber 4*)	Hot and cold pool distributed axial temperature
11	Vacuum/Gas Feedthrough	-	Vacuum/Gas Feedthrough for Core and IHX Outlet
12a	MI Cable	EMFM	Flowmeter voltage
12b	Single TC	TC_FM	Flowmeter temperature
12c	Blank	-	-
12d	Blank	-	-
13	Blank	-	-
14	Fiber	Fiber D (Fiber 3*)	IHX distributed axial temperature
15	Rake TC	TC_IHX	IHX distributed axial temperature
16	Single TC	TC_HT_PC	Core temperature 3" above bottom of elements

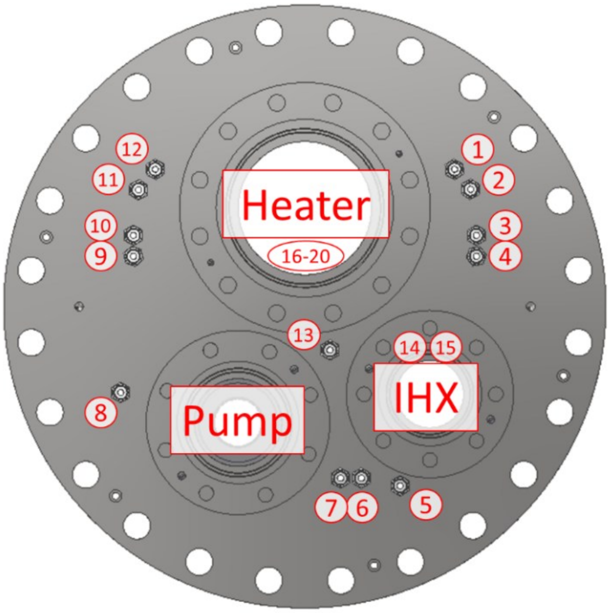

Figure 79: Locations of instrumentation feedthrough ports on top of primary flange

Primary System Thermocouple Measurements

All the thermocouples used in THETA, unless otherwise specified, are Type-K, ungrounded, with special limits of error. The accuracy of a special limits of error K type thermocouple is the greater of +/- 1.1 °C or +/- 0.4%.

Hot and Cold Pool (Instrument Name: TCR A/B/C)

Three multi-junction thermocouple probes span the hot and cold pools of THETA, instrument names TCR A, TCR B, and TCR C. Theses multi-junction probes possess 25 junctions with a resolution of 2.375”, where the first junction (TCR *A/B/C* #1) is located at the bottom tip of the probe. The axial tolerance of the junction position is ±1/16” with respect to the bottom of the probe. The bottom junction (TCR *A/B/C* #1) for the three probes are each located 30.13±0.09” below the bottom of the hot pool.

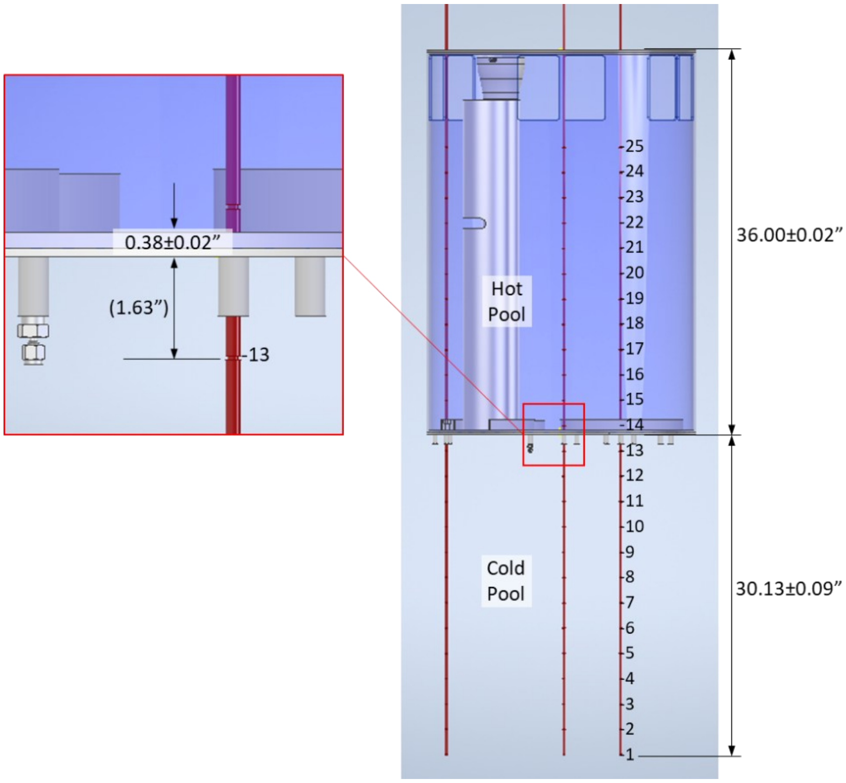

Figure 80: Axial locations of junctions for qty. (3) multijunction thermocouple probes. Appendix B provides the resolution and associated tolerance for the junction locations. Note that the probe bottom (junction 1) was positioned with a class II tape measure at a position of 30.13” below the bottom of the hot pool inner vessel bottom plate.

Hot Pool Vessel Wall (Instrument Name: TCIV)

A 1/8” OD, type K, ungrounded, multijunction thermocouple probe was installed on the outside of the hot pool inner vessel. The bottom junction (TC 1) was located flush with the bottom of the hot pool vessel bottom plate and the circumferential location of the probe was 1.88±0.09” from the weld seam that is located between two overflow windows, Figure 81. The axial tolerance of the junction position is ±1/16” with respect to the bottom of the probe.

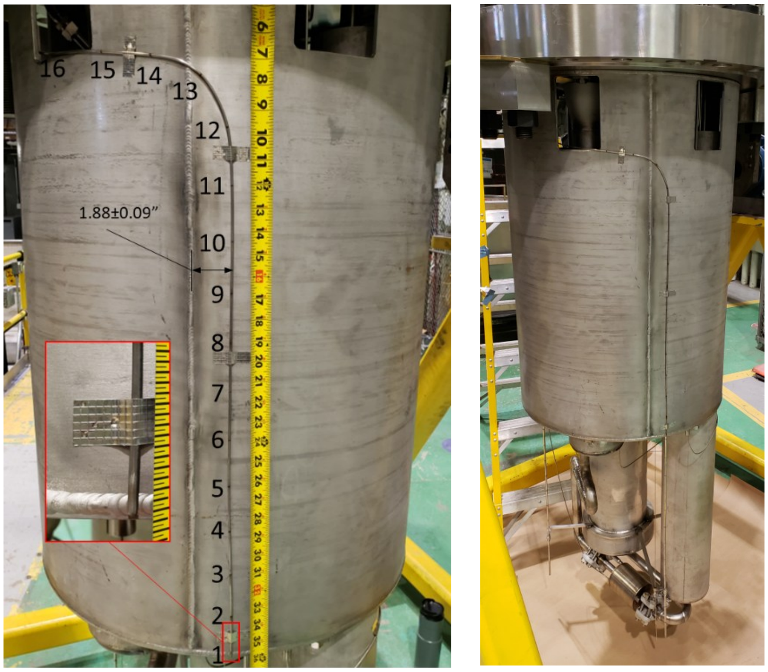

Figure 81: Photo showing location of thermocouples on hot pool vessel wall

Flowmeter (Instrument Name: TC_FM)

A single 1/8" OD type K ungrounded thermocouple probe was placed on the inside of the flowmeter, 1/8" from the permanent magnet.

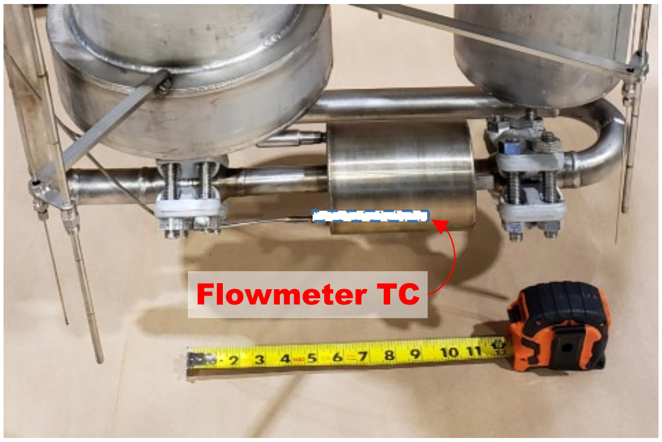

Figure 82: Photo showing locaiton of thermocouple in primary flowmeter

Pump Inlet (Instrument Name: TC_PMP_IN)

A single 1/8" OD thermocouple probe was placed at the inlet of the centrifugal pump case, Figure 83.

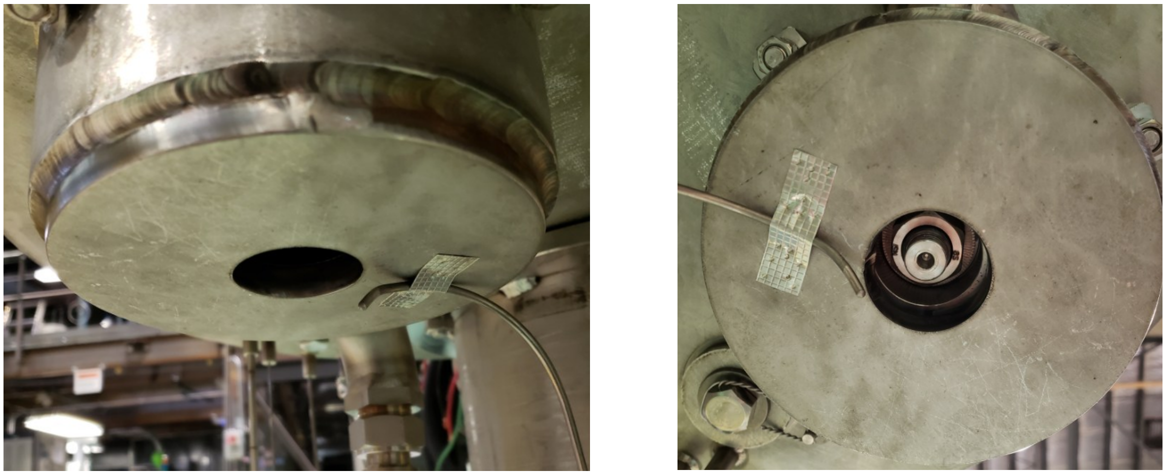

Figure 83: Photo showing location of pump inlet sodium

IHX Outlet (Instrument Name: TCIHX)

An 1/8” multijunction thermocouple probe captures sodium outlet temperature at each of the 6 IHX outlet windows, Figure 84. TCIHX_1 captures the bottom window (window 1) temperature and TCIHX_6 captures the top window (window 6) temperature and windows 2-5 are captured by TCIHX_2 through TCIHX_5, respectively. Note there are 16 total junctions, TCIHX_7 – TCIHX_8 measure cold temperature below the redan in close proximity to IHX out and TCIHX_9 – TCIHX_16 measure temperature at the base of the hot pool. TCIHX_1 is located 2.5” from the tip of the probe. TCIHX_1-6 have a pitch of 4.5”. TCIHX_7 is located 38” from the tip of the probe. TCIHX_7-16 possess a pitch of 2.375”. The axial tolerance of the junction position is ±1/16” with respect to the bottom of the probe.

Figure 84: Phot showing IHX outlet thermcouple junction locations

Core Inlet (Instrument Name: TC_HT_IN)

A single 1/8” OD thermocouple probe was placed at the inlet of the core, Figure 85.

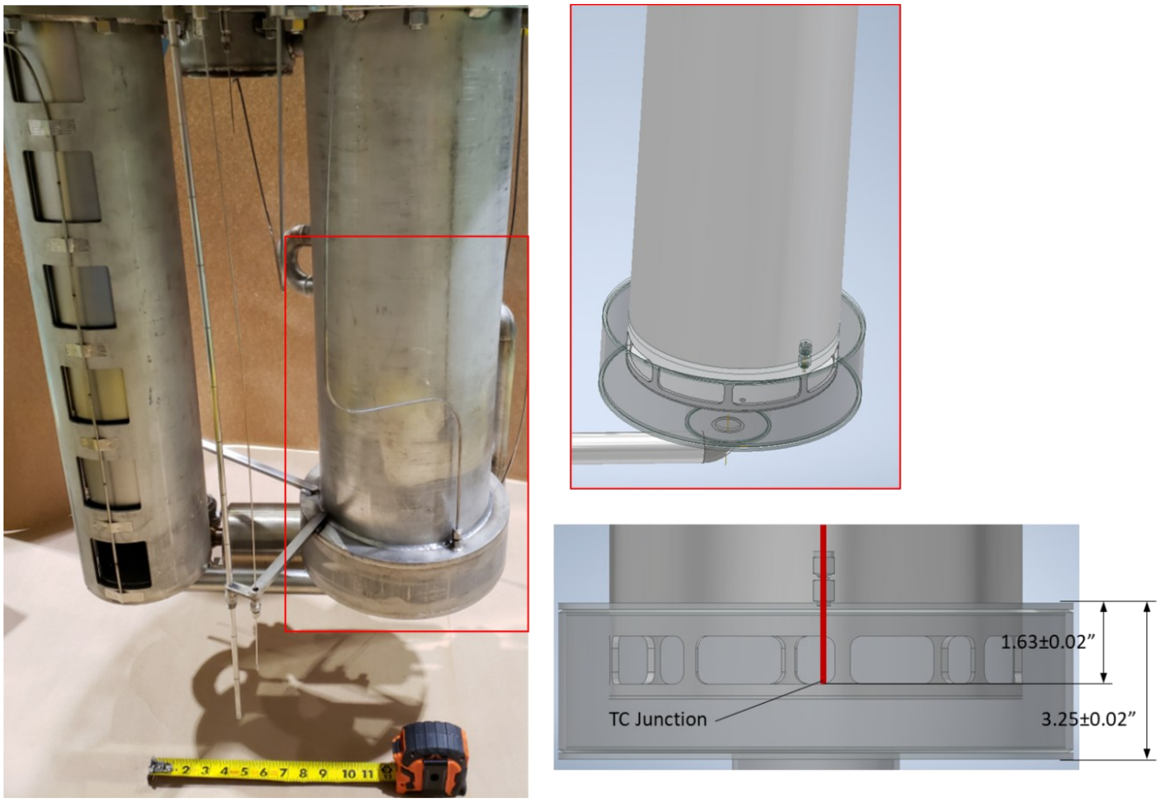

Figure 85: Photo and schematic showing core inlet thermocuple

Core Outlet (Instrument Name: TC_HT_OUT)
A single 1/8” OD thermocouple probe was placed at the outlet of the core, Figure 86.

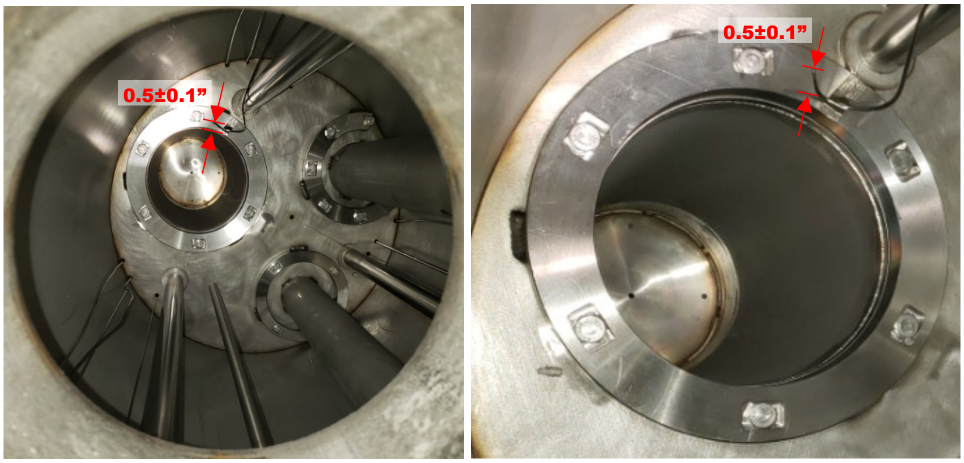

Figure 86: Photos showing core outlet thermocouple

Core Insulator (Instrument Name: TC_Core)
An 1/8” multijunction thermocouple probe captures temperature between the core insulator jacket and the core barrel. TC1 is located at the probe tip and TC2-16 possess a pitch of 2.375”. The axial tolerance of the junction position is ±1/16” with respect to the bottom of the probe.

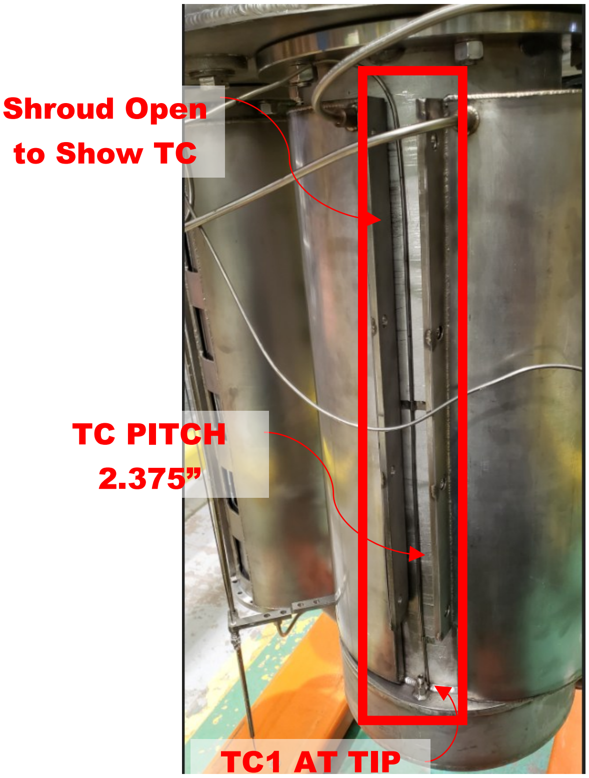

Figure 87: Photo showing core insulator thermocouple measurements. Note the clamshell insulator has been opened up to show the thermocouple rake.

IHX Shell (TC_IHX)

A 1/8”, K-type ungrounded multijunction (16 junction) thermocouple probe captures sodium temperature on the shell side of the IHX starting at the top of the collector (32.87” below the wetted face of the main flange), measuring every 1.75”. Note the 1” tall sodium inlet for the shell side of the IHX is located 16.25” below the wetted face of the main flange. Thus TC #11 will measure the sodium temperature at the elevation of the 1” tall sodium inlet.

Figure 88: Intermediate heat exchanger (IHX)

Core Process Control (Instrument Name: TC_HT_PC)
TC_HT_PC is a 1/8” OD thermocouple probe 3 inches above the bottom of the core in the center of the core

Secondary System Thermocouple Measurements

All the thermocouples used in THETA, unless otherwise specified, are Type-K, ungrounded, with special limits of error. The accuracy of a special limits of error K type thermocouple is the greater of +/- 1.1 °C or +/- 0.4%.

IHX Inlet and Outlet (Instrument names: TC_IHX_IN, TC_IHX_OUT)
1/8” OD thermocouples are installed in thermowells with the junction located near the center of the sodium flow cross section to measure the temperature at the inlet and outlet of the intermediate heat exchanger. TC_IHX_OUT is located at around 13” from the elbow of the upcomer pipe and TC_IHX_IN is located around 10” from the elbow of the downcomer pipe.

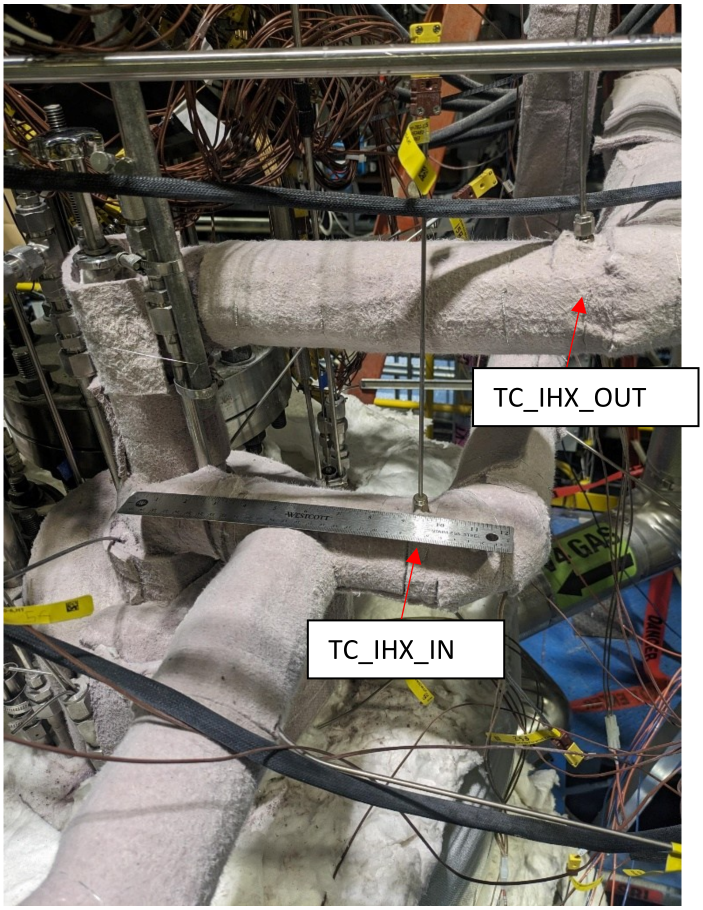

AHX Sodium Inlet and Outlet (Instrument names: TC_AHX_Na_IN, TC_AHX_Na_OUT)
1/8” OD thermocouples are installed to measure the sodium temperature at the inlet and outlet of the AHX. TC_AHX_Na_IN is a wetted TC immersed in the sodium at the inlet pipe, 6” from the in plenum head. TC_AHX_Na_OUT is located in a thermowell with the junction located near the center of the outlet plenum sodium.

AHX Air Inlet and Outlet (Instrument names: TC_AHX_Air_IN, TC_AHX_Air_OUT)
1/8” OD thermocouples are installed to measure the air temperature at the inlet and outlet of the AHX. The thermocouples are located at the center of the airflow, approximately 6” from the flanged inlet and outlets of the AHX shell.

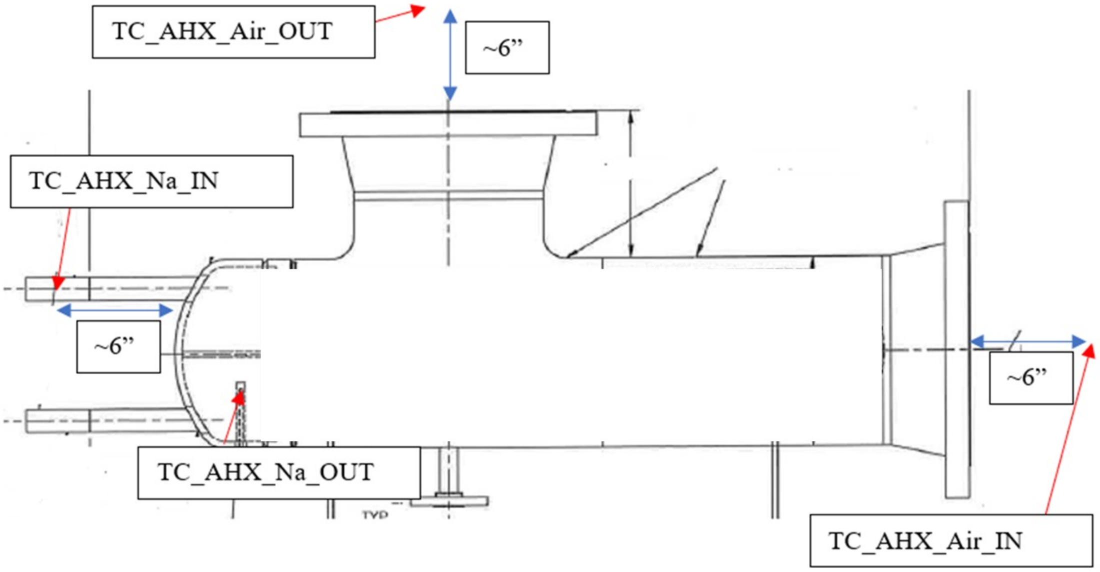
TC_AHX_Air_OUT
~6”
TC_AHX_Na_IN
~6”
~6”
TC_AHX_Na_OUT
TYP
TC_AHX_Air_IN

Secondary Piping Process Control Thermocouples

The 3/4" SCH40, 316SS secondary sodium piping network is split into 15 distinct zones as shown below. There are two process control thermocouples per zone (1/8", ungrounded, type K mounted with 316SS hose clamp). The thermocouples are labeled as TC_m8_1a and TC_m8_1b for zone 1 TC a and b and TC_m8_2a and TC_m8_2b for zone 2 TC a and b, etc.

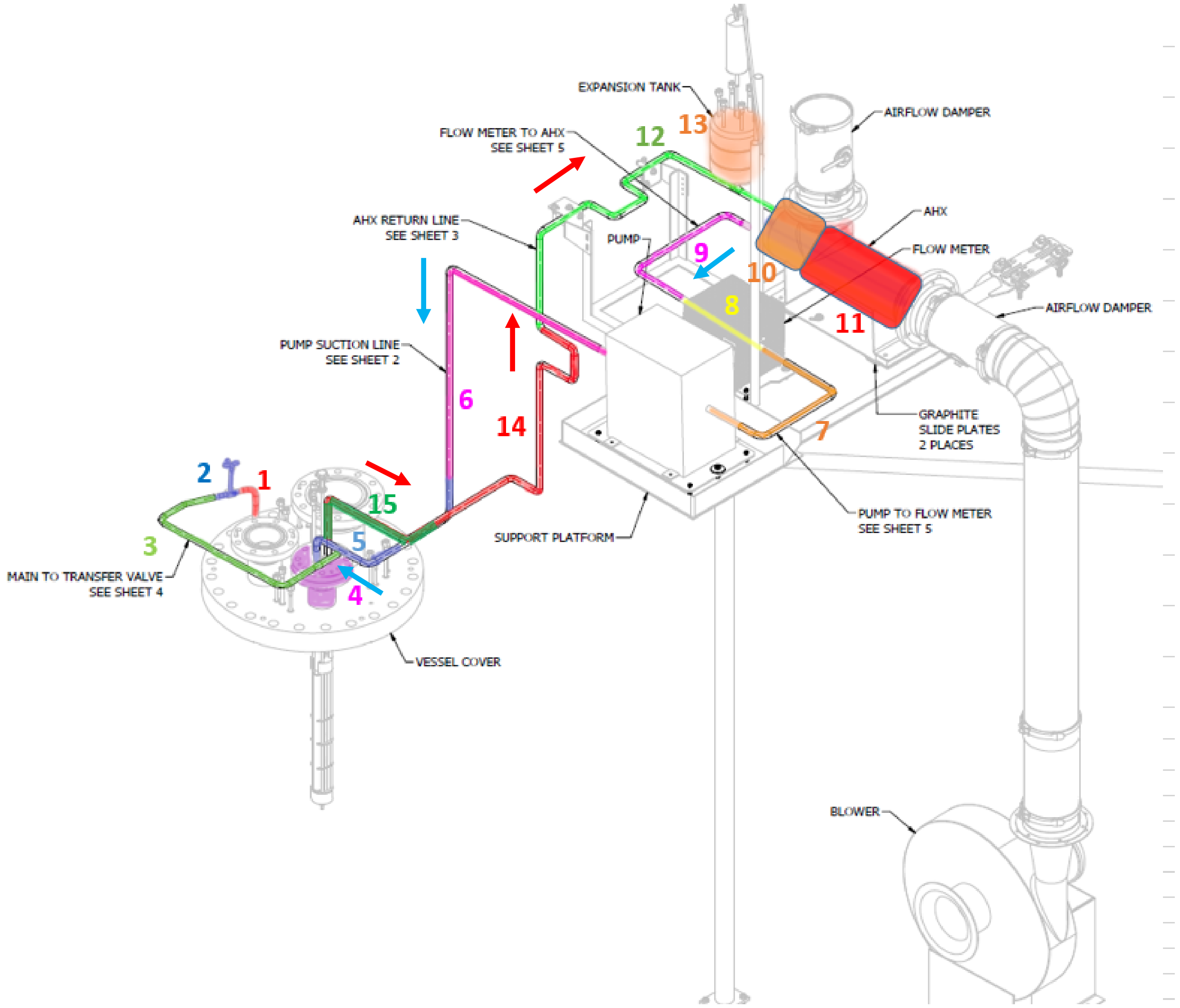

Optical Fiber Temperature Sensors (Fiber A/B/C/D)

A Rayleigh backscatter based optical frequency domain reflectometry system was used (ODISI 6104) to acquire distributed temperature measurements in the THETA hot and cold pools. Locations of the feedthroughs for the optical fibers can be found in Figure 79, Table 12.

Electromagnetic Flowmeter

A custom-built electromagnetic flowmeter was designed and built at Argonne. A paper describing the calibration procedure of this particular flowmeter can be found in literature.[1]

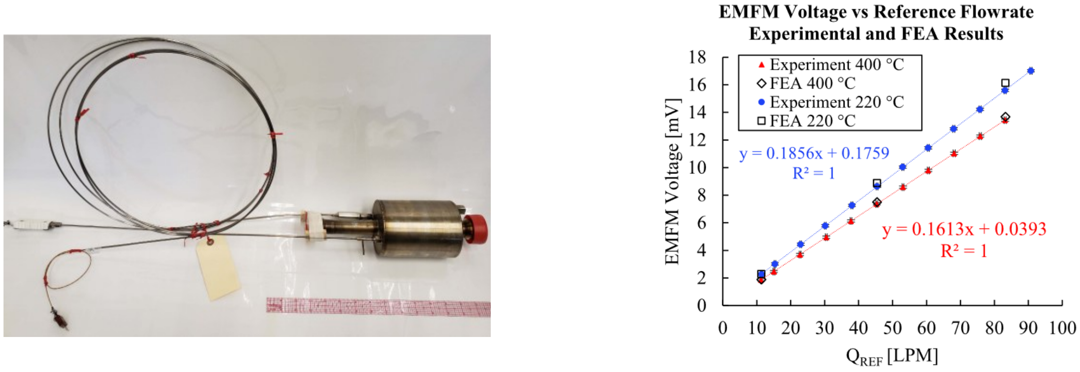

Figure 89: Flowmeter, left, voltage vs flowrate calibration plot, right.

Power Meter

A three-phase power meter) was installed on the immersion heater control panel to acquire power measurements. The measurement accuracy has been included in Figure 90.

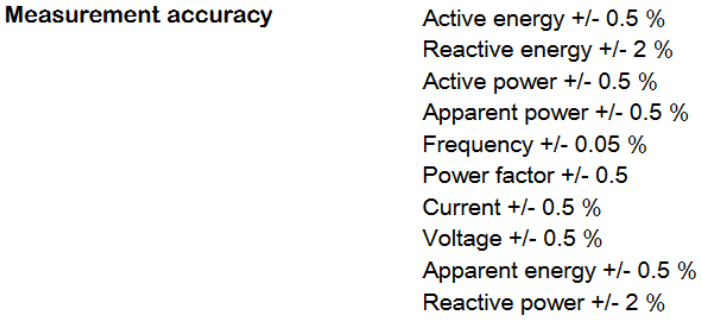

Measurement accuracy	Active energy +/- 0.5 % Reactive energy +/- 2 % Active power +/- 0.5 % Apparent power +/- 0.5 % Frequency +/- 0.05 % Power factor +/- 0.5 Current +/- 0.5 % Voltage +/- 0.5 % Apparent energy +/- 0.5 % Reactive power +/- 2 %

Figure 90: Electric power meter manufacturer rated accuracy

Air Flowmeter

A 0-50.8 m/sec air velocity transmitter with a 2% accuracy at full scale was used to measure the flowrate of the air leaving the blower before entering the sodium-to-air shell. The transmitter was installed in the ducting at approximately 3 feet from the blower exit.

---

[1] Weathered et al, "High Temperature Sodium Submersible Flowmeter Design and Analysis," IEEE Sensors Volume 21, Issue 15, 13 May 2021

Appendix B: Test ID for all Oklo GAIN Voucher Results (CRADA 2021-21121)

Phase	Set	Item	Test No.	Results file ID
1	1	A	1	2022_05_11_02
			2	2022_05_18_02
			3	2022_05_19_01
			4	2022_05_12_01
			5	2022_05_16_01
			6	2022_05_13_01
		B	1	06_23_22_01
			2	06_24_22_01
			3	06_27_22_01
			4	06_28_22_01
			5	06_29_22_01
			6	07_06_22_01
	2	A	1	2022_11_30_01
			2	2022_12_08_01
			3	2022_11_15_01
			4	2022_11_28_01
			5	2022_11_18_01
			6	2022_11_23_01
		B	1	2022_11_14_01
			2	2022_11_10_01
			3	2022_11_03_01
			4	2022_11_01_01
			5	2022_09_29_01
			6	2022_09_27_01
1.5	1	A	1	2023_06_01_02
			2	2023_06_02_01
			3	2023_06_09_01
		B	1	2023_06_05_01
			2	2023_06_06_01
			3	2023_06_09_02
	2	A	1	2023_06_08_01
			2	2023_06_08_02
			3	2023_06_11_02
		B	1	2023_06_07_01
			2	2023_06_06_02
			3	2023_06_11_01
2	1		1	2023_11_14_02
			2	2023_11_14_03
			3	2023_11_15_06
			4	2023_11_16_01
	2		1	N/A
			2	2023_11_15_04
			3	2023_11_16_03
			4	2023_11_16_02

Phase	Set	Test No.	Results file ID
3	1	1	2023_11_17_01
		2	2023_11_17_02
		3	2023_11_17_04
		4	2023_11_20_01
		5	2023_11_20_02
		6	2023_11_20_04
		7	2023_11_21_01
		8	2023_11_21_02
		9	2023_11_22_01
		10	2023_11_22_02
	2	1	2024_02_20_01
		2	2024_02_15_04
		3	2024_02_19_01
		4	2024_02_15_01
		5	2024_02_19_04
		6	2024_02_15_02
		7	2024_02_19_02
		8	2024_02_14_05
		9	2024_02_16_01
		10	2024_02_16_02
4	1	1	2023_12_19_02
		2	2023_12_19_04
		3	2023_12_20_01
		4	2023_12_20_02
		5	2023_12_21_01
		6	2023_12_21_02
		7	2024_01_04_01
		8	2024_01_04_02
		9	2024_01_08_02
		10	2024_01_08_03
		11	2024_01_09_01
		12	2024_01_09_02
	2	1	2024_01_22_03
		2	2024_01_22_02
		3	2024_01_19_02
		4	2024_01_19_01
		5	2024_01_19_04
		6	2024_01_22_01
		7	2024_01_18_03
		8	2024_01_18_02
		9	2024_02_14_01
		10	2024_02_14_02
		11	2024_02_14_03
		12	2024_02_14_04

Phase	Set	Test No.	Results file ID
5	1	1	2024_01_11_02
		2	2024_01_10_01
		3	2024_01_11_01
		4	2024_01_09_04
	2	1	2024_01_22_04
		2	2024_01_19_03
		3	2024_02_15_05
		4	2024_03_01_02
6	1	1	2024_02_29_02
		2	2024_02_29_03
	2	1	2024_03_01_03
		2	2024_03_01_01
7			2024_03_21_02

Nuclear Science & Engineering
Argonne National Laboratory
9700 South Cass Avenue, Bldg. 308
Argonne, IL 60439

www.anl.gov